UNIVERSITY OF CALIFORNIA, MERCED

Expanding the computational toolkit for theoretical chemistry studies

by

Xianghai Sheng

A dissertation submitted in partial satisfaction of the
requirements for the degree of
Doctor of Philosophy

in

Chemistry

Committee in charge:
Professor Christine Isborn, Chair
Professor Hrant P. Hratchian, Advisor
Professor Michael E. Colvin
Professor Dong Li

Spring 2019

The dissertation of Xianghai Sheng is approved:

Christine Isborn, Chair	Date
Hrant P. Hratchian, Advisor	Date
Michael E. Colvin	Date
Dong Li	Date

University of California, Merced

To my wife

Acknowledgments

First of all, I would like to sincerely thank my advisor Professor Hrant P. Hratchian. Without his constant guidance over the years, this work would not have been possible. I was inspired and enlightened by his profound knowledge, acute insights, deep understanding of the philosophy of research, and sense of humor.

I would like to thank my dissertation committee, Professor Christine Isborn and Professor Michael E. Colvin from Chemistry and Chemical Biology, and Professor Dong Li form Computer Science for their time, insightful comments and constructive guidance that significantly improved this dissertation.

I also would like to express my appreciation to my previous and current labmates and colleagues at UC Merced. Professor. Lee M. Thompson offered me great advice and was a huge help during the early stages of my Ph.D. I certainly enjoyed all the lunches we had together. I also want to thank my current colleagues Samantha Bidwell, Hassan Harb, Ali Abou Taka and Abdulrahman Zamani for all the collaborations and the time we spent together.

I also would like to thank the numerous fellowship awards, financial support and training from being research and teaching assistant at UC Merced.

My sincerest thanks to my wife Duan, who is the best thing that has happened in my life. She has always been there for me at times of frustration and celebration. She is my strongest supporter through this journey to my Ph.D. I can't imagine making it through graduate school without her.

Last but not least, I want to express my gratitude to my parents. They have sacrificed a lot to raise me with a sense of responsibility, a deep understanding of the meaning of hard work and an optimal attitude for appreciation of life. They have always been a constant source of love and encouragement for me.

Curriculum Vitae

Education

- Ph.D. in Chemistry. University of California, Merced (UCM). Merced, CA, USA. Aug. 2014-current
- B.S. in Chemistry. Fudan University (FDU). Shanghai, China. Sept. 2010-July 2014

Publications

1. Sheng, X.; Thompson, L., Hratchian, H. *Assessing the Calculation of Exchange Coupling Constants and Spin Crossover Gaps Using the Approximate Projection Model to Improve Density Function Calculations*, J. Chem. Theory Comput. Submitted.

Presentations

1. 253rd ACS National Meeting, Mar. 2017, San Francisco, CA, USA. *Finding minimum on crossing point in intersystem crossing events.*
2. Theory and Application of Computational Chemistry (TACC), Aug. 2016, Seattle, Washington, USA. *Improved Exchange Coupling Constants and Spin Crossover Gaps for Transition Metal Complexes Using Spin Projection*
3. 251st ACS National Meeting, Mar. 2015, San Diego, CA, USA. *Better magnetic properties by DFT with projection methods*

Honors

University of California, Merced, CA, USA

UC Merced CCB Travel Fellowship Award, UC Merced	2016
UC Mercd Graduate Summer Fellowship Award, UC Merced	2015, 2016

Fudan University, Shanghai, China

Outstanding Student Award	2011-2013

Contents

List of Figures

List of Tables

Nomenclature and Abbreviations

AC	Atom Connectivity
AF	Anti-Ferromagnetic
AFIR	Artificial Force-Induced Reaction
AP	Approximate Projection
B	Broken-symmetry
BE	Bond Electron (matrix)
BFGS	Broyden-Fletcher-Goldfarb-Shanno
BO	Born-Oppenheimer
CCSD	Coupled Cluster Singles and Doubles
CI	Configuration Interaction
DFT	Density Functional Theory
DIIS	Direct Inverse in the Iterative Subspace
DVR	Discrete Variable Representation
EPR	Electron Paramagnetic Resonance
FC	Franck-Condon
FC	Formal Charge
FM	Ferromagnetic
GEDIIS	Energy-Represented DIIS
GP	Gradient Projection
HF	Hartree-Fock
HS	High Spin
IR	Infrared
IRC	Intrinsic Reaction Coordinate
J(-coupling)	Magnetic exchange coupling constant
KS	Kohn-Sham
LS	Low Spin
MAE	Mean Absolute Error
MECP	Minimum Energy Crossing Point
MR	Molecular Representation
NP	Non-Projected
PAV	Projection-after-Variation
PCM	Polarizable Continuum Model
PES	Potential Energy Surface

PHF	Projected Hartree-Fock
RFO	Rational Function Optimization
RHF	Restricted Hartree-Fock
RMS	Root Mean Square
RMSD	Root Mean Square Distance
SC	Stuttgart/Cologne ECPxMHF
SCF	Self-Consistent Field
SMILES	Simplified Molecular-Input Line-Entry System
SP	Spin-Projected
SCE	Spin Contamination Error
TBO	Total Bond Order
TS	Transition State
UDFT	Unrestricted DFT
UHF	Unrestricted Hartree-Fock
VAP	Variation-after-Projection
VSEPR	Valence Shell Electron Pair Repulsion

Abstract

Expanding the computational toolkit for theoretical chemistry studies
by
Xianghai Sheng
Doctor of Philosophy
in
Chemistry
University of California, Merced
Professor Christine Isborn, Chair

Chemistry has been a primarily laboratory science since its beginning. However, with thanks to powerful modern high performance computer hardware and decades of theoretical chemistry research, the critical role of computational chemistry in today's chemical research enterprise is undeniable. Computational tools serve as a bridge between chemical theory and computer hardware, helping scientists with nearly all aspects of chemistry research. Indeed, it has been a significant driving force that pushes the chemical science forward. This thesis expands the computational toolkit for theoretical chemistry studies, with an emphasis on potential energy surface related studies and transition metal systems.

Proposing a theoretical mechanism for a newly discovered chemical reaction is a difficult job that requires extensive work from well-trained computational chemists. An automatic mechanism generator is proposed to automate this process. Given a reactant and a product, the methodology described expands the chemical space between them, finds the optimal reaction pathway, and reports the most probable mechanisms. The reaction network expands by enumerating all possible elementary reactions based on an electron pushing model. Each generated intermediate is filtered by user-defined atom configuration rules, in order to reduce the complexity of the algorithm.

Spin crossover, or intersystem crossing, happens in many important chemical processes. It takes place at the minimum energy on the crossing seam of two potential energy surfaces of different spins. In this work we developed an efficient optimizer to find the minimum energy crossing point in a spin crossover event. Finding this geometry will facilitate kinetic and thermodynamic studies on spin crossover events. This optimizer is integrated with highly efficient geometry optimization schemes that were published recently.

Zirconium oxide is found to have potential applications as catalyst in water splitting reactions. The work described in chapter 5 aimed to interpret a spectrum obtained from photodetachment spectroscopy on the adduct of ZrO_2 and H_2O by an experimental collaborator. Employing two-dimensional DVR (Discrete Variable Representation) method, we were able to account for the anharmonicity of the umbrella mode of the adduct, and interpret most of the peaks in a dense vibronic spectra, thus shedding some light on the structure of the adduct.

Spin contamination is a well-documented error of single-determinant DFT methods. The work described in chapter 3 employed Approximate Projection (AP), a simple and efficient spin-projection method to treat spin contamination in DFT calculations, to test its effect in predicting

exchange coupling constant and spin crossover gap. In summary, AP greatly reduced error in predicted spin crossover gaps caused by spin contamination. In terms of predicting exchange coupling constants, AP did not perform better than a non-projection method, which was due to statistical reasons. In addition, AP's effect on geometry optimization and subsequent effects on the two physical constants were tested as well, and were found to be significant for exchange coupling constants, and otherwise for spin crossover gaps.

Chapter 1

Introduction

The use of computers for chemistry studies has paralleled the development of computers since the 1950s, and has been a core area of chemical research in more recent years. Apart from universal use cases such as visualization and automation, two main uses of computers in chemistry is to carry out immense mathematical calculations often introduced by the Schrödinger equation, as well as to explore vast chemical spaces.

1.1 Fundamentals of Quantum Chemistry

Proposed in 1926, the Schrödinger equation [1] is central to quantum chemistry, and has been studied by generations of theoretical chemists. It is a partial differential equation that describes the wave function of a quantum-mechanical system. This equation is not exactly solvable when the system has multiple interacting electrons, because of the correlation between them. Various approximations have been proposed to find approximate solutions to this equation. This thesis primarily focuses on the non-relativistic, time-independent Schrödinger equation, given by

$$\hat{H}|\Psi\rangle = E|\Psi\rangle \tag{1.1}$$

where $\hat{H}$ is the hamiltonian operator, $|\Psi\rangle$ is the wave function and E is the energy of the system. The hamiltonian operator is given by

$$\hat{H} = -\sum_{i=1}^{N} \frac{1}{2}\nabla_i^2 - \sum_{A=1}^{M} \frac{1}{2M_A}\nabla_A^2 - \sum_{i=1}^{N}\sum_{A=1}^{M} \frac{Z_A}{r_{iA}} + \sum_{i=1}^{N}\sum_{j>i}^{N} \frac{1}{r_{ij}} + \sum_{A=1}^{M}\sum_{B>A}^{M} \frac{Z_A Z_B}{R_{AB}} \tag{1.2}$$

Atomic units are used in this equation. M_A is the ratio of the mass of nucleus to the mass of an electron, and Z_A is the atomic number of nucleus A. The Laplacian operators ∇_i^2 and ∇_A^2 involve differentiation with respect to the coordinates of the ith electron and the Ath nucleus. The first and second term in Eq. 1.2 are the operator for kinetic energy of the electrons and nuclei respectively; the third term represents the coulomb attraction between electrons and nuclei; the fourth and fifth terms represent the repulsion between electrons and between nuclei respectively.

One central approximation assumed by most theoretical chemistry studies is Born-Oppenheimer

(BO) Approximation [2], which states that nuclei move much more slowly than electrons because of they are much heavier. Therefore, the two motions of electrons and of nuclei can be separated and electrons can be considered to be moving around fixed nuclei. Applying this approximation, the second term in Eq. 1.2, the kinetic energy of the nuclei, can be neglected and the last term, the nuclear repulsion, can be considered constant. The terms that remain are called the electronic Hamiltonian, which is explicitly dependent on the electronic coordinates while parametrically dependent on the nuclear coordinates.

To solve the electronic Schrödinger equation, the Hartree-Fock [3–5] (HF) approximation was introduced where the wave function is approximated by a single Slater determinant of orbitals (single-particle wave functions).

$$|\Psi_0\rangle = |\psi_1\psi_2 \dots \psi_N\rangle \tag{1.3}$$

This form satisfies the requirement that the wave function should be anti-symmetric. The orbitals ψ_i are represented by linear combinations of known basis functions $\{\phi_\mu(\mathbf{r})|\mu = 1, 2, ..., K\}$, given by

$$\psi_i = \sum_{\mu=1}^{K} C_{\mu i}\phi_\mu \tag{1.4}$$

According to variational principle, the ground state energy should be minimized to give the best combination of coefficients for the ground state. This gives rise to Roothaan equations, given by

$$\sum_\nu F_{\mu\nu}C_{\nu i} = \epsilon_i \sum_\nu S_{\mu\nu}C_{\nu i} \tag{1.5}$$

where S is the overlap matrix. Its elements are defined by

$$S_{\mu\nu} = \langle\mu|\nu\rangle \tag{1.6}$$

where μ and ν are ϕ_μ and ϕ_ν respectively. F is the Fock matrix. Its elements are defined by

$$F_{\mu\nu} = (\mu|\hat{H}_1|\nu) + \sum_{\lambda\sigma} P_{\lambda\sigma}[(\mu\nu|\lambda\sigma) - \frac{1}{2}(\mu\sigma|\lambda\nu)] \tag{1.7}$$

where $(\mu\nu|\lambda\sigma)$ are the electron-electron repulsion integrals, $\hat{H}_1$ is the one-electron Hamiltonian (including the first and the fourth term in Eq. 1.2), and P in Eq. 1.7 is the density matrix. P's element is given by

$$P_{\lambda\sigma} = 2 \sum_{i=1}^{occupied} C^*_{\lambda i}C_{\sigma i} \tag{1.8}$$

The Roothaan equation is solved through an iterative self-consistent field (SCF) procedure since Fock matrix is itself dependent on the coefficient matrix. The solution gives the coefficients in Eq. 1.4, and thus gives an approximate wave function with a minimized ground state energy. This energy is an upper bound of the true energy.

The difference between the HF model and the exact non-relativistic energy is often called electron correlation. [6] Although the HF method is able to account for $\sim$ 99% of the total energy

with a large basis set, the remaining $\sim 1\%$ correlation energy often plays important roles in explaining chemical processes. Correlation energy primarily arises from two sources. First, HF method uses a single Slater determinant to represent a wave function, which could be a poor representation of a state of a many-electron system, especially when the system has multiple (near-)degenerate Slater determinants. This type of correlation is termed static correlation. Second, in a HF solution, electrons do not interact instantaneously with each other, as they do in reality. The Coulomb repulsion between electrons is treated as if each electron is surrounded by a mean-field created by all other electrons. This type of correlation is termed dynamic correlation. It should be noted that there is not a clear boundary between the two types of correlation; they are rather useful concepts to consider when one tries to remedy the deficiencies of HF. Some methods are better at calculating dynamic correlation while some are good at static correlation.

Despite its deficiencies, HF is a good starting point for many methods of higher accuracy, including configuration interaction [7, 8] (CI), coupled cluster theory [9–11] and Møller-Plesset perturbation theory [12, 13], *etc*. These methods can all be systematically improved by including higher excitation states or higher-order terms to their equations. However the added computational cost from these terms are substantial and sometimes cost-prohibitive.

Another line of methods is based on Density Functional Theory [14, 15] (DFT), which states that there is a one-to-one correspondence between the electron density and the energy of a system. In other words, the ground state energy is determined completely by the electron density ρ which is a function of three spacial coordinates. Thus this method is orbital-free and only involve 3 variables. However, it suffers from a poor representation of kinetic energy [16].

Kohn and Sham [17] popularized this method by introducing the concept of orbitals to DFT, gaining a more accurate kinetic energy term while paying a price of increasing from 3 to 3N variables. Since then, DFT has gained great popularity and is one of the most used computational chemistry methods because of its good accuracy to cost ratio. [18] Despite its popularity, DFT has a number of well-documented limitations. [19–21] A major one is that DFT can not be systematically improved, whereas HF based methods can. This thesis address another limitation [21, 22], which is the fact that DFT often fails to yield the correct eigenvalue of $\langle S^2 \rangle$ for open-shell systems.

1.2 The Potential Energy Surface

After the separation of the electronic and the nuclear degrees of freedom by applying the BO approximation, the electronic time-independent Schrödinger equation is given by

$$\hat{H}_{el}(\mathbf{r}, \mathbf{R})\phi(\mathbf{r}; \mathbf{R}) = E(\mathbf{R})\phi(\mathbf{r}; \mathbf{R}) \tag{1.9}$$

where the electronic wave function $\phi(\mathbf{r}; \mathbf{R})$ is explicitly dependent on electron positions and parametrically dependent on nuclear positions. The energy of the system $E(\mathbf{R})$ is only dependent on nuclear positions because the nuclei are considered to be moving around in a "mean-field" created by fast-moving electrons. The potential energy surface (PES) is defined as a plot of E versus $\mathbf{R}$. A PES has the same dimensions as the nuclear degrees of freedom, $3N - 6$, where N is the number of atoms in a system. Being a common representation of chemical space, the PES is a conceptual tool for analyzing molecular geometry and reaction dynamics. Studying minima, saddle points

and many other aspects of its landscape reveals various properties of a molecule including stable geometries and the dynamics of chemical transformations.

For small systems, the PES can be fitted to experimental data or quantum mechanics calculation data. However, it is infeasible to calculate enough single point energies on a PES except for very small ones because of its high dimensionality. In most cases, PESs are not known *a priori*. Usually two types of computational techniques are used to explore a PES, optimization methods and hopping methods.

Optimization methods usually start from a particular point on a PES, then calculate the local gradient and proceed by following that gradient using Newton-Raphson method until convergence. The gradient is the first derivative of energy with respect to nuclear coordinates, given by

$$\frac{dE}{dq_i} = \langle\phi|\frac{d\hat{H}}{dq_i}|\phi\rangle + 2\langle\frac{d\phi}{dq_i}|\hat{H}|\phi\rangle \tag{1.10}$$

In quantum chemical calculations, this equation is often written in a more convenient form [23] that is derived from the HF energy expression,

$$\frac{dE}{dq_i} = \sum_{\mu\nu}\frac{d(\mu|\hat{H}|\nu)}{dq_i}P_{\mu\nu} + \frac{1}{2}\sum_{\mu\nu\lambda\sigma}\frac{d(\mu\nu|\lambda\sigma)}{dq_i}(P_{\mu\nu}P_{\lambda\sigma} - P_{\mu\lambda}P_{\nu\sigma}) - \sum_{\mu\nu}\frac{dS_{\mu\nu}}{dq_i}W_{\mu\nu} \tag{1.11}$$

where

$$\mathbf{W} = \mathbf{PFP} \tag{1.12}$$

where **F** is the Fock matrix and P is the density matrix. The cost of calculating energy gradient in this form scales similarly to the cost of HF energy calculations. In addition, many terms are already calculated in an HF energy calculation and can be reused here. As a result, analytic gradient calculations become routine when exploring *ab initio* PESs. Once gradients are obtained, depending on the task, the optimizer goes downhill to find a stable structure, or uphill when trying to find a transition state geometry. Better-informed methods also calculate the second derivatives of energy with respect to coordinates, the Hessian matrix, in order to gain curvature information and better guide the exploration on a PES. The cost to calculate gradients and optionally the Hessian matrix makes the traveling cost of gradient following methods significant.

Another type of PES exploring techniques is hopping methods. They do not follow gradients as they travel, but hop to other points on the PES. The acceptance of the hop is decided later by pre-defined criteria. These methods typically have no significant traveling cost, but since steps are taken unaware of the shape of the PES, a large number of samples are usually required to yield a reasonable result.

1.3 Transition metals in quantum chemistry

Transition metal complexes play an important role in a wide range of chemistries including catalysis [24], magnetic materials [25], and biological systems [26]. Over the past several decades, computational models and methods for transition metals have become increasingly efficient and accurate; meanwhile computers have become orders of magnitude faster. All these factors have made

the computational study of transition metal chemistry more reliable and predictive. Computational study has become an important driving force in transition metal chemistry. [26–28]

In contrast to organic systems where quantum chemical methods within a single-determinant approximation often yield results of sufficient accuracy for the ground state [29], transition metal systems impose a few unique challenges to quantum chemistry. First, transition metals often have a number of possible oxidation states and spin states. A variety of ligands and ligand-metal interactions further add to the complexity. Second, the introduction of d-orbitals creates dense low-lying near-degenerate states, which undermines the single-determinant approximation. In principle, one can include more determinants and use multi-reference methods to fix this error. However, such methods are usually cost prohibitive because of the factorially growing number of configurations. In recent years, DFT successfully strikes a balance between computational cost and accuracy, and has become routine for investigations of transition metal systems [30].

Despite being relatively accurate for its cost, DFT is still a single-reference method, thus suffering from the ill treatment of static correlation. This is partly remedied by using an unrestricted formalism. The Hartree-Fock method (the discussion around restricted/unrestricted formalism also apply to Kohn-Sham DFT) in its original formalism (also refered to as restricted HF) requires that one orbital have two electrons with opposite spins. The unrestricted formalism instead have different orbitals for different spins. As a result, an unrestricted Slater determinant can be written as a combination of several restricted determinants, and thus recovers some static correlation with a single-reference cost. An unrestricted determinant is often used as a first approximation to the wave function for doublets and triplets because it has lower energies than the corresponding restricted wave functions. While unrestricted HF indeed accounts for some static correlation, it makes the wave function no longer an eigenstate of the $\hat{S}^2$ (spin squared) operator. The expected value of $\hat{S}^2$ is given [31] by

$$\langle \hat{S}^2 \rangle_{\mathrm{UHF}} = \langle \hat{S}^2 \rangle_{\mathrm{Exact}} + N^{\beta} - \sum_{i}^{N} \sum_{j}^{N} |S_{ij}^{\alpha\beta}|^2 \tag{1.13}$$

where N^{α} and N^{β} are the number of α and β electrons respectively and $N^{\alpha} \geq N^{\beta}$, and where

$$\langle \hat{S}^2 \rangle_{\mathrm{Exact}} = \left(\frac{N^{\alpha} - N^{\beta}}{2}\right)\left(\frac{N^{\alpha} - N^{\beta}}{2} + 1\right) \tag{1.14}$$

In Eq. 1.13, $\langle \hat{S}^2 \rangle_{\mathrm{Exact}}$ is the spin square value of the corresponding spin pure state, and $|S_{ij}^{\alpha\beta}|$ is the overlap between α and β orbitals. When α and β orbitals completely overlap, the second and the third term yield zero, thus reducing to the restricted formalism. Difference between α and β orbitals result in higher numbers of $\langle \hat{S}^2 \rangle_{\mathrm{UHF}}$, which indicates undesired mixing of higher spin states. This failure is called spin contamination. Errors associated with the spin contamination can significantly change the energy and distort the PES. These errors are particularly prevalent in geometrically strained and spin-polarized systems, such as transition state structures and transition metal clusters [32]. Chapter 3 discusses a method to treat this error.

1.4 Dissertation Overview

Minima and first-order saddle points are the main points that chemists seek out on a PES, corresponding to the stable geometries and transition state geometries respectively. To find these points efficiently, a variety of PES exploration methods have been developed. The most common ones are optimization methods, where the global or local energy gradient is solved and followed to reach certain stationary points. Another category of methods is surface hopping, where the traveling method from point to point is hopping instead of following gradients. Two representative types of methods are Monte Carlo simulations and heuristic-guided explorations. Chapter 2 reports an automated reaction mechanism generator based on an electron-pushing model, which belongs to heuristic-guided exploration methods. Given reactants and products, this tool systematically generates all reaction pathways between them, filtered by customizable heuristic rules. The variety and customizability of acceptable rules help this approach achieve a balance between the amount of human input and computational cost.

To calculate energy or energy gradients on the surface, various approximate solutions to Schrödinger equation have been developed. In general, more accurate solution requires more computations. Different combinations of accuracy and computational cost construct a spectra of methods, ranging from the less accurate empirical methods, to mean-field methods, and to the more accurate post-SCF methods. Among these methods, Density Functional Theory (DFT) gains the most popularity over the past 3 decades because it achieves relatively high accuracy with mean-field cost for most closed shell systems. For systems with unpaired electrons, DFT suffers from a number of inaccuracies, one of which is spin contamination error (SCE). When using DFT, the PES of such systems will also be distorted. Chapter 3 benchmarks a computational tool developed by my research group that aims to eliminate such error with minimal costs.

Besides stationary points on a PES, minima on the seam of crossing surfaces also attract researchers' attention because they often correspond to a transition point during certain chemical process. For example, during intersystem crossing events, the spin crossover most likely happens on the minimum energy point on the crossing seam of the PESs of two different spin states. Chapter 4 reports an efficient optimization method that optimize to these points. It is challenging because these points are not stationary points on the original PESs, but on the crossing surface, which effectively makes them constrained optimization problems.

Computational tools are also widely used to work closely with experimentalists to aid them in experiment design and result interpretation. In particular, spectroscopy is one of the fields where collaborations between experimentalists and theorists happen most frequently. Chapter 5 showcases a collaboration with experimentalists using state-of-the-art computational modeling methods. In order to study the potential of ZrO_2 being a catalyst for water spliting, the Neumark group carried out a cryo-SEVI photoelectron detachment spectroscopy on ZrO_2 and H_2O adduct. The resulting spectra was high-resolution and rich of vibrational structures. Traditional methods failed to interpret about half of the features in the experimental spectra. Preliminary studies indicated that an umbrella mode plays a role in the spectra. We used a discrete variable representation (DVR) technique to model the double-well mode and shed some light onto the structure of the adduct and some mechanistic insight on the water splitting reaction catalyzed by zirconium oxide.

Chapter 2

An Automated Reaction Mechanism Generator Based on an Electron-Pushing Model

Over the last few decades, the process of determining many unknown reaction mechanism has come to rely on first principles molecular modeling techniques. [33–35] These modeling techniques typically involve exploration and sampling on the potential energy surface (PES), in order to find stationary points along reaction pathways. The PES is a 3N - 6 dimensional hyper-surface (N is the number of atoms in the system), thus a full PES exploration has a substantial cost and is only possible for very small systems. Instead, chemists rely heavily on chemical intuition and prior knowledge to constrain the search space.

While chemical intuition has achieved great successes, it has at least two limitations. First, intuition is not always accurate and often fails in the most complex reaction mechanisms. [36, 37] Second, this process involves substantial human input and is thus prone to errors and suffers from a low throughput rate. To overcome these challenges, automated computer algorithms have been designed to find reaction pathways. [38, 39] Without human intervention, they may require to explore a bigger space on the PES, but if designed well, they can be more efficient than the manual approach.

To automate the reaction path searching process, one needs to first choose a data structure that represents a molecule on a computer, i.e. the molecular representation (MR). An MR can be as minimal as a name, or as complex as a wavefunction. In a reaction path search, MR defines the maximum size of chemical space one needs to search. Different MRs generally fall into two categories: (1) quantum or classic models; [40–45] and (2) graph-based models. [46–52]

Quantum or classical models make use of quantum mechanics or classic mechanics to model a PES. They are aware of the shape of the PES and typically guided by the PES gradient. These methods can be very accurate depending on the underlying theory, but are rather expensive. Maeda and coworkers developed the anharmonic downward distortion following (ADDF) method that finds neighboring transition structures (TS) starting from a local minima [41]. Then the intrinsic reaction coordinate (IRC) method is used to travel to other connecting intermediates of the TSs. These two

steps are repeated to find the complete reaction path for multi-step processes. Maeda and coworkers also developed the artificial force-induced reaction (AFIR) method that finds a reaction path through accelerated chemical reactions with an artificial force [40].

Graph-based models use a graph to represent atomic connectivity (AC) and sometimes lone pairs. These models generally do not contain three-dimensional structure information. Graph-based models are not aware of the shape of the PESs and PES exploration typically involves hopping between stationary points. Starting from an intermediate, one often needs to enumerate multiple possible intermediates and/or TSs that can be hopped to under certain conditions. Therefore finding a reaction pathway is transformed into finding a way of hopping from the reactant to the product on the PES. A few graph-based methods have been developed in recent years. Zimmerman has developed a method called ZStruct based on AC table that enumerates bond formations and breakings [47]. Kim and coworkers proposed a method based on similar ideas to that of Zimmerman, and further incorporated reaction network analysis techniques to reduce the search space [49]. Suleimanov and Green used bond electron matrix (BE) as the MR, taking into account electron change during the enumeration process [50].

Although most aforementioned methods try to achieve zero user interactions during mechanism search, none of them is user-interaction-free. [39] It suggests that pursuing zero user intervention is still too big of a leap at this time. Therefore our method does not pursue this goal, but aims at striking a balance between user input and computational cost.

Another limitation of existing enumeration-based methods is that they only showed that they are able to solve a set of problems, but did not provide the scaling of the computational cost. Since it is always a trade-off between completeness and computational cost for an enumeration method, we argue that a time complexity analysis is necessary so that a user knows if it is practical to solve certain problems with that method.

Here, we propose an automated reaction mechanism generator based on graph representation and enumeration, that mimics an electron-pushing model. It is designed to strike a balance between level of automation and computational cost, which follows the rule that the more restrictions one provides, the less computation required. We provide a thorough time complexity analysis of this algorithm and include a cost reduction analysis for various possible restrictions. The model is then applied to a few textbook reactions to provide an analysis of the model.

2.1 Methods

2.1.1 SMILES

SMILES [53–55], short for simplified molecular-input line-entry system, is an MR in form of an ASCII string. The length of a SMILES string is usually on the same order as the number of atoms in the species it represents. A SMILES string contains all information that can be found from a connection table, including atoms and bonds. It also contains certain stereochemistry information, including chiralty and E/Z structure of a double bond. Compared to a connection table, SMILES takes 50 - 70% less space and contains more information. In addition, SMILES can be canonicalized, that is, it can be made unique so that one species will only yield one unique canonical SMILES. Finally, SMILES is human-readable. With moderate training, a chemist can easily trans-

late both from a chemical structure to SMILES and from SMILES to chemical structures. These properties make SMILES desirable for many applications, including keys for database entries, exchange media of chemical information, etc. The use of SMILES in this work is mostly as a unique identifier for each generated species, as a means to eliminate duplicate species. The most widely-used specifications of SMILES are maintained by Daylight Chemical Information Systems, Inc. and can be found on their website [56].

2.1.2 Open Babel

Open Babel is a chemical toolbox designed to speak the many languages of chemical data. It's an open, collaborative project allowing anyone to search, convert, analyze, or store data from molecular modeling, chemistry, solid-state materials, biochemistry, or related areas. It is also an all-around chemical software library with many built-in classes such as Atom, Molecule, Bond, Residual, etc., and functions such as file format conversion, molecular fingerprints and fast searching, bond perception and atom typing, canonical representation of molecules, 2D to 3D coordinate conversion and forcefield calculations. It is written in standard-compliant C++, which provides fast execution speed. It also provides language bindings for a range of other programming languages, including JAVA, Perl, Python and Ruby, for rapid development and prototyping. Here we highlight some features of Open Babel and describe how they were used extensively in this project.

2.1.2.1 Canonical SMILES

As described in section 2.1.1, SMILES is a string representation of a molecule. For a certain molecule, there are many ways to write a SMILES string that represents it. E.g. for the molecule $CH_2(CH_3)(C_2H_5)$ we can choose either the methyl or the ethyl as the main carbon chain and the other as the branch, giving either "C(CC)C" or "C(C)CC" as the SMILES string respectively, which are both valid SMILES strings but represent the same molecule.

In the enumerating stage of the mechanism generator, it is common occurrence that the generator generates a species that has appeared in previous generations. When this happens, instead of creating a new node in the reaction network, a new edge should be created that connects the current species to the newly-generated but previously-appearing species. However, given the flexibility of SMILES representation, we do not know if a species has appeared before. Canonical SMILES has to be used here in order to identify duplicates and to create a correct edge.

The algorithm that generates a canonical SMILES is not trivial. For example the algorithm must handle the ordering of molecular fragments and the choice and labeling of the main chain, etc. In our benchmark, this algorithm's time complexity scales as approximately $O(n^{0.5})$.

2.1.2.2 File Format Conversion

Open Babel is named "babel" because of its ability to convert between numerous file formats. These file formats include input and output files from various computational chemistry packages (MOPAC, Gaussian, GAMESS), different picture formats (PNG, SVG, ChemDraw), and common formats used in cheminformatics (SMILES, InChI, MOL), etc. Each format also has options that

controls how Open Babel perceives and generates its content, e.g., whether hydrogens are drawn in picture formats.

The mechanism generator makes extensive use of this functionality mainly in three places, drawing species in reaction network, converting between SMILES and the Molecule class in code, and generating input files for computational chemistry packages in order to calculate energies.

When converting a 0D format such as SMILES to input files for energy computation, Open Babel first builds the molecule from scratch following geometrical rules based on the hybridization of the atoms. After an initial structure is generated, Open Babel correct the stereochemistry if it is provided. Finally forcefield methods are used to further minimize the structure and the energy. Available forcefields are MMFF94 [57–61], UFF [62] and GAFF [63].

The construction of the proposed method involves three key components: (1) a numerical representation of the valence electron distribution in the molecule; (2) a defined algorithm for the electron-pushing model and the computational complexity and costs associated with the model. This analysis is critical for assessing the feasibility of the model as a legitimate tool in chemical reaction mechanism discovery and exploration. The subsections below describe each of these elements in turn.

2.1.3 Molecular Representation

Our method uses a BE matrix [64], M, to represent a molecule A. BE matrix is an N×N matrix where N is the number of atoms. Off-diagonal elements M_{ij} gives the bond order between atom i and atom j (the bond order is zero if two atoms are not bonded). A diagonal element M_{ii} is the number of non-bonding valence electrons, i.e., lone pair and radical electrons of atom i. We choose this representation because it contains most 2D information of a molecule, which is what we need for an arrow pushing model.

In addition to the BE matrix, some additional information is maintained, including atomic number, formal charge (FC), and the total bond order (TBO) of each atom. The TBO of an atom is defined as the sum of bond orders of all the bonds involving this atom. Although FC and TBO arrays can be easily computed on-the-fly from BE, our program initiates them when the molecule is created, and update them at each reaction step. This approach reduces the computational cost because FC and TBO are frequently checked during the enumeration process. In fact, it reduces the time cost by a factor of $O(N)$. As an example, the BE of the hydroxide anion is

$$\begin{array}{c} \\ \mathrm{H} \\ \mathrm{O} \end{array} \begin{array}{c} \begin{array}{cc} \mathrm{H} & \mathrm{O} \end{array} \\ \begin{bmatrix} 0 & 1 \\ 1 & 6 \end{bmatrix} \end{array}$$

and the corresponding FC and TBO are [0 -1] and [1 1] (atom order is H and O) respectively.

It is worth noting that this representation use the same matrix for conformers. Therefore it can not represent the complete PES. This limitation will be addressed in future work.

2.1.4 Electron-Pushing Model

The well-known arrow pushing model has been employed in organic chemistry for almost a century. [65] It is widely adopted because of its simplicity and the ability to describe a wide range of reaction mechanisms. Double-barbed electron pushing arrows can be grouped into three categories by its target and destination, which are bond-to-atom, atom-to-bond and bond-to-bond. (For example see Figure 2.1). Arrows in each category make changes to the BE matrix in the same way, i.e., they can be represented by the same delta BE matrix. Bond-to-atom, atom-to-bond and bond-to-bond electron-pushing arrows can be represented by

$$\begin{bmatrix} 0 & -1 \\ -1 & 2 \end{bmatrix}, \begin{bmatrix} -2 & 1 \\ 1 & 0 \end{bmatrix}, \begin{bmatrix} 0 & -1 & 0 \\ -1 & 0 & 1 \\ 0 & 1 & 0 \end{bmatrix}$$

respectively. Subsequently, each elementary reaction, consisting of one or more electron pushing arrows, can be formally represented by the sum of the corresponding delta BE matrices, denoted as a reaction matrix. [64]. Therefore, by enumerating possible reaction matrices, we will visit every minima on the PES that is adjacent to the minima we start with.

To find the reaction pathway between two species, the process is as follows: starting from the reactant described by an BE matrix, we enumerate all possible reaction matrices under certain restrictions, and then we examine the resulting products, mark some of them as valid intermediates according to chemical rules, and then repeat the same enumeration process on each intermediate in a breath-first-search manner, until we find the target product. The complete result is a reaction network represented by a graph, where each node is a valid intermediate (represented by an BE matrix) and each edge is a valid transformation between two intermediates (represented by a reaction matrix). At last, a filter is optionally applied that only keep the paths that lead to the product.

Compared to a atom connectivity based model, the electron-pushing model has a major advantage. It keeps track of electron numbers instead of just connectivity, thus taking into account reactions that do not involve connectivity changes. An example reaction would be the bond-to-atom scheme shown in Figure 2.1 where no connectivity change occurs. As a result, it will be ignored by a bond-forming-and-breaking model but captured by an electron-pushing model.

2.1.5 Time Complexity Analysis

In this section, we analyze the time complexity of the whole enumeration process in terms of big O notation and discuss the time complexity reduction of several restrictions that can be applied in the process.

For each intermediate, reaction matrices are enumerated according to one basic rule: it has to be the sum of one or more delta BE-matrix representing electron-pushing arrows. The process is hence transformed into enumerating electron-pushing arrows. Here we apply one restriction that there can be no more than three electron-pushing arrows in one elementary step. (We denote the maximum number of electron-pushing arrows as **nPairs** thereafter) This constraint is reasonable given that an elementary reaction rarely involves more than three arrows. If an elementary step has more than three arrows, it is most likely that it can be separated into two elementary steps. Such a

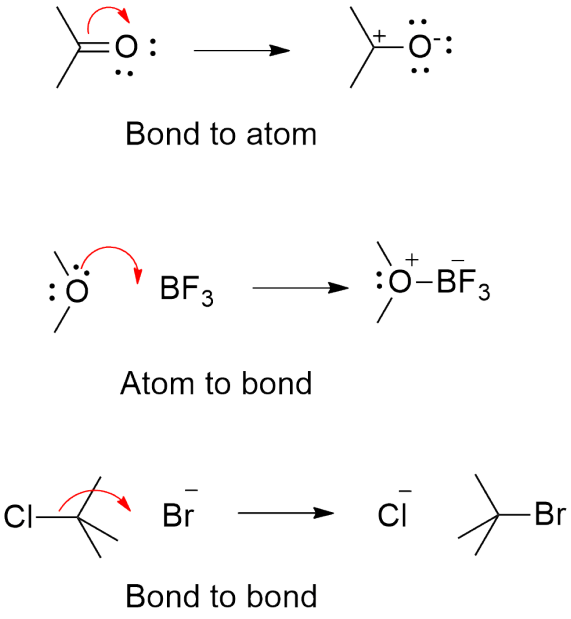

Figure 2.1: Three types of electron arrow in the arrow pushing model

constraint reduces the number of options when enumerating reaction matrices.

It is worth noting that *nPairs* can be easily changed by users. We assume it to be three here to simplify the analysis. Each arrow has an electron donor and an electron acceptor. Each entry in the BE-matrix can be chosen to be a donor or an acceptor, i.e., both atom and atom pair can provide and accept electron. There are $O(N^2)$ entries in the BE-matrix, N being the number of atoms. Therefore each arrow has $O(N^4)$ options to choose from.

Another restriction that naturally applies here is that only non-zero entries in BE matrix can provide electrons. There are approximately $O(N)$ entries that are non-zero (including atoms with lone pairs and bonds), which reduces the arrow choices to $O(N^3)$. Therefore, for each intermediate, allowing a maximum of three electron-pushing arrows, there are approximately $O(N^9)$ reaction matrices to choose from. Although this time complexity is far from ideal, it includes most intermediates and possible reaction pathways.

A cost scaling of $O(N^9)$ is far too steep for the method to be feasible for reactions involving even modest-sized species. There are a few ways for the user to reduce the time complexity. First, if only two electron-pushing arrows are allowed, the complexity reduces dramatically to $O(N^6)$. In fact, this can be done in most cases since most elementary reactions only involve one or two arrows.

Second, one can specify active atoms which limits the number of choices when choosing electron sources and targets. Specifically, only atoms that are active or bonds that have active atoms are subject to change in a transformation. This reduces N directly from the number of atoms to the number of active atoms.

Third, atom configuration rules can be applied as filters to further reduce the time complexity for each intermediate as well as the number of intermediates. These rules are based on concepts from

the Lewis structure model. In a Lewis structure, every atom has an equality that total bond order (TBO) + the number of non-bonding electrons = the number of valence electrons - formal charge. For a certain atom, given its formal charge, only a few TBO numbers are likely to be present in an energetically favorable system. For instance a neutral carbon atom is likely to have a TBO of four or two, while a negatively or positively charged one often has three. These rules are enforced at the stage when the electron acceptor of an arrow is enumerated so that only a fraction of electron acceptors are selected. Here the rule enforcement only takes $O(1)$ which is made possible by the auxiliary information of BE matrices. This dramatically reduces the number of choices for electron acceptor from $O(N^2)$ to effectively close to $O(1)$, as we will show later. Therefore the total time complexity is reduced from $O(N^9)$ to $O(N^3)$. Moreover, it only introduces minimal bias because these observations of atom configuration rules are usually reliable. More importantly, these rules are made accessible to users and easy to comprehend with chemical intuition. Each configuration rule is a mapping between an "atomic number, formal charge" pair and a list of allowed TBOs. A default set of rules comes with the program that is extracted from common organic reactions. A user may or may not choose to change it depending on the system being investigated. In practice, these rules can also be improved iteratively by users based on the feedback from previous results.

So far, we have analyzed the time complexity of enumerating reaction matrices for one intermediate. If there are k intermediates in the reaction network, the total time complexity will be $O(kN^9)$ without any filters. k is affected by several factors. (1) The number of steps allowed in a mechanism. With each added step, the program will expand the reaction network for one more generation of intermediates, i.e., it will do another enumeration of reaction matrix from each intermediate in the last step. The number of intermediates scales exponentially with the number of steps, although duplicate intermediates may reduce this scaling. (2) Filters that are applied by users. For example, atom configuration rules have a direct effect on possible intermediates because those that have undesired Lewis structure will simply not be included as intermediates. However this effect is difficult to quantify.

Another non-trivial and inevitable computation is to eliminate duplicate intermediates in the enumeration process. This operation takes place at every enumerated reaction matrix. It is necessary because in the reaction network many different intermediates could transform into the same species, through different transformations. If we create a new node in the graph for each of such transformations, the size of the graph will grow exponentially and become intractable. Instead, we need to determine if a reaction matrix has produced an intermediate that already exists in the graph. If that is the case, we connect the starting node to the existing node. Secondly, the cost of detecting duplicate molecules is non-trivial because generating a canonical representation of molecule requires significant work. This problem is similar to the graph isomorphism problem, which takes polynomial time. [66, 67] Here we used OpenBabel's built-in canonical SMILES generator which generates a unique and human-readable string for each molecule. We store all unique canonical SMILES and identify duplicates if a newly generated intermediate is already stored.

In summary, $O(N^3)$ time is required to enumerate one electron-pushing arrow in a system of N atoms, without applying any filters. Well-constructed atom configuration rules can reduce this cost to $O(N)$. Assuming this cost is $O(N^a)$, and that we allow p arrows in one elementary step, that we only choose m active atoms, and that k intermediates are produced in the reaction network, the enumeration cost, or the number of enumerated reaction matrices scales as $O(k{*}m^{p*a})$. Furthermore,

if we assume the deduplication cost to be $O(m^d)$ for each enumerated reaction matrix, the end-to-end cost will scale as $O(k * m^{p*a}(1 + m^d))$. This analysis should also apply to other enumeration methods based on chemical heuristics of bond-making and bond-breaking, such as Zimmerman's [47] and Kim's [49] schemes.

2.2 Results & Discussion

Benchmark calculations were run on a production cluster equipped with dual 6-core 2.60 GHz Intel Xeon processors. All calculations were carried out using one core.

In the following case studies, we apply our method to a few reactions with well-accepted mechanisms. Then, we analyze the generated reaction network and compare with the accepted mechanism. At the end, we report a time complexity analysis.

2.2.1 Substitution Reaction

Substitution reaction is a classic textbook reaction and is ubiquitous in Organic Chemistry. A substitution reaction on a carbon atom can occur via two mechanisms, S_N1 and S_N2. Here we applied our method to the reaction

$$CH_3CH_2Cl + Br^- \longrightarrow CH_3CH_2Br + Cl^-$$

The atom configuration rules shown in Table 2.1 were used and *nPairs* and *maxStep* were set to 3 and 2 respectively at first. These parameters were chosen to include the most number of intermediates. The result was a three-layered graph (due to the maxStep=2 constraint) with the reactant and the product being the top and bottom layer respectively, and 32 intermediates in the middle layer. Every intermediate is connected to both the reactant and the product, and the reactant and the product are directly connected as well. The complete graph is omitted here due to its size (See a complete list of intermediates in Figure S1), but some representative intermediates are shown in Figure 2.2. Figure 2.2.a is the S_N1 mechanism, Figure 2.2.b is a C-H bond dissociation. Figure 2.2.c involves a C-Cl bond dissociation and carbon gets the electron pair, which is unlikely. Figure 2.2.e involves a 3-pair mechanism since we allow three electron pairs to move in the settings. Note that the graph also includes a direct pathway between the reactant and the product, representing the S_N2 mechanism. Besides the S_N1 and S_N2 mechanism, this set of configuration rules generates 31 unlikely pathways, most of which contain carbanion or proton. If we are certain that these intermediates are unlikely to form, we can easily exclude them by deleting the corresponding configuration rules. Figure 2.3 shows the complete reaction network under the atom configuration rule set 2 in Table 2.2. The number of intermediates decreased from 32 to 4, which is small enough to carry out manual inspections. If we go further by not allowing carbon-carbon double bond in intermediates, we will only have the S_N1 and the S_N2 mechanism.

2.2.2 Diels-Alder Reaction

The Diels-Alder reaction is a classic organic reaction that involves 4+2 cycloaddition. Three pairs of electrons are involved in this reaction. Therefore, we expect to find the accepted mechanism

		C^-	3	Cl^-	0	Br^-	0
H	1	C	4	Cl	1	Br	1
H^+	0	C^+	3			Br^+	2

Table 2.1: Atom configuration rule set 1 used for substitution reaction. The numbers are the allowed coordination numbers for each atom type.

				Cl^-	0	Br^-	0
H	1	C	4	Cl	1	Br	1
		C^+	3			Br^+	2

Table 2.2: Atom configuration rule set 2 used for substitution reaction. The numbers are the allowed coordination numbers for each atom type.

only when *nPairs* is set to 3. *maxStep* is set to 2 even though this is a one-step reaction, because that we want to include possible two-step mechanism, and also because otherwise the reaction network would be only an arrow connecting the reactant and the product. We first used the configuration rule in Table 2.1 but the calculation kept running for more than one hour without a result. This is because this system has 16 atoms and both carbon and hydrogen are highly reactive according to the configuration rules used, resulting in a long running time. (See the Time Complexity Analysis Section) Since neither C^- nor H^+ are expected to be involved in the mechanism, we used configuration rule set 2 in Table 2.2, which disabled those two species. This run generated 32 intermediates. Some representative ones are shown in Figure 2.4. Again, the one-step 4+2 cycloaddition mechanism was revealed in the reaction network by one arrow directed connecting the reactant and the product. Since hydrogen atoms are not involved in the 4+2 cycloaddition, we apply an addition constraint that only the 6 carbon atoms are active atoms in the mechanism searching process. The result is shown in Figure 2.5. This run only included 5 intermediates plus the 4+2 cycloaddition mechanism.

The results on the addition reaction and the Diels-Alder reaction show the effectiveness of applying constraints in order to filter unwanted intermediates and confine search space. Another thing to note is that these two reactions have relatively simple mechanisms, and all above calculations, except the Diels-Alder run using configuration rule set 1, finished within a minute.

2.2.3 Claisen Ester Condensation

The Claisen ester condensation reaction is a carbon-carbon bond forming reaction that occurs between two esters or one ester and another carbonyl compound in the presence of a strong base, resulting in a β-keto ester or a β-diketone. [68] It is a classic textbook organic reaction widely used to form a new carbon-carbon bond in synthesis, with a fairly complex mechanism. The accepted mechanism [69] is shown in Figure 2.6. We applied our method to this reaction.

We examined different combinations of input parameters for this reaction, including *maxStep*, whether carbanion and proton are allowed, and different range of active atoms and *nPairs*. Table 2.3

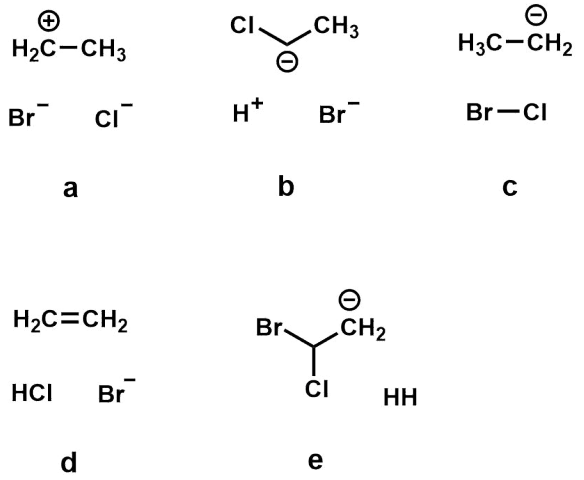

Figure 2.2: Some representative intermediates from the substitution reaction run using configuration rule set 1.

No.	maxStep	C^-/H^+ allowed	Active atoms	nPairs	No. intermediates	No. edges	mechanism found	time/s
1	3	yes	1-2, 5-8	2	35	148	yes	0.85
2	2	yes	1-2, 5-8	2	8	17	yes*	0.33
3	3	no	1-2, 5-8	2	16	60	no	0.83
4	2	no	1-8	3	75	151	yes*	225
5	3	no	1-8	3	254	8464	yes*	3634

Table 2.3: The results of Claison condensation with different sets of parameters. The labels for active atoms are those shown in Figure 2.6.

provides a summary of the results.

The accepted mechanism requires 3 steps, involves a carbanion and 6 atoms, and only has 2-electron-pair elementary steps. Trial 1 set the parameters as such, and the accepted mechanism was found in the generated reaction network, among 35 intermediates and 148 edges. When *maxStep* is set to 2 (trial 2), the search can only find a simplified mechanism (Figure 2.7) where electron movement d and e in Figure 2.6 are omitted. These electron movements are "redundant" in a sense that they describe a pair of electron going from the carbonyl π-bond to oxygen at the end of a step and immediately returning to the carbonyl double bond at the start of the next step. Trial 3 turned carbanion off and produced a network about half the size of trial 1, but none of them are close to the accepted mechanism. Trial 4 included both carbonyl group as active atoms and allowed 3-electron-pair elementary steps, and found another similar mechanism (Figure 2.8) as a result. Instead of forming a carbanion, the mechanism included a redundant process described above that is similar to arrow d and e in Figure 2.6.

As for computational cost, all trials took minimal time to finish except trial 5, where 254 intermediates and 8464 edges were included in the graph. This suggests a high scaling of computational cost.

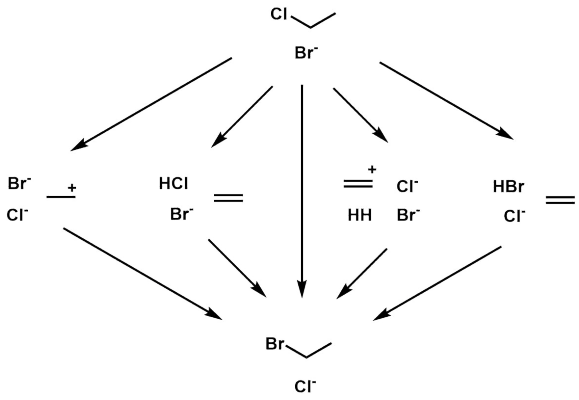

Figure 2.3: The complete reaction graph from the substitution reaction run using configuration rule set 2.

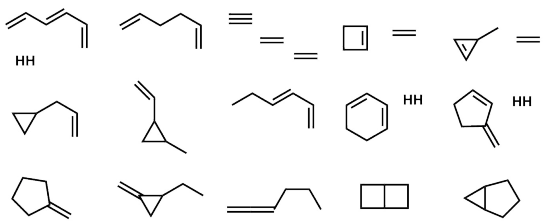

Figure 2.4: Representative intermediates from the diels-alder run using configuration rule set 1.

2.2.4 Time Complexity benchmark

In this section, we first benchmark our time complexity analysis by measuring the practical scaling of our algorithm. The scheme of the benchmark is that we choose a reaction, add atoms to the reacting system without changing the mechanism and measure how running time increases as the system grows. The test systems we use are ethanol, acetaldehyde, and ethene + hydrogen bromide, representing elimination, keto-enol tautomerization, and addition reactions respectively. These reactions are chosen mainly because of their simplicity, so that it does not take too much time when we increase the number of atoms in the system for testing purpose. We vary *nAtom* by adding terminal methyl groups to the carbon chain. For example in the ethanol series we have ethanol, 1-propanol, 1-butanol, etc. Here we mark all atoms as active.

The atom configuration rules used in the benchmark are shown in Table 2.4. Empty values mean the corresponding atom and formal charge pairs are not enabled. All tests successfully generated the accepted mechanism. The total running time is sometimes divided into the enumeration part and the deduplication part in this section. Here enumeration time refers to the total time spent on enumerating reaction matrices from intermediates. Deduplication time refers to the total time spent on converting the resulting species from each reaction matrix, to canonical SMILES.

Figure 2.9 shows the average numbers of possible electron donors and acceptors at enumer-

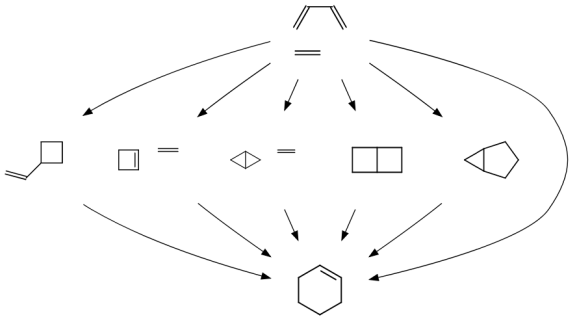

Figure 2.5: Generated reaction network for diels-alder reaction with configuration rule set 2 and only 6 carbon atoms selected as active atoms.

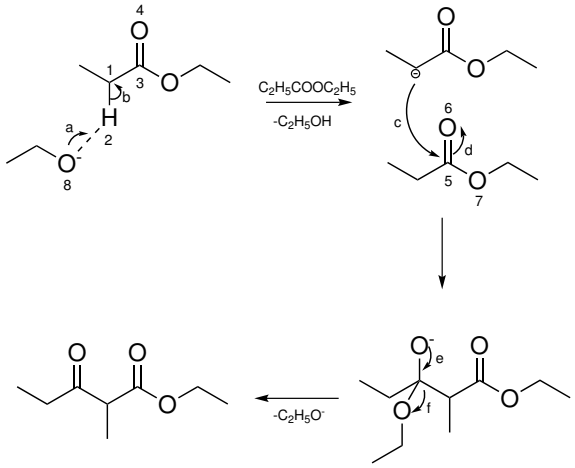

Figure 2.6: The accepted Claisen condensation mechanism.

ation time, measured with *nPairs* set to 2, for the addition reaction set. This demonstrates the effectiveness of atom configuration rules, which, as discussed above, formally reduce the scaling of enumerating electron acceptors from $O(N^2)$ to $O(1)$. Because one can incorporate well-established rules into the algorithm, we do not view such constraints as unreasonable or necessarily limiting.

Figure 2.10 shows the log-log plot of running time vs *nAtom* for both deduplication and enumeration, measured with *nPairs* set to 2, for the addition reaction set. As a result, deduplication and enumeration scale similarly as around $O(N^5)$. Deduplication scales slightly steeper than enumeration, accounting for about 2/3 of the running time when *nAtom* is 35.

Figure 2.11 and 2.12 show the enumeration time spent on each intermediate with different *nAtom*, when *nPairs* is 2 and 3 respectively, for all three reaction series. Both show a trend of going up then down, and then leveling at the end. This is different from our expectation, which anticipated $O(N^3)$ and $O(N^2)$ scaling for 3 pairs and 2 pairs respectively. This is largely due to the fact that the growth in *nAtom* is only provided by $-CH_3$ groups which contribute little to the variety

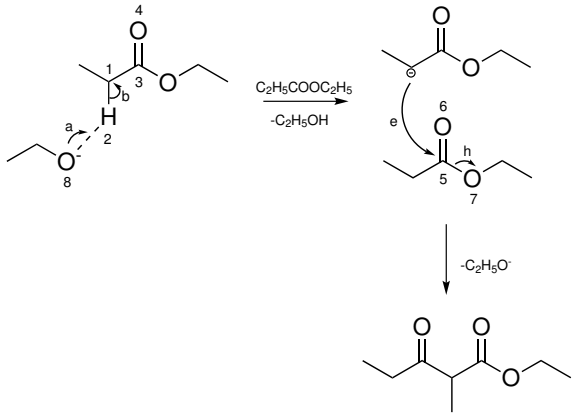

Figure 2.7: A two-step Claisen condensation mechanism found in trial 2.

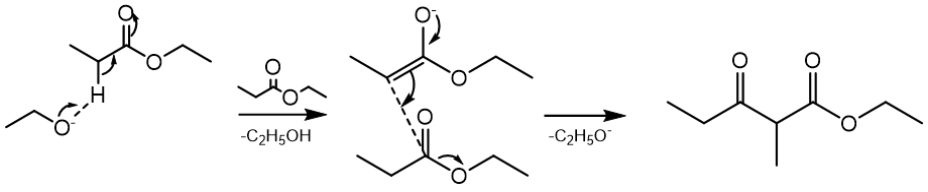

Figure 2.8: An alternative Claisen condensation mechanism found in trial 4.

of reactions that can happen. Also note that it takes two orders of magnitude longer ($\sim$ 1s) for a 3-pair enumeration than a 2-pair enumeration ($\sim$ 0.01s).

Table 2.5 summarizes the scaling of different metrics, including the number of node (nNode), the total number of reaction matrix generated, the time spent on enumeration and the time spent on deduplication.

Based on this analysis, we derive a few key observations. First, for both 2-pair and 3-pair jobs, deduplication time scaling is about $\sim O(N^{0.5})$ higher than the scaling of No. reaction matrices, indicating the time complexity of generating a canonical SMILES is on average $O(N^{0.5})$. Second, for 2-pair jobs, enumeration time and *nNode* have similar scaling, indicating a $O(1)$ time complexity 2-pair enumerations. Whereas for 3-pair jobs, enumeration scales $O(N^2)$ more than nNode, indicating a $O(N^2)$ time complexity for 3-pair enumerations.

				O^-	1	Br^-	0
H	1	C	4	O	2	Br	1
		C^+	3	O^+	3	Br^+	2

Table 2.4: Atom configuration rules used in the timing tests. The numbers are the allowed coordination numbers for each atom type.

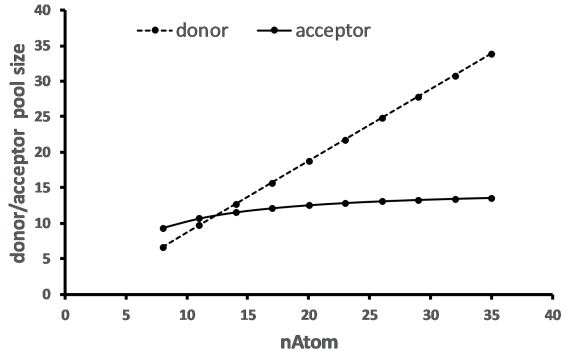

Figure 2.9: The average numbers of possible electron donors and acceptors respectively. Reaction matrices are enumerated by choosing two donors from the donor set and two acceptors from the acceptor set. It was measured for the addition reaction series.

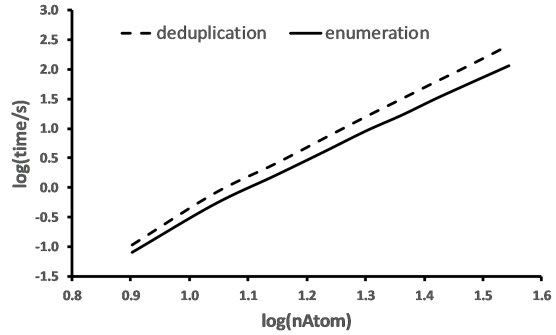

Figure 2.10: The time it took to run the enumeration part and the deduplication part for the addition reaction series. The deduplication scales as $O(N^{5.17})$ and the enumeration scales as $O(N^{4.83})$.

2.3 Conclusion

In this work, we developed an efficient method that automatically searches for possible reaction mechanisms, given reactants and products. The method is based on the widely-used electron arrow-pushing model and therefore can be employed in a wide range of applications. The method is highly customizable and allows user to choose atom-specific configuration rules and other search parameters including the maximum number of elementary reaction steps allowed (*maxStep*), the maximum number of electron pairs allowed to move (*nPair*), and the set of active atoms to be included in the mechanism search.

We applied our method to three reactions, substitution reaction, Diels-Alder reaction and Claisen ester condensation reaction, in order to evaluate the effectiveness and reliability of the method. The program generated the accepted mechanism for all three reactions under various constraints. The "parameter tuning" was shown to be very effective in reducing computational cost while still able to discover the accepted mechanism if applied correctly. In addition, we analyzed

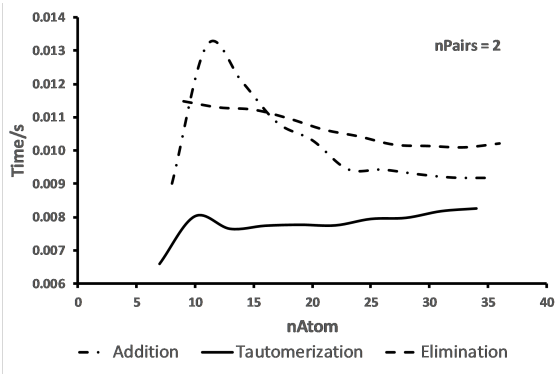

Figure 2.11: Enumeration time spent on each intermediate, plotted with *nAtom*, for the three reaction types respectively. *nPairs* is set to 2.

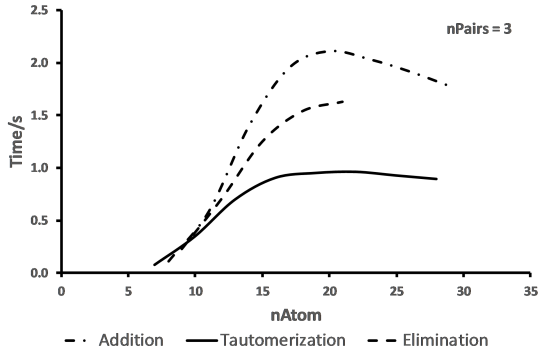

Figure 2.12: Enumeration time spent on each intermediate, plotted with *nAtom*, for the three reaction types respectively. *nPairs* is set to 3.

the time complexity of our algorithm. It is $O(k * m^{p*a})$, k being the number of intermediates in the network, m being the number of active atoms, p being *nPair*, a being the exponent of the exponential scaling of enumerating one electron-pushing arrow. This conclusion, possibly with minor modifications, could apply to all graph or reaction network based enumerating method, such as Zimmerman's [47] and Kim's [49].

This work focuses on providing a method to systematically generate a few most possible mechanisms under user-defined constraints along with its formal complexity analysis rather than predicting the one correct mechanism. Therefore applying thermodynamic and kinetic analysis to further narrow down possible mechanism is out of the scope of this paper.

This method will not work well with metals currently because metal reactions can not always be described by lewis structures and electron-pushing arrows. However the backbone of this algorithm, that is, the iterative enumeration of intermediates and reaction network analysis, still apply to metallic systems. We are currently working on a separate electron-counting scheme that can describe metallic reactions.

Table 2.5: Scaling factor a of different metrics. The number a means the running time scales as $O(N^a)$, N being the number of atoms.

Scaling factor a (as $O(N^a)$)	nNode	No. Reaction Matrix	Enu. time	Dedup. time
Addition, 2 pairs	4.97	4.87	4.83	5.17
Elimination, 2 pairs	4.79	4.57	4.64	4.83
Tautomerization, 2 pairs	4.55	4.57	4.69	5.01
Mean	**4.77**	**4.67**	**4.72**	**5.00**
Addition, 3 pairs	6.65	8.23	8.59	8.68
Elimination, 3 pairs	6.29	8.28	8.61	8.77
Tautomerization, 3 pairs	6.53	7.71	8.51	8.44
Mean	**6.49**	**8.07**	**8.57**	**8.63**

Chapter 3

On the Effect of Spin-Projection on Potential Energy Surfaces

The work described here has appeared as a paper on ChemRxiv [70] and has been submitted to Journal of Chemical Theory and Computation.

3.1 Introduction

Transition metal complexes play an important role in a wide range of chemistries including catalysis [24], magnetic materials [25], and biological systems [26]. Over the past several decades, computational models and methods for transition metals have become increasingly efficient and accurate; meanwhile computers have also become orders of magnitude faster. All these factors have made computational study of transition metal chemistry more wide spread, reliable, and predictive. While computational study has become an important driving force in transition metal chemistry, [26–28] it can be quite difficult to achieve chemical accuracy (error $\sim$ 1 kcal/mol) using available models due to the complex nature of the electronic structure of transition metal compounds. As a result, routine modeling transition metal systems often employs Density Functional Theory (DFT). [30] As a single-reference method, DFT treatment of transition metals lacks a description of static correlation energy, often yielding unsatisfying results and limiting the scope of potential applications. [71]

An alternative and computationally feasible approach that has seen widespread application is broken-symmetry DFT. This scheme employs an unrestricted Kohn-Sham determinant that breaks spin symmetry in the density. Analysis of the broken-symmetry determinant shows that it is a mixture of different spin-pure configurations. Errors associated with this spin contamination can significantly change the energy and distort the potential energy surface (PES). These errors are particularly prevalent in geometrically strained and spin-polarized systems, such as transition structures and transition metal clusters [32, 72, 73]. Nevertheless, in certain cases symmetry breaking yields an improved treatment of static correlation at single-reference cost, though static and dynamic correlation are can become poorly balanced in such cases. [74]

To correct spin contamination error, spin projection methods can be used to remove the con-

taminating spin states from a broken symmetry determinant. When projection is carried out after a spin-contaminated determinant is fully converged, this approach is referred to as projection-after-variation (PAV). PAV scheme often maintain mean-field cost and recover static correlation without needing to explicitly rely on multi-reference methods. In contrast, variation-after-projection (VAP) methods variationally optimize a projected determinant, which will obtain static correlation and some dynamic correlation contributions as well. Examples of VAP schemes include the extended Hartree-Fock (HF) method of Löwdin and, more recently, the projected Hatree-Fock (PHF) method developed recently by Scuseria and co-workers. [75–77] PAV and VAP results are not directly comparable and the formal weaknesses of PAV are well documented. [78] However, PAV allows a clean separation of correlation types, which may present a relatively straightforward pathway for ongoing theory and methods developments.

Approximate Projection (AP), a PAV method proposed by Yamaguchi and coworkers, [79] has shown its usefulness for energy calculations of transition metal complexes and diradicals [80–82]. However, to the best of our knowledge, there has not yet been a systematic investigation of the impact of AP or related projection models on the geometries and subsequent property calculations of transition metal systems. To address this question, we have applied AP to two classes of problems: (1) calculation of exchange coupling constants (J-couplings) for a set of binuclear transition metal complexes; and (2) spin crossover gaps for mononuclear transition metal complexes.

A key aspect of this work is the investigation of geometry optimization effects, i.e., how geometry optimization affects J-coupling and spin crossover gap calculations. It has been reported that full relaxation of the crystal structure in gas phase (without projection) slightly worsens J-coupling results relative to experiment. [83] It seems reasonable to expect that projection may alter the PES and yield different minimum energy structures than these previous reports. To support such studies, our group has extended the use of AP by developing and implementing efficient first and second derivatives, [84, 85] making geometry optimization and force constant evaluations on AP-corrected potential energy surfaces practical.

In this work, we use AP to test how projection methods affect the prediction of two properties important in the characterization of many transition metal complexes. This study gives particular attention to the importance of geometry optimization in such calculations. Specifically, we compare the AP predicted J-coupling and spin crossover gap values with those obtained by conventional broken-symmetry DFT and experiment. We also compare results obtained from different geometries and different approximate density functionals. We show that spin projection can alter PESs and that addressing this consideration in geometry optimizations is beneficial for computational studies of systems affected by spin contamination.

3.2 Computational Details

All electronic structure calculations were carried out using a local development version of Gaussian [86]. Calculations using the AP model employed local implementations of analytic first- and second-derivative programs. [74, 84, 85]

The examination of J-coupling calculations used the test set reported by Peralta and Rudra [87, 88]. Calculations have been carried out using five different functionals - B3LYP [89, 90], LC-ωPBE [91, 92], CAM-B3LYP [93], B3PW91 [94] and ωB97XD [95]. Previous studies have shown

that B3LYP and LC-ωPBE yield the best J-couplings among several density functionals [87,96]. All J-coupling calculations were performed with Ahlrich's all electron triple-ζ valence plus polarization for the metal centers [97] and Ahlrich's double-ζ valence plus polarization basis sets for non-metal atoms [98]. Broken symmetry solutions were generated by using a fragment guess approach to ensure spin-localized initial Kohn-Sham (KS) determinant guesses. All converged KS solutions were verified by stability analysis. [99, 100]

To explore the impact of spin-projection on the types of calculations being explored here, we have chosen to use the AP method as a proxy for other spin-projection models (PAV, in particular). Indeed, recent work from our lab has demonstrated the conditions under which such approaches are rigorously equivalent and those cases for which such models are numerically equivalent. [74] AP calculations using self-consistent field based models, such as HF and DFT, require two converged determinants: (1) a spin-contaminated broken-symmetry state; and (2) a spin-pure high-spin state. Those two determinants are used to assemble an AP energy according to

$$E_{\mathrm{AP}} = \alpha E_{\mathrm{LS}} + (1-\alpha) E_{\mathrm{HS}} \tag{3.1}$$

where

$$\alpha = \frac{\langle S^2_{\mathrm{HS}} \rangle - S_{z,\mathrm{LS}}(S_{z,\mathrm{LS}}+1)}{\langle S^2_{\mathrm{HS}} \rangle - \langle S^2_{\mathrm{LS}} \rangle} \tag{3.2}$$

Subscripts low spin (LS) and high spin (HS) refer to (broken-symmetry) low-spin and (spin-pure) high-spin states. AP geometries were obtained by standard geometry optimization methods. [101] In this work, the phrase "AP geometry" refers to the optimized ground state structure of a complex, whether the ground state corresponds to the AP corrected LS or HS state.

For each approximate density functional, three different geometries were used for calculating J-couplings. The first approach, and perhaps most widely used methodology in similar benchmark studies, determines the J value using published crystal structures. The second source of geometries was the minimum energy structures on the HS or broken-symmetry PESs. The third set of geometries used minimum energy structures located on the AP PESs. In the discussion below, the phrase "UDFT geometry" refers to the lower-energy structure of the HS and broken-symmetry results for each complex, i.e., this refers to a broken-symmetry result when the ground state species is anti-ferromagnetic (AF) and a HS result when the ground state is ferromagnetic (FM).

The effect of projection on computed spin crossover gaps was determined using a test set previously used by Hughes and Friesner. [102] Calculations on this test set employed the B3LYP/6-311G* model chemistry. The PCM solvent model was used with the solvents that were used in the experimental references. [103, 104] This model chemistry is similar to the DBLOC tests by Hughes and Friesner except that the basis set used here is 6-311G*, which yields somewhat better results than the smaller LACVP basis set (see Table C.7 for preliminary data). Calculations of spin crossover gaps involved HS energy calculations with UDFT and LS energy calculations with both UDFT and AP. In all cases, the lowest energy solution found for each spin state/multiplicity was used in evaluating gaps. Again, the stability of all KS determinants was verified. [99, 100]

3.3 Results and Discussion

As discussed above, we have explored the effect of spin projection on the quality of calculated J-coupling values and spin crossover gaps for two commonly used test sets. A particular interest in this work is the dependence of such calculations on the geometries one employs. Specifically, we have used our in-house analytic AP first- and second-derivative codes to examine the extent to which spin contamination degrades the quality of the potential energy surface, predicted minimum energy structures, and ultimately the calculated (vertical) gaps between spin-states. We begin by reporting the results from our tests on a well characterized set of J-coupling parameters corresponding to a collection of nine transition metal complexes. Next, we examine this effect on spin crossover gaps for a set of 65 complexes compiled and reported by Hughes and Friesner. [102]

3.3.1 J-Coupling Tests

Our examination of the role of geometry optimization and spin projection on predicting J-couplings used the test set constructed by Peralta and Rudra [87, 88]. This test set consists of nine medium-sized (40-100 atoms) binuclear transition metal complexes (Fig. 3.1) that have spin-spin coupling between metals facilitated by bridging ligands. Specifically, the test set includes Cu(II), Cr(III), V(IV), Mn(II), Mn(III) and Mn(IV) metal centers and oxygen, nitrogen, and chlorine coordinating atoms. Experimentally, compounds 1-5 are observed to be AF while 6-9 are FM. Modifications were made to compounds 3, 6, 8 and 9 to ensure that the structures were in agreement with published structures [105] or to remove unnecessary water molecules and ions that do not play a significant role in the transition metal complex structures (comparisons can be seen in Table C.1).

Exchange coupling constants are phenomenological parameters describing the strength and sign of spin coupling. Most commonly, exchange coupling parameters, J_{ij}, are extracted from the Heisenberg spin-spin coupling model,

$$\hat{H} = -2 \sum_{i,j} J_{ij} \hat{S}_i \cdot \hat{S}_j \tag{3.3}$$

where J_{ij} is the coupling constant. [106] S_i and S_j represent the $\hat{S_z}$ spin operator for each spin site. Positive J corresponds to FM spin coupling and a HS ground state, while negative J indicates a preferred AF spin coupling and a LS ground state. The magnitude of J indicates the energy gap between two spin states. Experimentally, J is obtained using techniques such as electron paramagnetic resonance (EPR). [107] Using computation, J can be estimated by relating it to the energy difference between HS and LS states described by the Heisenberg Hamiltonian, according to

$$J = \frac{E_B - E_{\mathrm{HS}}}{2S_1 S_2 + S_2}, \; S_1 \geq S_2 \tag{3.4}$$

where E_B is the energy of the broken-symmetry state. This equation is commonly referred to as the non-projected (NP) approach as it does not involve spin projection. [96]

The deficiency of the NP method is that the LS energy typically involves a spin contaminated KS determinant. Addressing this concern, Dai and Whangbo [108] proposed a spin-projected (SP) approach by mapping the broken-symmetry and HS states onto the Heisenberg Hamiltonian, and

Figure 3.1: Nine transition metal complexes used for testing J-coupling prediction.

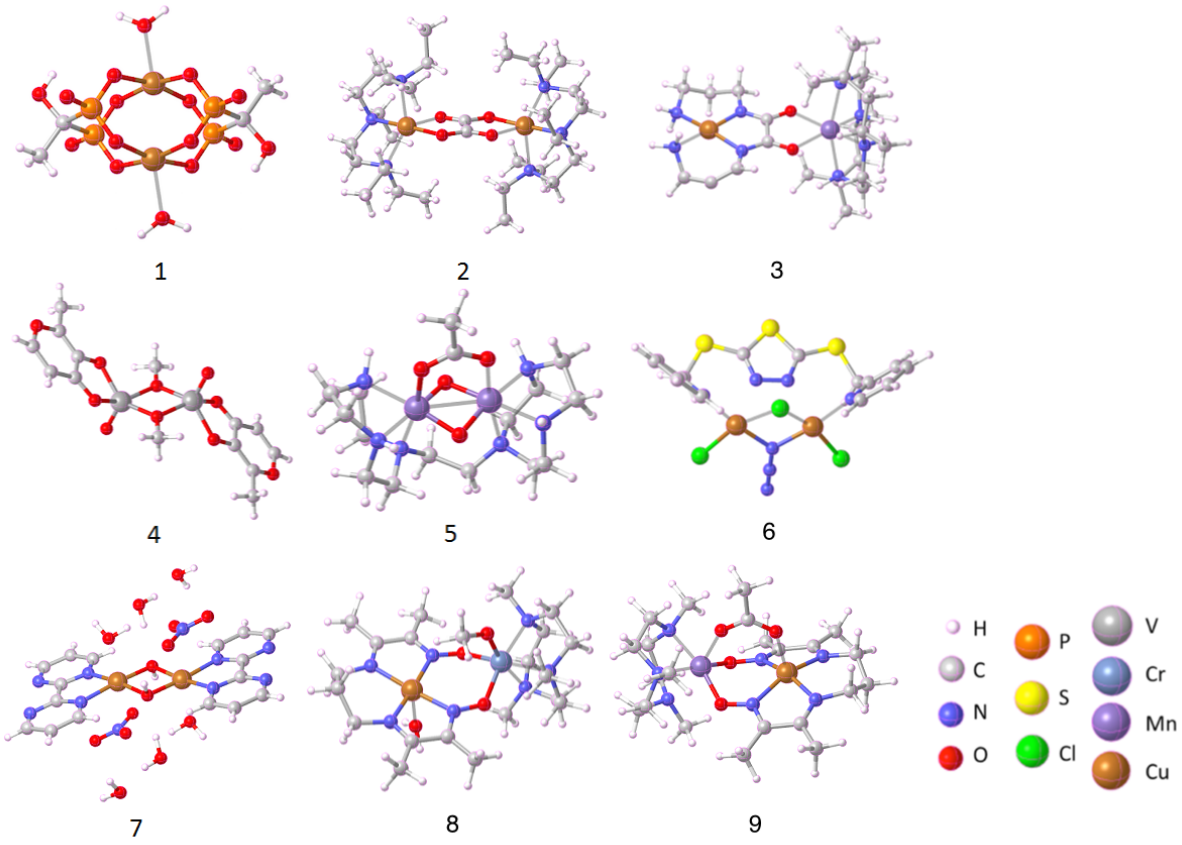

derived the following expression for J,

$$J = \frac{E_B - E_{\mathrm{HS}}}{2S_1S_2} \tag{3.5}$$

Equation (3.4) corrects for the spin contamination of the broken-symmetry result using an approximation for spin projection and will yield a J whose magnitude is necessarily greater than that computed using Eq. (3.4).

The validity of SP and NP approaches depends on the magnitude of spin coupling. In the weak coupling regime, where the overlap between two interacting magnetic orbitals a and b is close to zero, i.e. $\langle a|b\rangle \approx 0$, SP should be chosen. NP tends to perform better in the strong coupling regime, where $\langle a|b\rangle \approx 1$. However, in practice, DFT tends to overestimate the magnitude of J-couplings. [109] NP tends to underestimate the magnitude of J, and when used with DFT, gives better results even in the weak coupling regime. [110, 111]

The AP model smoothly unifies the two limiting cases treated by the SP and NP approaches. The AP model employs the dominant HS contaminant, finds its weight in the broken-symmetry state, removes it from the contaminated energy, and renormalizes the energy to yield a corrected low-spin energy. The exchange coupling parameter in this model is given by

$$J = \frac{E_{\mathrm{AP}} - E_{\mathrm{HS}}}{\langle \hat{S}^2\rangle_{\mathrm{HS}} - \langle \hat{S}^2\rangle_{\mathrm{LS}}} \tag{3.6}$$

where E_{AP} is the AP-corrected LS energy and $\langle \hat{S}^2\rangle_{\mathrm{LS}}$ is the ideal spin-squared expectation value of the pure LS state. In the weak coupling regime, when the broken symmetry solution exhibits a large degree of spin polarization, AP reduces to SP (Eq.3.5). In the strong coupling regime, $\langle S^2\rangle_B$ approaches $\langle S^2\rangle_{\mathrm{LS}}$ and AP reduces to NP.

To quantify the extent of geometric relaxation resulting from these optimization calculations, the root-mean-square-difference-at-maximum-overlap values for the crystal structure, HS, and broken-symmetry LS minimum energy geometries were computed relative to corresponding optimized AP geometries. These RMSD values are shown in Table 3.1. As one might expect, meaningful geometric relaxation is observed when optimizing structures in the gas phase from initial crystal structures. The average RMSD of the crystal structures relative to the AP geometries was 0.48Å. The largest internal coordinate displacements of bond lengths, angles, and dihedrals involving a metal center averaged over the set of nine compounds were 0.09Å, 12.6°, and 34.2°, measured between crystal and AP geometries. On the other hand, HS and broken-symmetry LS geometries differ with AP geometry only slightly (RMSD $\sim 0.01 - 0.02$Å), which suggests that AP energy correction only slightly changes the potential energy surface, in agreement with prior findings. [112] This observation indicates that – at least for the test set considered here – the geometries are not very sensitive to the presence of spin contamination.

For example, Fig. 3.2 compares the crystal structure and optimized AP geometry for Compound 3. Overall, the three-dimensional structure remains qualitatively unchanged, but evaluation of specific internal coordinates shows a few key changes. The most notable change is in the copper-nitrogen bond distance labeled in Fig. 3.2, which decreases during geometry optimization on the AP PES by more than 0.2 Å. The complete set of geometric parameter changes due to geometry

Geometry	1	2	3	4	5	6	7	8	9
Crystal	0.85	0.29	0.39	0.26	0.15	0.44	1.03	0.60	0.38
HS	0.01	0.02	0.02	0.01	0.01	0.02	0.02	0.01	0.02
Broken-Symmetry LS	0.01	0.01	0.00	0.00	0.01	0.01	0.02	0.01	0.00

Table 3.1: RMSD (Å) of crystal, optimized HS and optimized broken-symmetry LS structures relative to corresponding optimized AP geometries.

optimization are given in Table C.2).

Figure 3.2: Comparison of crystal geometry and AP optimized geometry for complex 3 as a representative example of the large geometry optimization effect.

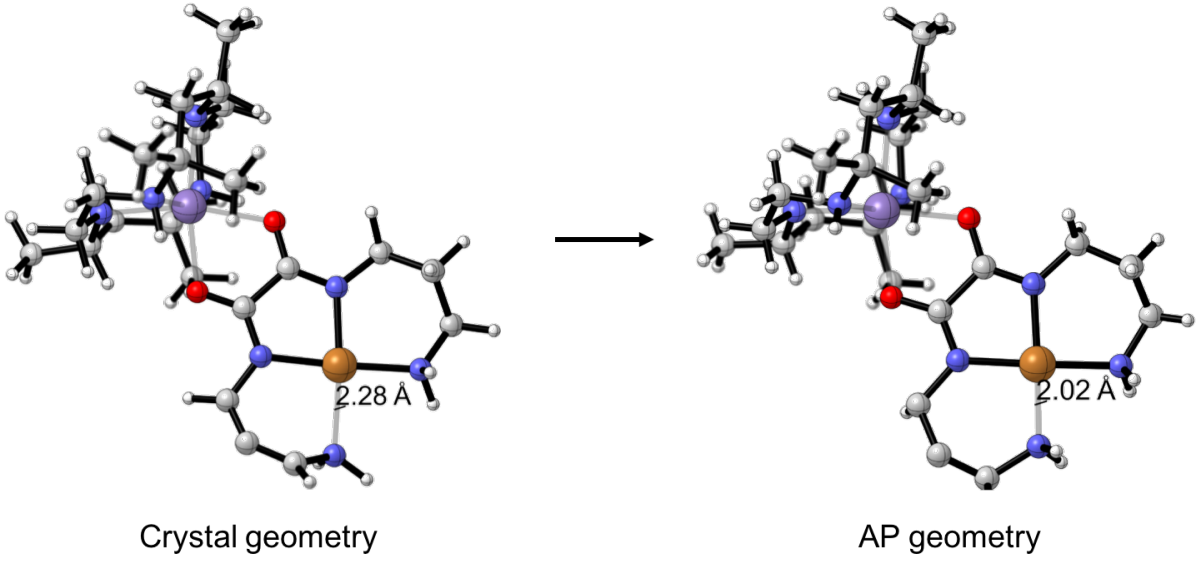

We next investigated the quality of calculated J-coupling parameters by employing optimized AP structures. As described earlier, we considered three different approaches for calculating J-couplings – NP (Eq.(3.4)), SP (Eq.(3.5)), and AP (Eq.(3.6)). Table 3.2 gives J-couplings calculated by Eqs. (3.4)-(3.6) on AP geometries using the B3LYP and LC-ωPBE approximate density functionals. Table 2 also includes experimentally determined J values and calculated expectation values of the S^2 operator for each compound. Results using other approximate functionals and geometries (crystal structures, and HS and broken-symmetry LS minimized energy structures) are provided in the Appendix C. The specific approximate functionals shown here were chosen as representative results.

The two projection methods, SP and AP, gave similar results. This result was anticipated as all of the complexes in the test set exhibit weak coupling between metal centers, in which case the SP and AP expressions agree. With this in mind, we report only NP and AP values in the remainder of this work.

In all cases, calculated J-coupling values had the correct sign, indicating that hybrid func-

Table 3.2: J-couplings (cm^{-1}) calculated by different methods on AP geometry with B3LYP and LC-ωPBE. $\langle S^2\rangle_{HS}$ and $\langle S^2\rangle_{LS}$ are calculated with B3LYP. S square calculated by other DFT functionals are omitted here because they differ by less than 1%.

					B3LYP			LC-ωPBE			Exp
#	S_a	S_b	$\langle S^2\rangle_{HS}$	$\langle S^2\rangle_{LS}$	AP	SP	NP	AP	SP	NP	
1	0.5	0.5	2.00	1.00	-92.7	-93.3	-46.6	-29.5	-29.5	-14.8	-30.9
2	0.5	0.5	2.01	0.99	-114.8	-116.1	-58.1	-69.2	-69.4	-34.7	-37.4
3	2.5	0.5	12.01	6.99	-43.9	-44.1	-36.7	-16.8	-16.8	-14.0	-15.7
4	0.5	0.5	2.02	1.01	-120.8	-121.9	-60.9	-110.2	-110.9	-55.4	-107
5	2	1.5	15.84	3.73	-135.2	-136.4	-109.1	-140.3	-141.4	-113.1	-110
6	0.5	0.5	2.01	0.98	129.0	132.0	66.0	283.4	287.0	143.5	84
7	0.5	0.5	2.00	1.00	115.8	116.1	58.1	105.2	105.3	52.7	57
8	1.5	0.5	6.03	3.03	34.2	34.2	25.6	23.6	23.6	17.7	18.5
9	2	0.5	8.83	4.82	112.4	112.7	90.2	61.0	61.4	49.1	54.4

tionals (with or without range separation included) predict the correct ground state. In addition, NP J-couplings are always smaller in magnitudes than those obtained by AP. This result is in line with the suggestion that NP counteracts the overestimation of J-couplings by DFT. [113–115]

Comparing NP and AP results with experimental data, it is clear that the non-projection approach yields better agreement with experiment. Importantly, it should be kept in mind that the magnitudes of the J-couplings in these systems are much smaller than the typical error limits associated with DFT calculations. Assuming a normal distribution for the error in DFT energy calculations, the calculated HS and LS energies can be related to the *true* energies according to,

$$E_{\mathrm{LS}}^{\mathrm{calc}} = E_{\mathrm{LS}}^{\mathrm{true}} + X_{\mathrm{LS}} \tag{3.7}$$

and

$$E_{\mathrm{HS}}^{\mathrm{calc}} = E_{\mathrm{HS}}^{\mathrm{true}} + X_{\mathrm{HS}} \tag{3.8}$$

where X_{LS} and X_{HS} are two scalar values taken from a normal distribution with deviation σ. Invoking Eq.(3.4) we obtain

$$J_{\mathrm{NP}}^{\mathrm{calc}} = J_{\mathrm{NP}}^{\mathrm{true}} + \frac{\Delta X}{2S_1S_2 + S_2} \tag{3.9}$$

where

$$J_{\mathrm{NP}}^{\mathrm{true}} = \frac{E_{\mathrm{LS}}^{\mathrm{true}} - E_{\mathrm{HS}}^{\mathrm{true}}}{2S_1S_2 + S_2} \tag{3.10}$$

and $\Delta X = X_{\mathrm{HS}} - X_{\mathrm{LS}}$. ΔX is the difference between the two normally distributed variates and thus follows a normal distribution of zero mean and 2σ variance. Thus, the NP error, ϵ_{NP}, is given by

$$\epsilon_{\mathrm{NP}} = \left|J_{\mathrm{NP}}^{\mathrm{calc}} - J_{\mathrm{exp}}\right| = \left|J_{\mathrm{NP}}^{\mathrm{true}} - J_{\mathrm{exp}} + \frac{\Delta X}{2S_1S_2 + S_2}\right| \tag{3.11}$$

Similarly, the AP J-coupling error, ϵ_{AP}, can determined by using Eq.(3.6) and is given by

$$\epsilon_{\mathrm{AP}} = \left|J_{\mathrm{AP}}^{\mathrm{calc}} - J_{\mathrm{exp}}\right| = \left|J_{\mathrm{AP}}^{\mathrm{true}} - J_{\mathrm{exp}} + \frac{\Delta X}{2S_1S_2}\right| \tag{3.12}$$

$\Delta J_{AP} = J_{\mathrm{AP}}^{\mathrm{true}} - J_{\mathrm{exp}}$ is the difference between the J value calculated using the *true* LS and HS energies with the AP scheme and the experimentally measured J. For the cases studied here, the magnitude of ΔJ_{AP} is similar to, or much smaller than, the magnitude of the experimental J value. The same observation holds for $\Delta J_{NP} = J_{\mathrm{NP}}^{\mathrm{true}} - J_{\mathrm{exp}}$. If one assumes these two parameters are given by the same small value $\Delta J_{AP/NP} \approx 100$ cm^{-1} (0.286 kcal/mol), σ is 1 kcal/mol, and S_1 and S_2 are 0.5 (as is the case for most singlet-triplet splittings) we have that

$$\epsilon_{\mathrm{NP}} = |\Delta J_{NP} + \Delta X| \tag{3.13}$$

and

$$\epsilon_{\mathrm{AP}} = |\Delta J_{AP} + 2\Delta X| \tag{3.14}$$

Within the range $\Delta X > 0 \cup \Delta X < -\frac{2}{3}\Delta J_{AP/NP}$, $\epsilon_{\mathrm{NP}} < \epsilon_{\mathrm{AP}}$ is always true. In a normal distribution, the probability of ΔX being in that range is calculated to be 0.9244. For other fair assumptions of ΔX, $\Delta J_{AP/NP}$, S_1 and S_2 values, the probability of $\epsilon_{\mathrm{NP}} < \epsilon_{\mathrm{AP}}$ remains close to 1 as long as $\Delta J_{AP/NP}$ is significantly smaller than ΔX. In other words, if a calculated value is normally distributed around the true value with a deviation well beyond its magnitude, a method that consistently results in values of smaller magnitude will yield statistically better results.

The geometry dependence of J-couplings was further examined by calculating NP and AP coupling values using crystal geometries and those found from geometry optimizations on the UDFT and AP PESs. As a representative case, Table 3.3 reports the J values calculated by LC-ωPBE. Overall, J-coupling dependence on geometry is very small. Relative to the crystal structure results, UDFT geometries resulted in slightly improved J-couplings with the NP method but slightly degraded results using the AP method. Using AP geometries, on the other hand, yielded somewhat improved results relative to UDFT geometry by both AP and NP methods, especially when compound 6 is excluded.

Figure 3.3 shows MAE's of calculated J-couplings for four different approximate density functionals using three difference types of geometries and evaluating J using both AP and NP approaches. In agreement with previous work by Phillips et al., we found that range separated approximate functionals are found to be superior to global hybrid functionals in predicting J-couplings. [116] We note, that that work suggests that the improvement of such results using range separated functionals (relative to global hybrids) is not an effect of range separation. Instead, it appears that the improved agreement with experiment is due to the inclusion of more HF exchange. Our results also show that using geometries optimized on AP PESs, J-coupling values calculated with range separated functionals reduced the MAE by 50-60% (excluding complex 6) with both AP and NP methods, relative to B3LYP results. The three range-corrected functionals behave similarly. Geometry dependence, although small, can be seen clearly where AP and UDFT geometries give better agreement with experiment than crystal structure with the range separated functionals considered.

Table 3.3: J-couplings (cm^{-1}) on crystal, UDFT and AP geometries calculated by AP and NP methods using LC-ωPBE.

	J(AP)			J(NP)			
Geometry	Crystal	UDFT	AP	Crystal	UDFT	AP	Exp
1 Cu^{II} Cu^{II}	-43.6	-27.4	-29.5	-22.5	-13.7	-14.8	-30.9
2 Cu^{II} Cu^{II}	-56.9	-66.6	-69.2	-29.4	-33.4	-34.7	-37.4
3 Mn^{II} Cu^{II}	-16.3	-16.7	-16.8	-13.9	-13.9	-14.0	-15.7
4 V^{IV} V^{IV}	-61.1	-83.4	-110.2	-31.5	-41.8	-55.4	-107
5 Mn^{III} Mn^{IV}	-147.3	-135.8	-140.3	-121.5	-109.3	-113.1	-110
6 Cu^{II} Cu^{II}	300.9	338.0	341.3	157.4	171.5	173.3	84
7 Cu^{II} Cu^{II}	115.2	109.4	109.5	59.0	54.7	54.8	57
8 Cu^{II} Cr^{III}	23.2	24.2	24.3	17.8	18.2	18.2	18.5
9 Cu^{II} Mn^{III}	60.6	64.5	65.4	49.7	51.7	52.4	54.4
MAE[1]	44.7	45.1	43.8	20.7	20.2	18.8	
MAE[1] w/o 6	23.1	18.9	16.0	14.1	11.8	10.7	
VarE[2] w/o 6	22.0	17.7	19.1	23.5	20.8	16.4	

[1]MAE is the mean absolute error relative to experimental values.

[2]VarE is the variance of the errors.

Figure 3.3: MAE's of the J-couplings of complexes 1-9 (excluding 6) calculated with four different functionals by AP and NP methods on Crystal and AP geometry.

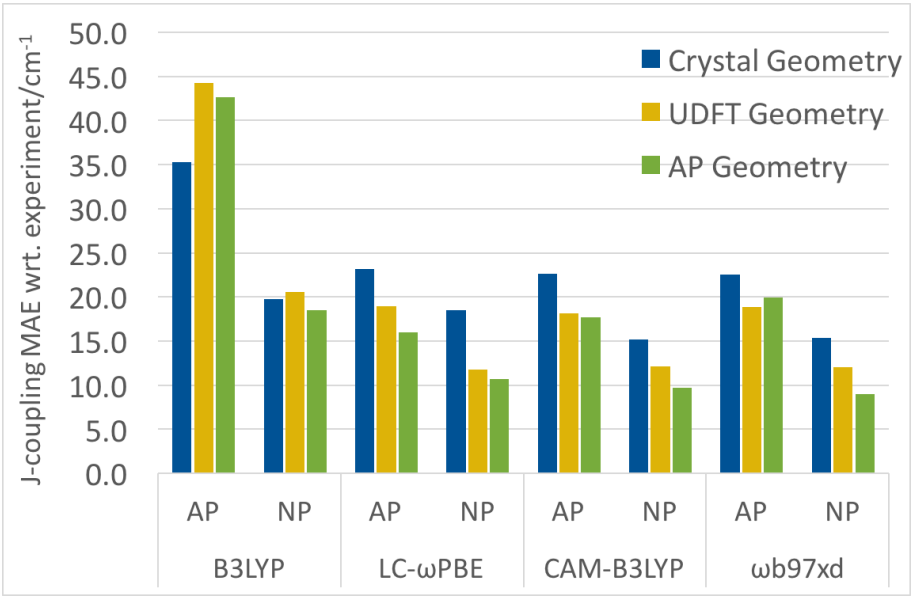

3.3.2 Spin Crossover Gaps

As a second test of the impact of spin-contamination on geometry and spin-state energy differences, we explored the role of spin-projection in calculating spin crossover gaps in a broad set of transition metal compounds. The set of spin crossover species was used by Hughes and Friesner in the development of their DBLOC model. [102]. This test set includes 65 octahedral first-row mononuclear transition metal complexes, including V, Cr, Mn, Ni, Fe, Co with oxidation states ranging from +2 to +4, total charge ranging from -4 to +4, multiplicity ranging from 1 to 6, and total number of valence d-shell electrons ranging from 2 to 8. The set is divided into several subgroups (*transition types*) based on the number of valence electrons and transition type (see Table 3.4). For example, for each member of the t_{2g}-t_{2g} d^3 transition type group a t_{2g} electron is excited to another t_{2g} orbital.

Table 3.4: Transition types and associated transition diagrams of the 65 complexes in the Hughes and Friesner test set.

transition type	# of complexes	transition diagram
t_{2g}-t_{2g} (d^3)	10	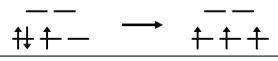
t_{2g}-t_{2g} (d^4)	2	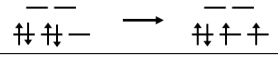
t_{2g}-t_{2g} (d^2)	3	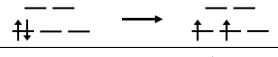
t_{2g}-e_g (d^5)	2	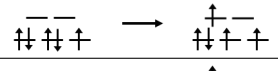
t_{2g}-e_g (d^6)	9	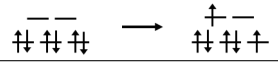
*t_{2g}-e_g (d^6)	11	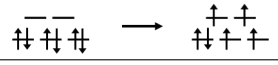
*t_{2g}-e_g (d^7)	2	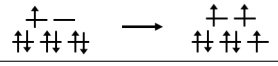
e_g-e_g (d^8)	20	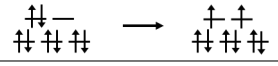
e_g-t_{2g} (d^5)	6	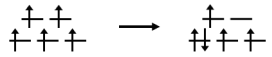

* These two groups are experimentally observed to have very small spin crossover gaps.

To determine the dependence on geometry optimization in spin crossover calculations, spin crossover energies were calculated for each compound in the test set using the same three types of geometries as in the exchange coupling calculations described above: (1) crystal structures; (2) optimized UDFT geometries; and (3) AP optimized geometries. The complete collection of these results is given in Tables C.8 and C.9, including spin crossover gaps calculated on different geometries and by different projection methods, with and without inclusion of (implicit) solvent effects. These combinations of geometry and projection method (and their notations) include crystal structure without projection methods (Crystal), UDFT geometry without projection (UDFT) and with AP (UDFT//AP), and AP geometry with AP (AP//AP).

Table 3.5 summarizes these results aggregated according to the nine transition types described earlier. MAEs for each transition type and calculation approach are provided in the table. The MAE of spin crossover gaps computed on the crystal structures (over all complexes) is 14.80 kcal/mol. UDFT optimization reduced the total MAE to 11.45 kcal/mol. By applying AP, UDFT//AP produced significantly better results with the MAE reduced to 5.83 kcal/mol. AP//AP values obtained by optimizing geometries on AP PES did not yield further significant improvements.

Table 3.5: Average errors (kcal/mol) of spin crossover gap calculations on different geometries with B3LYP/6-311G(d) grouped by transition type, along with DBLOC errors and group-averaged α values (defined by Eq. (3.2)) and their standard deviation.

transition	# of	Error wrt. Exp.					α
type	complex	Crystal	UDFT	UDFT//AP	AP//AP	DBLOC	(Std. Dev.)
t_{2g}-t_{2g} d^3	10	12.83	12.54	1.21	1.20	2.21	1.50 (0.00)
t_{2g}-t_{2g} d^4	2	23.54	23.49	12.20	13.38	2.47	1.96 (0.03)
t_{2g}-t_{2g} d^2	3	12.90	12.83	1.14	1.32	1.77	1.99 (0.01)
t_{2g}-e_g d^5	2	10.40	1.91	2.12	6.28	2.88	1.01 (0.00)
t_{2g}-e_g d^6	9	4.82	3.78	3.78	3.61	1.54	1.00 (0.00)
*t_{2g}-e_g d^6	11	22.99	19.49	19.49	19.06	3.63	1.00 (0.00)
**t_{2g}-e_g d^7	2	8.68	5.50	5.53	5.33	2.73	1.00 (0.00)
e_g-e_g d^8	20	17.25	12.70	2.76	2.82	1.94	1.99 (0.01)
e_g-t_{2g} d^5	6	12.26	2.57	3.05	2.40	3.10	1.02 (0.06)
MAE total	65	14.80	11.45	5.83	5.92	2.38	
MAE ($\alpha > 1$)	43	14.92	11.24	3.03	3.22	2.19	

* ** These two groups are experimentally observed to have very small spin crossover gaps.

Despite the overall improvement from UDFT to UDFT//AP, no significant difference between them is observed in the t_{2g}-e_g (d^6), *t_{2g}-e_g (d^6) and **t_{2g}-e_g (d^7) transition types. This can be understood by considering the AP α parameter defined by Eq. (3.2), which represents the degree of contamination in a broken symmetry determinant. The closer α is to one, the less contaminated a solution. Therefore, AP will have little (or no) effect on spin crossover gaps when α is close to 1.0.

On the other hand, AP correction dramatically reduced the errors of all $\alpha > 1$ cases, including t_{2g}-t_{2g} (d^3), t_{2g}-t_{2g} (d^4), t_{2g}-t_{2g} (d^2) and e_g-e_g (d^8), from 11.24 to 3.03 kcal/mol (see last row of Table 3.5). Using AP these transition types all yielded relatively accurate results except for group t_{2g}-t_{2g} (d^4), where the error is decreased by nearly a factor of two. Nevertheless, the error is still relatively large (12.20 kcal/mol). Exploring the results for the members of the d^4 transition type transition type group individually, it was apparent that complex mn2p2pameth2 significantly skews the results. This compound features a Mn(III) center with two bonding oxygens and four coordinating nitrogens. Calculations on this specific test compound yielded an error of 34.85 kcal/mol without AP and 24.31 kcal/mol with AP.

AP behaved particularly well for group t_{2g}-t_{2g} (d^3), which is shown in detail in Table 3.6. Crystal and UDFT values were only slightly different, meaning that geometry changes impose similar effects on HS and LS energies and thus the change in spin crossover gap is negligible. The MAE obtained on crystal structures is 12.83 kcal/mol, which was significantly improved to 1.21

Table 3.6: Spin crossover gaps (kcal/mol) and their errors (in parethesis) with respect to experiments on crystal, UDFT, and AP geometries calculated by B3LYP/6-311G(d) for group t_{2g}-t_{2g} (d^3).

Complex (error)	Geometry//Projection				Exp.
	Crystal	UDFT	UDFT//AP	AP//AP	
crf6	24.80 (15.57)	25.40 (14.97)	38.09 (2.28)	38.33 (2.04)	40.37
cr223tetch2	24.18 (12.35)	23.78 (12.75)	35.60 (0.93)	36.24 (0.29)	36.53
crccsime36	20.94 (12.58)	21.49 (12.03)	32.23 (1.29)	32.63 (0.89)	33.52
crcn6	21.18 (9.82)	22.96 (8.04)	34.36 (3.36)	35.68 (4.68)	31.00
crcyclamncs2	23.11 (11.43)	23.22 (11.32)	34.79 (0.25)	35.14 (0.60)	34.54
cren3	25.38 (13.29)	25.81 (12.86)	38.65 (0.02)	38.83 (0.16)	38.67
crnh34cl2	25.15 (11.80)	24.86 (12.09)	37.24 (0.29)	37.83 (0.88)	36.95
crnh36	25.78 (13.37)	25.98 (13.17)	38.92 (0.23)	39.29 (0.14)	39.15
crox3	23.77 (12.76)	23.86 (12.67)	35.76 (0.77)	36.20 (0.33)	36.53
mnf6	25.87 (15.37)	25.78 (15.46)	38.57 (2.67)	39.25 (1.99)	41.24
MAE	12.83	12.54	1.21	1.20	

kcal/mol by using AP. In this case, only LS states were affected by AP because HS states were not spin contaminated. Therefore AP had a substantial impact on the energy gaps. AP//AP values were calculated on AP geometry instead of UDFT geometry, but no significant improvement in spin crossover gap was seen. Both UDFT//AP and AP//AP methods gave better agreement with experiments than DBLOC (1.2 vs 2.2 kcal/mol) in this group.

Calculations without solvent effect were also performed and yielded very similar results. The MAE for UDFT//AP and AP//AP model chemistries were the same within two decimal places, and the MAE of $\alpha > 1$ cases of these two methods were 3.04 and 2.98 kcal/mol (See Table S9). From our results, solvent effect for this test set does not seem to be significant. Overall, AP provides reasonably good results for spin crossover gaps predicted by UDFT.

3.4 Conclusions

This work explored the effect of spin projection on the quality of calculated J-coupling values and spin crossover gaps in transition metal complexes. Furthermore, the dependence of such calculations on geometry has been studied. A widely used test set of J-couplings for nine transition metal complexes was studied with and without applying spin-projection corrections. Our results show that spin-projection does not often result in large geometric changes in the minimum energy structure relative to optimized spin-contaminated unrestricted DFT geometries. However, the use of geometries optimized with the AP method in J-coupling computations using either the spin-projected or non-projected approaches generally results in better agreement with experiment than using unoptimized crystal structure geometries. In addition, NP method was found to perform better than AP method in most cases, rationalized by considering that the magnitude of DFT energy calculation error is much bigger than the that of a typical J-coupling value.

A second set of benchmark tests involved a set of 65 transition metal complex spin crossover gaps. Projection methods were found to be effective for calculating spin crossover energy gaps.

Focusing on a subset of 43 members of this set where the AP model is expected to improve the quality of mean-field calculations showed that AP geometry optimization and energy evaluations leads to very good agreement with experiment. Importantly, these results are similar in quality to the DBLOC model which employs an empirical correction model involving a fitted parameter set.

Overall, the results of this work demonstrate that correcting for spin-projection can improve the performance of DFT calculations of transition metal complex J-couplings and spin crossover gaps. However, for some systems this correction is modest. Also, as expected, the quality of calculations on systems with multiple contaminating spin-states are degraded by the use of the AP model. In such circumstances, more complicated projection models would likely improve calculated results. Nevertheless, this investigation supports the use of the AP model in calculations on molecular systems of the sort considered in this work.

Chapter 4

Efficient Optimization of Minimum Energy (Spin-) Crossing Points

4.1 Introduction

Many chemical processes involve transitions between electronic states that have different electronic spins [117–120]. Of particular interest here is thermal-induced spin crossover processes. They are found in a wide range of chemical reactions such as the predissociation of N_2O [121] and the oxygen-transfer reactions of FeO^+ with H_2 or alkanes. [122] Spin crossover events are formally spin-forbidden in a non-relativistic context. Conveniently and approximately, they are often described in terms of the crossing of two non-interacting energy surfaces. The minimum energy on the crossing seam, or minimum energy crossing point (MECP) is where the crossover most likely takes place. [123] Therefore an optimizer that can consistently find the MECP would be beneficial for investigation of such spin crossover events.

An MECP is similar to a transition state (TS) structure on a potential energy surface (PES) in that they are both minimum within all degrees of freedom except one. A TS structure is the maximum on the one degree of freedom, thus a first-order saddle point, while an MECP is generally not a stationary point on the one degree of freedom. For MECP, this degree of freedom is defined by the constraint that the energies of the two states are the same. MECP and TS are also similar because they both act as a reaction barrier. TS is the energy barrier of a reaction route connecting two structures with bond changes. Likewise, MECP is the energy barrier of a route that connects spin changes. Therefore, when the two kinds of route coexist around a minimum, the reacting system will favor the exit channel with the lower energy barrier. [124] That barrier, in the case of an MECP, is often the bottleneck along the pathway of a spin-forbidden process, [125] where the system hop from one surface to the other, facilitated by spin-orbit coupling.

To gain quantitative knowledge of the process such as the hopping probability and the reaction rate, one needs to first locate the MECP on the crossing seam of two adiabatic surfaces. [124, 126] However, this can not be easily done by regular geometry optimization technique because MECP is not a stationary point on the PES. In terms of an optimization problem, MECP is obtained by optimizing the structure under the constraint that the energies of the two states are equal.

Several MECP optimization methods have been developed over the past 30 years. They

generally fall into three categories. Lagrangian methods, penalty fucntion methods and gradient projection methods.

Lagrangian methods. Morokuma group first applied the Lagrange-Newton method that uses Lagrangian multiplier to solve the constrained optimization problem. [127,128] These methods first construct a Lagrangian as a function of atomic coordinates and a multiplier λ:

$$L(\mathbf{q}, \lambda) = E_1(\mathbf{q}) + \lambda(E_2(\mathbf{q}) - E_1(\mathbf{q})) \tag{4.1}$$

where E_1 and E_2 are the energies of the two spin states. Then the constrained optimization problem is reduced to finding the minimum on the Lagrangian function without any constraints, and can be solved by Newton method. This Lagrange-Newton method is robust and often converges quickly thanks to the well-behaved Newton optimization method. However, the calculation of second derivatives of the Lagrangian which is required by Newton method is both expensive and non-trivial to implement. Moreover, regular Hessian updating methods such as Broyden-Fletcher-Goldfarb-Shanno (BFGS), [129] which are used to avoid calculating second derivatives explicitly, are not suited for Lagrange method [130].

Penalty function method, proposed by Ciminelli [131], adds an additional term to energy function as the energy equality constraint. The modified energy has the following form:

$$E'(\mathbf{q}) = \frac{E_1 + E_2}{2} + c_1 c_2^2 \ln[1 + (\frac{E_2 - E_1}{c_2})^2]. \tag{4.2}$$

The first term is the energy average, which is responsible of finding the minimum while on the seam. The second term is a function of energy difference, namely the penalty function, which is responsible of getting to the seam. The constant c_1 is the weight that we give to the penalty term and the constant c_2 determines how quickly we want the optimization to get to the seam. This method has the advantage of simplicity as it is relatively easy to implement in most optimization programs. The implementation is simply replacing the energy with the modified energy, and the gradient with the gradient of the modified energy. However, penalty function method suffers from poor convergence. [130]

Gradient projection method, first proposed by Bearpark et al. [132] and then adopted by Harvey et al. [133], projects the gradient of either spin state onto the intersection space, and then adds the gradient of the energy difference to it. Define $\mathbf{x_1}$ as the vector difference of the two gradients, i.e.

$$\mathbf{x_1} = \frac{\partial(E_2 - E_1)}{\partial \mathbf{q}} = \mathbf{g_2} - \mathbf{g_1}. \tag{4.3}$$

where $\mathbf{g}_1$ and $\mathbf{g}_2$ are the gradients of the two spin states respectively. The projector can be written as

$$P = I - \frac{\mathbf{x_1} \cdot \mathbf{x_1}^t}{|\mathbf{x_1}|^2}, \tag{4.4}$$

where I is identity matrix with the same dimensionality as $\mathbf{x_1} \cdot \mathbf{x_1}^t$. The modified gradient has the following form:

$$g' = P \cdot \mathbf{g_1} + 2(E_2 - E_1)\mathbf{x_1}. \tag{4.5}$$

The first term is the projected gradient in the intersection space, responsible of finding the minimum on the seam. The second term is the gradient of squared energy difference, responsible of driving the optimizer to the seam. This looks similar to penalty function method, yet it is better in the sense that the two parts of the gradient are decoupled, resulting in smaller chance of oscillation and quicker convergence in optimization calculations. [130] The disadvantage of this method is that the modified gradient is not a gradient of any proper energy function, which means optimization accelerating techniques that use energy as an indicator can not be directly applied, such as line search [134] and GEDIIS [135] (energy-represented DIIS geometry optimization). In addition, Hessian updating techniques that uses information from previous steps also behave poorly if the optimization does not start near the seam. [136]

In this work, we focus on the gradient projection method and its remedies. We incorporate advanced optimization techniques to accelerate the optimization, such as GDIIS (DIIS geometry optimization). [137] We show that if applied correctly, modern geometry optimization schemes significantly accelerates the MECP optimization.

4.2 Computational Methods

Theoretical background of geometry optimization has been previously described in Chapter 1.2. In the gradient projection method, a pseudo-gradient is constructed by Eq. 4.5 and used by the optimizer instead of the gradients of individual spin states. There are a number of established techniques that can be used to accelerate a geometry optimization. We will discuss GDIIS [137] and GEDIIS [135].

The GDIIS method is based on the idea of Direct Inversion in the Iterative Subspace [138] (DIIS) in SCF calculations where the Fock matrix at each step is a linear interpolation of those at previous steps. In GDIIS, the Newton-Raphson step is not taken from the last geometry but a linear interpolation (extrapolation) of the previously visited geometries on the PES. The interpolation coefficients are chosen in a way that minimize the length of a predefined error vector.

$$\mathbf{q}_\mathbf{n}^* = \sum_i^n c_i \mathbf{q}_\mathbf{i}, \sum_i^n c_i = 1 \tag{4.6}$$

where the error vector is given by

$$\mathrm{ErrF}(\mathbf{c}) = \| \sum_i^n c_i \mathbf{e}_\mathbf{i} \| \tag{4.7}$$

Minimization of the error function subject to the normalization constraint is solved by the Lagrangian method. With λ being the Lagrangian multiplier, the Lagrangian equation is given by

$$\begin{pmatrix} a_{11} & a_{12} & \cdots & a_{1n} & -1 \\ a_{21} & a_{22} & \cdots & a_{2n} & -1 \\ \vdots & \vdots & \ddots & \vdots & \vdots \\ a_{n1} & a_{n2} & \cdots & a_{nn} & -1 \\ -1 & -1 & -1 & -1 & 0 \end{pmatrix} \begin{pmatrix} c_1 \\ c_2 \\ \vdots \\ c_n \\ -\lambda \end{pmatrix} = \begin{pmatrix} 0 \\ 0 \\ \vdots \\ 0 \\ -1 \end{pmatrix} \tag{4.8}$$

where a_{ij} = trace($\mathbf{e_i}.\mathbf{e_j}$). Rewrite Eq. 4.8 into

$$\mathbf{Ac} = \mathbf{b} \tag{4.9}$$

and the coefficients can be solved by directly invert the A matrix,

$$\mathbf{c} = \mathbf{A}^{-1}\mathbf{b} \tag{4.10}$$

Matrix A has the errors from the previous n iterations, hence the name "direct inversion in the iterative subspace".

The error vector is chosen to represent how close the geometry is to convergence. Therefore either geometry or gradient can be chosen, represented by $\mathbf{H}_n^{-1}\mathbf{g}_i$ and $\mathbf{g}_i$ respectively. It has been shown that using the gradient results in better convergence in most cases [139].

DIIS significantly accelerates the convergence of SCF calculations. Likewise, GDIIS also significantly accelerates the convergence of geometry optimizations in most cases. However, the target function in a geometry optimization is complex and often contains many minima, saddle points and flat areas. These characteristics cause GDIIS to behave undesirably. For example, when a GDIIS optimizer pass through a flat area, the gradients will be small for several steps, causing the interpolated gradient to also be small. When the optimizer approaches a minimum, the gradient will suddenly become larger. Subsequently, the structure will be pulled back to the flat area where the gradient is small, thus delaying the convergence. [16]

Later GEDIIS was proposed to fix this problem. It uses an energy indicator as the error vector instead of gradient or geometry indicators. This technique was based on the SCF-EDIIS [140] proposed by Scuseria and coworkers. The relationship between GEDIIS and SCF-EDIIS is an analog to the relationship between GDIIS and DIIS; the former is the extension of the latter in geometry optimization.

In GEDIIS, the energy function is the error indicator. It is approximated to first order with respect to geometry $\mathbf{q}$.

$$E(\mathbf{q}^*) = E(\mathbf{q}_i) + (\mathbf{q}^* - \mathbf{q_i})\mathbf{g_i} \tag{4.11}$$

where $\mathbf{g}_i$ is the gradient of the i-th geometry. Applying eq. 4.6 and interpolate the right hand side of eq. 4.11 over n points with the same set of coefficients, we get

$$E(\mathbf{q}^*) = \sum_i^n c_i E(\mathbf{q}_i) - \frac{1}{2}\sum_{i,j}^n c_i c_j (\mathbf{g}_i - \mathbf{g}_j)(\mathbf{q}_i \mathbf{q}_j) \tag{4.12}$$

The energy is then minimized directly with respect to the coefficients c_i's.

The MECP optimization was implemented in a local Gaussian Development Version. The method was implemented as a regular optimization job. At each iteration before the Newton-Raphson step, two separate gradient calculations are run for both states, and the two gradients are then combined as eq. 4.5 to construct the effective gradient. The effective gradient is regarded as the gradient in a regular geometry optimization by the optimizer which then carries out the optimization as usual. Different optimization techniques built in Gaussian, including rational function optimization [141, 142] (RFO), GDIIS, GEDIIS, etc. can be employed since they are decoupled

from the gradient calculation. Compared to previous method, this implementation makes a variety of optimization techniques ready to use, which have proved to accelerate geometry optimization significantly.

In order to test the effectiveness of our implementation, we incorporate it with GDIIS and GEDIIS respectively, and compare them with a popular implementation by Harvey [133]. In this work, geometry optimization is considered converged with the following criteria: root mean square (RMS) force is less than 5.0×10^{-4} au, maximum component of force is less than 7.5×10^{-4} au, RMS geometry displacement is less than 2.0×10^{-3} au, maximum component of geometry displacement is less than 3.0×10^{-3} au, and energy difference is less than 4.0×10^{-5} au. This was applied to both Harvey's method and our implementation. No symmetry factor is considered.

4.3 Results & Discussion

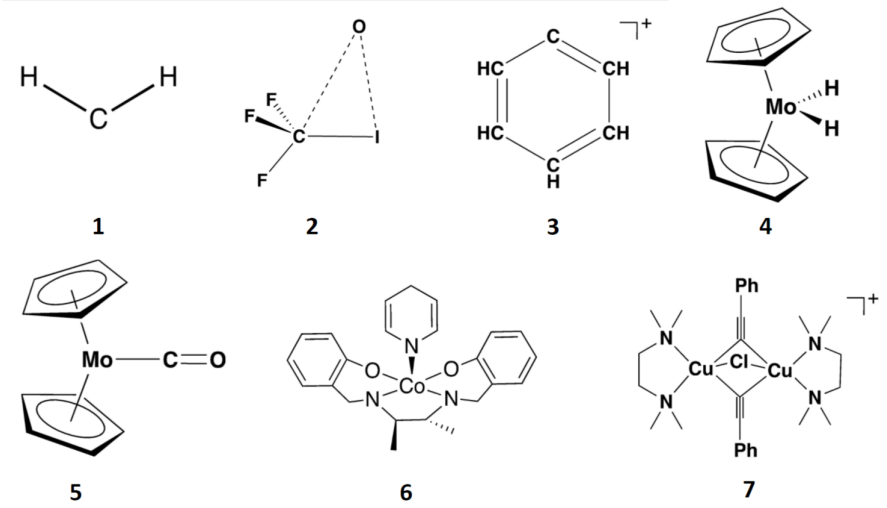

Figure 4.1: Seven benchmarking molecules for MECP-locating methods

7 molecules were chosen in our method benchmark (Figure 4.3, ranging from small to medium-sized, and from organic molecules to transition metal complexes. These molecules all exhibit typical intersystem crossing behavior experimentally. [133, 143–145] In addition, species 1, 3, 4 have a second "distorted" version of geometry as a different starting point for the optimization. These geometries deviate from the standard VSEPR structure and were added to test the robustness of our implementation.

We compare the gradient projection method that was implemented by Harvey [133] (hereinafter referred to as the GP method) with our implementation incorporating GEDIIS and GDIIS respectively (hereinafter referred to as GEDIIS and GDIIS respectively). We applied these methods to locate the MECPs of the 7 molecules where intersystem crossing most likely takes place, and compared the results and the convergence behavior of different methods. The converged geometries are included in Appendix A.

Table 4.1: The number of steps it took to converge to the MECP of each species using different methods. The average number of converging steps of the GP method is calculated by assuming that species 6 and 7 each takes 100 steps to converge

		# of steps to converge		
Species	Size	GP	GEDIIS	GDIIS
1	3	7	10	6
1'	3	9	17	10
2	6	19	25	28
3	11	14	8	7
3'	11	26	17	13
4	23	39	36	29
4'	23	26	46	44
5	23	40	61	55
6	52	100+	25	23
7	53	100+	39	41
Mean w/o 6, 7		**22.5**	**27.5**	**24**
Mean		**38.0**	**28.4**	**25.6**

Table 4.1 shows The number of steps it took to converge to the MECP of each species using different methods. The converging criteria are described in the Method section.

Overall, GEDIIS and GDIIS took 30 - 40% less steps to converge than the GP method. For the two bigger species 6 and 7, the GP method failed to converge within 100 steps while both GEDIIS and GDIIS converged within 50. GEDIIS and GDIIS behaved similarly overall, with GDIIS slightly better on average than GEDIIS. More specifically, GDIIS almost always converged slightly faster than GEDIIS except species 2 and 7. If we only look at the smaller species of the test set (excluding 6 and 7), the three methods performed similarly and the GP method has a slight advantage. This indicates that these advanced geometry optimization schemes have a overhead that can only be compensated by the accelerating effect gained on systems with more than 30 atoms.

In addition to the accelerating effect, GEDIIS and GDIIS are able to make MECP geometry optimization more robust, as the results for species 6 and 7 showed. This is expected because GEDIIS and GDIIS are proven [135, 137] to make optimizations faster and more robust. However, these effects do not have a significant effect on small-sized systems which only take a few steps to converge; it's not enough steps to see the effect of extrapolation methods. Between the two optimization schemes, surprisingly, the older method GDIIS almost always used less steps to converge than GEDIIS. This is because that in addition to geometry indicators, GEDIIS also uses energy as the error function in the DIIS process, whereas energy is ill-defined in a projection framework. For example, in our calculation, total energy is defined as $(E_{HS} - E_{LS})^2$, which is not the real energy of the system.

Both GDIIS and GEDIIS performed badly on species 4' and 5, which only have 23 atoms respectively, but took the two methods around 50 steps to converge. To identify potential systematic failure in these runs, some important optimization indicators were plotted against step number during the optimization (Figure 4.2, 4.3), including high spin state (HS) energy, squared energy difference, RMS force, and the angle difference of $\mathbf{x_1}$ (defined in Eq.4.3) between structures before

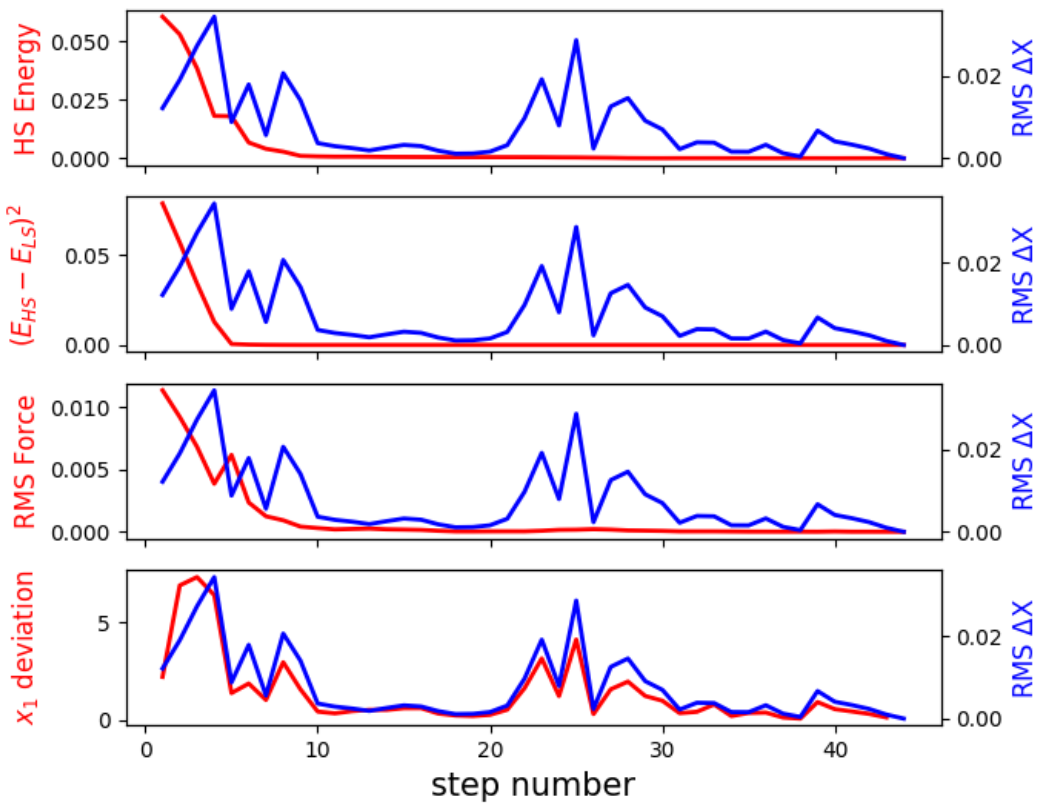

Figure 4.2: Optimization profile for species 4'. HS means high spin. HS energy is relative to the MECP energy, and is in hartree. RMS Force and RMS ΔX are both in atomic units. x_1 deviation is in degrees.

and after every step. RMS atomic displacement (ΔX) were also shown in each graph as a reference. For both species, E_{HS}, $(E_{HS} - E_{LS})^2$ and RMS force (the first three rows of each graph) all converged or were close to converging within 20 steps, where RMS ΔX (atomic displacement) had an abnormal rise. Compared to similar graphs for the other species that converged quickly with GDIIS and GEDIIS (not shown here), the abnormal rise of RMS ΔX after RMS force converged is unique. This indicates that the optimizer can be unstable when on or close to the seam. To investigate the optimizer's behavior near the seam, we computed the direction of $\mathbf{x_1}$ (branching vector, defined by eq. 4.3) at every step, and calculated the deviation of it from the last step. Figure 4.2, 4.3 show that it has a very similar trend with RMS ΔX, especially at the abnormal rise. This means that the size of the step the optimizer took along the branching vector is proportional to the total step size even when the system is close to the seam. This is unexpected because the optimizer is supposed to move in parallel with the seam when near it, which would have much smaller changes in x_1 angle. This

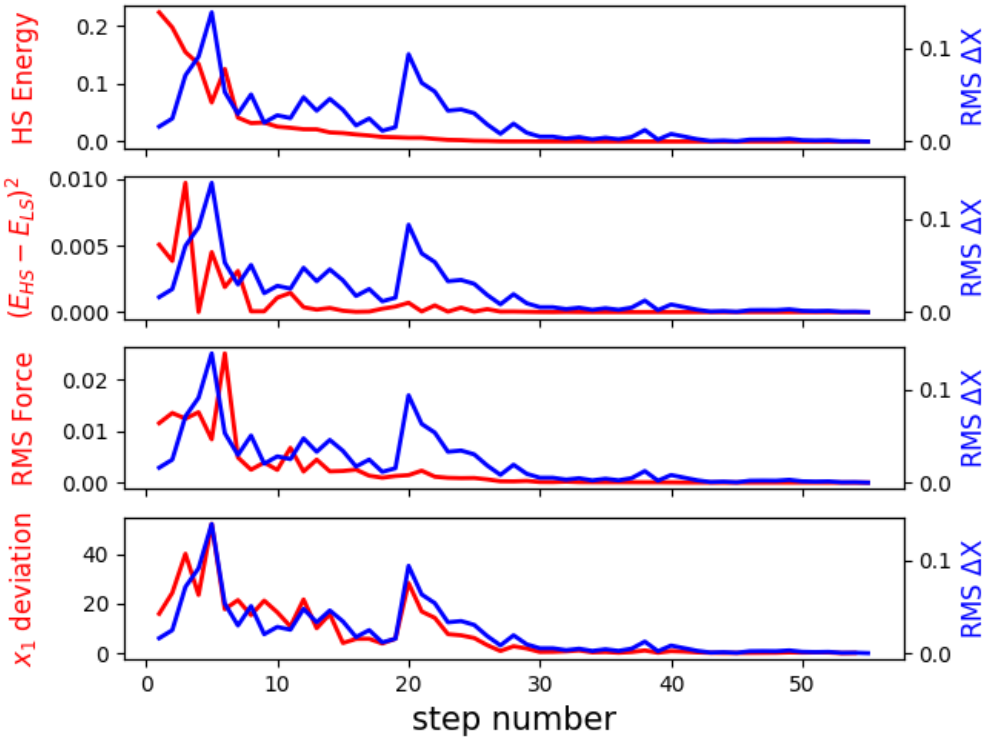

Figure 4.3: Optimization profile for species 5. HS means high spin. HS energy is relative to the MECP energy, and is in hartree. RMS Force and RMS ΔX are both in atomic units. x_1 deviation is in degrees.

behavior caused the optimizer to travel away from the seam, thus taking extra steps to converge. Although our implementation showed accelerating effect and more robustness on large systems, we are still working on solving this issue, hoping to achieve an improvement across systems of all sizes.

4.4 Conclusion

This work is an efficient implementation of the gradient projection method used to find the MECP of two spin states. MECP is the energy barrier of an intersystem crossing event, thus provides valuable information for thermodynamics and kinetics study on such spin change events.

Our implementation is developed in the Gaussian software framework, thus readily incorporated with a variety of geometry optimization techniques, such as GDIIS and GEDIIS. A benchmark study was carried out that compared Harvey's implementation and our implementation incorporated with GDIIS and GEDIIS. Results showed that with a small overhead, our implementation with GDIIS and GEDIIS are both more robust and converges 30 - 40% quicker than Harvey's imple-

mentation. In particular, GDIIS is almost always slightly faster than the newer technique GEDIIS. Finally, for cases where our method performed worse than Harvey's method, a common issue has been identified that the optimizer sometimes fails to stay near the seam when it gets close to convergence, which caused the optimization to take extra steps. This is being investigated and results will be published in future articles.

Chapter 5

Modeling Metal Oxide Photodetachment Spectroscopy with State-of-the-Art Methods: ZrO_2 + H_2O Adduct

5.1 Introduction

Zirconium oxide (ZrO_2) is an important material with extensive applications in catalysis, photochemistry, refractory ceramics and corrosion resistant materials [146–149]. Similar to its neighbor in the periodic table, titanium, ZrO_2 has also shown photocatalytic capability for water splitting to generate H_2 and O_2 [150–152]. The pursue of an efficient water splitting catalyst has been decades long, but has only received limited success [153, 154], regardless of whether it is TiO_2 based or ZrO_2 based. This is mainly due to a lack of detailed mechanistic understanding necessary for rational design of metal oxide catalysts [153].

Studies on transition metal oxide catalysts has shown that surface defects are often the active sites in a catalytic reaction [155–157]. Therefore studying the interaction between defect sites and water molecules is the key to understanding the mechanism of water splitting. However, it is experimentally difficult to study defects on surfaces because they are difficult to prepare reliably. Instead, metal oxide clusters containing one to a few metal centers have shown to be useful model systems for mechanistic studies on metal oxide surfaces. These species are relatively easy to prepare, and have certain structural motifs that mimic common defects on metal oxide surfaces [158–162]. In addition, these species are easier for computational methods to model since they contain less atoms. Therefore, computational studies in this area are often important additions to experimental work since they can provide valuable mechanistic insight with a relatively low computational cost.

Studies on the interaction between TiO_2 cluster and water are abundant [153, 163, 164]. Fewer studies have been done for the interaction between ZrO_2 cluster and water. Experimentally, Holms and coworkers [165] did IR studies of water sorption on ZrO_2 polymorphs. High frequency bands at 3760 cm^{-1} and 3660 cm^{-1} were discovered and assigned to chemisorbed OH groups, indicating a $OZr(OH)_2$ structure. Computational studies on ZrO_2 and H_2O has been carried out most comprehensively by Dixon and coworkers [166], who used DFT and CCSD(T) to study the hydrolysis

reactions of $(ZrO_2)n$ ($n = 1 - 4$). For the simplest stoichiometric ZrO_2/H_2O reaction, $ZrO_2 + H_2O$, they found that the cis- di-hydroxyl $OZr(OH)_2$ structure, in which the water is split, has around 50 kcal/mol lower energy than the molecularly absorbed ($ZrO_2 \cdot H_2O$) structure, which agrees with Holms' results. They also found that the singlet is around 50 kcal/mol lower in energy than the triplet. More electronic structural details remain to be discovered.

Slow electron velocity-map imaging of cryogenically cooled anions (cryo-SEVI) is a high-resolution spectroscopy technique that provides vibronically resolved detachment spectrum for anion and neutral species. The Neumark group has used cryo-SEVI to characterize the TiO_2^- monomer [167] and $TiO_3H_2^-$ [164] (a single TiO_2^- reacted with a single H_2O). Here, they used cryo-SEVI to probe the $ZrO_3H_2^-$ species. The resulting spectrum show rich vibronic structures in close range with each other (~ 50 cm^{-1}), with a high resolution. My role in this study is primarily interpreting the experimental spectrum using a Franck-Condon simulation, assigning vibronic structures to individual excitations and gain mechanistic insight into the catalytic capability of zirconium oxide on water splitting reactions.

5.2 Computational methods

Franck-Condon calculations were used to simulate the experimental spectrum. These simulations calculate the dipole strength of possible transitions between the initial and the final states of an electron detachment process, at vibrational level. These calculations are based on the Franck-Condon principle. In quantum mechanics, the probability of an electronic transition occurring is given by

$$P_{i\to f} = |\langle\psi^*_{\text{final}}|\hat{\mu}|\psi^*_{\text{initial}}\rangle|^2 \tag{5.1}$$

where $\hat{\mu}$ is the transition operator, and is only dependent on the electronic component of the wave function. Thus, separating the electronic and nuclear wave function according to the BO approximation, we have

$$\langle\psi^*_{\text{final}}|\hat{\mu}|\psi^*_{\text{initial}}\rangle = \langle\psi^*_{\text{nu, f}}|\langle\psi^*_{\text{el, f}}|\hat{\mu}|\psi_{\text{el, i}}\rangle\psi_{\text{nu, i}}\rangle = \langle\psi^*_{\text{nu, f}}|\psi_{\text{nu, i}}\rangle\langle\psi^*_{\text{el, f}}|\hat{\mu}|\psi_{\text{el, i}}\rangle \tag{5.2}$$

where $\langle\psi^*_{\text{nu, f}}|\psi_{\text{nu, i}}\rangle$ is the nuclear wave function overlap, also termed the Franck-Condon factor. The transition probability is proportional to this factor. In other words, when an electronic transition happens, it is so fast that the nuclear positions remain stationary where the nuclear wave function reaches the maximum overlap. This is also termed a vertical excitation.

Our initial Franck-Condon calculations were carried out with Gaussian Development Version, Revision I.10+ [86]. The method used in the software is implemented by Bloino, Barone and coworkers [168, 169]. It assumes all normal modes to be harmonic oscillators, and calculates the wave function for each normal mode for both initial and final states. It then calculates the overlap between each vibrational level in the initial state and each in the final state, and produces the relative intensity in the simulated spectrum. The excitation energies are the corresponding horizontal coordinates in the spectrum.

However, as we show later, this method failed to reproduce a considerable number of peaks in the experimental spectrum, largely due to one of the normal modes of $ZrO_2 + H_2O$ adduct being an umbrella mode, far away from the harmonic oscillator approximation. Therefore we carried out

additional normal mode analysis using Discrete Variable Representation (DVR) technique described in Miller's paper [170]. DVR is a numerical method using grid point basis functions (in our case particle in a box wave functions) to represent the Hamiltonian for selected normal modes. The benefit of DVR is that it only requires single point potential energies on the grid points and can achieve high accuracy in simulating anharmonic potentials, given a fine grid.

We calculate the hamiltonian of a state with DVR in the following steps. First, we choose a finite basis as grid points for DVR. Second, we derive a grid point representation of kinetic energy. Third, we do an energy scan over all grid points for potential energies and construct the Hamiltonian. Here, we chose the particle-in-a-box eigenfunctions as the basis. On a 1D grid, it can be shown that if we apply DVR on the interval $(-\infty, \infty)$, the kinetic energy is given by

$$T_{ii'} = \frac{\hbar}{2m\Delta x^2}(-1)^{i-i'} \begin{cases} \frac{\pi}{3}, & i = i' \\ \frac{2}{(i-i')^2}, & i \neq i' \end{cases} \tag{5.3}$$

where Δx is the grid spacing, i and i' are two grid points, i.e. two subscripts of the Hamiltonian. On a 2D grid, the Hamiltonian matrix is

$$H_{ij,i'j'} = T_{ii'}\delta_{jj'} + T_{jj'}\delta_{ii'} + \delta_{ii'}\delta_{jj'}V(x_i, y_i) \tag{5.4}$$

where x_i and y_i is the ith grid point on the two dimensions respectively. The benefit of DVR is that it allows arbitrary accuracy towards the limit allowed by the model chemistry, on vibrational energy levels. This makes it a good candidate method to analyze normal modes with large anharmonicity, like the umbrella mode in this study. The DVR simulations carried out in this study used a grid spacing of 0.03 Å. It can be shown that finer grid spacing does not change the simulation results significantly.

Preliminary results suggest meaningful differences in normal mode frequencies and vertical excitation energies between model chemistries. Therefore, three DFT-based methods ωB97XD [171], B3LYP [172–175] and B3PW91 [176] and three basis sets def2tzvp [177], Stuttgart/Cologne [178] ECP28MHF (SC) and SDDPlusTZ + ECP (SDD+TZ) [179–181] are used in initial benchmark calculations, resulting in a total number of 9 model chemistries. Different model chemistry indeed produced meaningfully different results. On the other hand, care was taken to determine scaling factors for the calculated frequencies of the neutral state, so that the simulated FC spectrum aligned the best with experimental ones. This step is necessary because calculated values of frequencies are very sensitive to DFT errors, especially for those that have a small magnitude. If the scaling factor is not too far from 1, and that the peak positions align well with the experimental spectrum after scaling, the scaling can be regarded as an effective way to compensate DFT error. Likewise, all simulated FC spectra were also shifted such that the vertical excitation energy agrees with the experimental one, making the two spectra origins overlap. Because of the scaling and shifting, differences between model chemistries are less meaningful. Therefore, we will only show results produced with ωB97XD and the SC basis set.

All calculations were carried out with Gaussian Development Version, Revision I.10+ [86]. Stability was tested on all converged Kohn-Sham wave functions. Standard geometry optimization methods [182] were used to get minimum geometries.

5.3 Experimental Details

The cryo-SEVI technique and apparatus have been described elsewhere in detail [183–185]. To summarize here, a packet of mass-selected anions A^- is intersected with a laser beam that has a pre-selected energy. If that energy exceeds the electron bonding energy to the anion, the photon may detach an electron. The remaining energy can become the kinetic energy or excite the resulting neutral species into its vibronic excited states. The energy from the photon must be conserved, therefore the distribution of kinetic energies among the detached photoelectrons indicates the vibronic structure of the neutral species.

The spectrum produced by the cryo-SEVI experiments are shown in Figure 5.1.

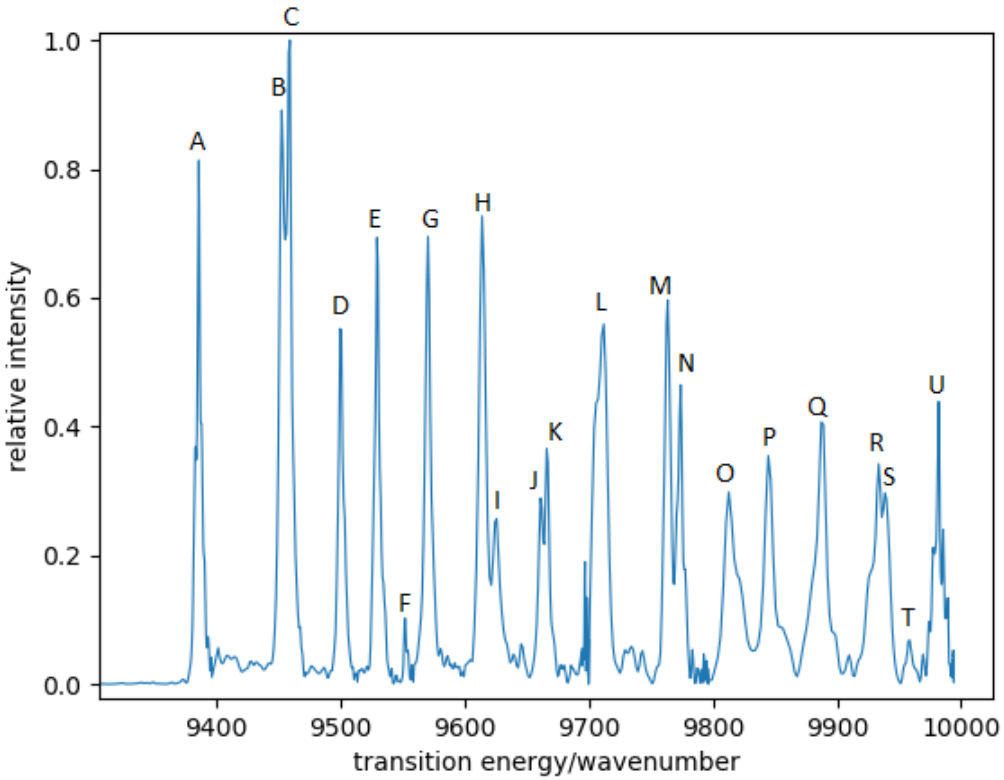

Figure 5.1: Cryo-SEVI spectrum of anionic ZrO_2 and H_2O adduct losing one electron

The spectrum spans 9350 - 10000 cm^{-1} and shows rich vibronic structures in close proximity with each other ($\sim$ 50 cm^{-1}), with a high resolution. The first sharp peak, the 0 to 0 transition, gives an electron affility of 1.16 eV.

5.4 Results and Discussion

In this section, we present the results of Franck-Condon simulations, and try to interpret the experimental spectrum by assigning each peak to a certain vibronic excited state. Finally, we draw a conclusion about what species are formed in the ZrO_2 and H_2O adduct.

5.4.1 Harmonic Oscillator Approximation

Previous study [166] revealed the most stable geometry of $ZrO_2 \cdot H_2O$ is the chemically absorbed cis-OH $OZr(OH)_2$ structure (See Figure 5.2). It has an umbrella-like shape, with Zr outside the O-O-O plane. We hypothesized that this was the only species that was probed in the experiment since it was an ultra-cold experiment.

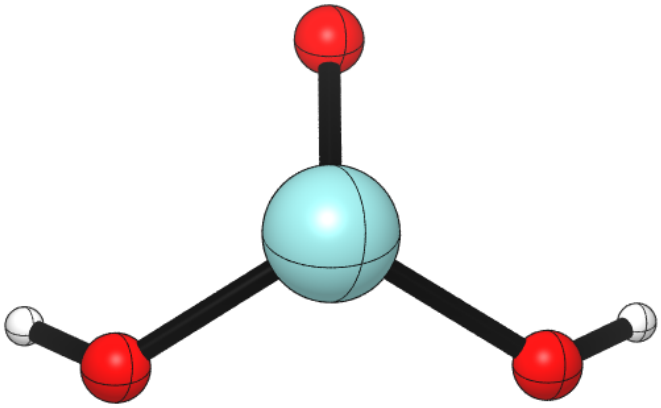

Figure 5.2: The cis-OH $OZr(OH)_2$ structure of $ZrO_2 \cdot H_2O$. It has an umbrella-like shape, with Zr outsidethe O-O-O plane. It is the most stable geometry of ZrO_2 and H_2O adduct reported by Dixon.

A frequency calculation and a normal mode analysis was done on this geometry using ωB97XD and the SC basis set. Table 5.1 shows the normal modes and their corresponding frequencies. Of particular interest here is mode **a1** which has an umbrella-like motion with a double well potential.

Table 5.1: Normal mode analysis of $OZr(OH)_2$. Frequencies are in cm^{-1}. Calculated in Gaussian with ωB97XD and the SC basis set.

normal mode	mode frequency
a1	91.51
a2	170.57
a3	210.63
a4	427.78
a5	439.07
a6	492.31
a7	513.69
a8	624.39
a9	648.97
a10	949.75
a11	3971.86
a12	3974.14

Figure 5.3 shows the cryo-SEVI spectrum overlaid with sticks generated by a Franck-Condon simulation using Gaussian Development Version Revision 10+ with the same model chemistry as in Table 5.1. The blue line is the experimental spectrum and the black sticks represent simulated FC progressions calculated by Gaussian. The simulated peaks are annotated with their vibronic states. Excited states of the anionic $OZr(OH)_2$ are not considered since they are not populated in the ultra-cold cryo-SEVI experiments.

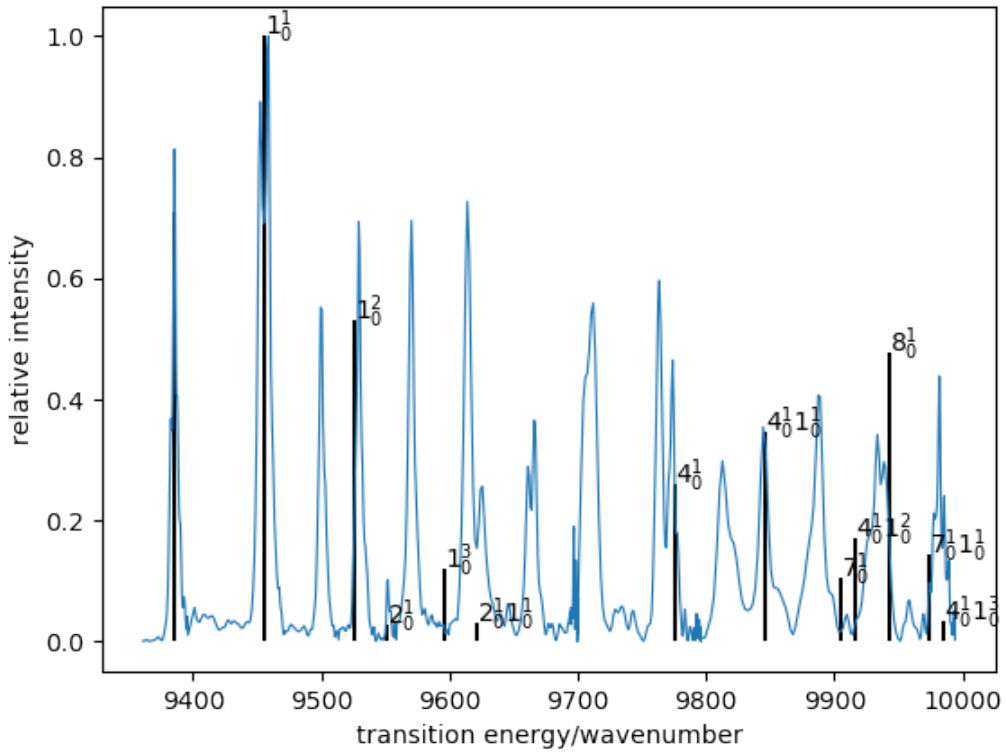

Figure 5.3: The cryo-SEVI spectrum overlaid with sticks generated by a Franck-Condon simulation using Gaussian. The blue line is the experimental spectrum and the black sticks are the peaks and the corresponding relative intensities calculated by Gaussian. The simulated peaks are annotated with their vibrational states. The notation 1_0^1 means the peak is produced by exciting an electron from the vibrational ground state of anionic $OZr(OH)_2$ to the neutral $OZr(OH)_2$ with mode **a1** excited to the first excited state. $1_0^1 2_0^1$ denotes a combination mode of **a1** and **a2**, both at the first excited state.

The calculated vertical excitation energy was shifted horizontally and **a1**, **a2**, **a4** were scaled to achieve optimal alignment with the experimental spectrum. Their original and changed values are shown in Table 5.2.

Table 5.2: Details of the scaling and the shift operations.

item	original/cm^{-1}	changed/cm^{-1}
vertical excitation	9910.2	9385.5
a1	91.5	70.0
a2	170.6	166.0
a4	427.8	390.0

For **a1**, the first and the second excited states match the experimental spectrum well, but 1_0^3 does not match any peaks in the spectrum. We attribute this to the high anharmonicity of **a1**. For **a2**, calculated intensities are quite low (including the combination modes with **a1**) and match poorly with the spectrum. In addition, many peaks in the spectrum are not found from the simulated results in the 9500 - 9750 cm^{-1} region. Therefore, we need to take anharmonicity into account.

In order to simulate a double-well potential, we tried the potential of the following form:

$$V(X) = \lambda x^4 - kx^2$$

but it did not produce a better FC simulation than the harmonic approximation. The results are omitted here.

5.4.2 Anharmonic Treatment with DVR

Discrete Variable Representation (DVR), a numerical method using grid point basis functions (in our case particle in a box wave functions) to represent the Hamiltonian for selected normal modes, was then employed. The benefit of DVR is that it only requires single point potential energies on the grid points and can achieve high accuracy in simulating anharmonic potentials, given a fine grid. The results are shown in Figure 5.4 in red sticks. Clearly, the anharmonicity is reproduced. Moreover, every simulated stick consists of two predicted peaks of the same energy, which successfully simulated the doublet behavior of a double-well mode.

One complication involved in a DVR calculation is that we cannot obtain force constants from DVR calculations since they are numerical methods. Therefore, there is no obvious way to scale the frequencies. We tried to achieve the scaling effect by directly scaling all the scanned potential energies. The results are shown in Figure 5.4. The simulated peaks were indeed scaled, in an anharmonic way. That is, the peak shift increases as it gets to higher excitation level. It also appears that 90% scaled results match better than the original results.

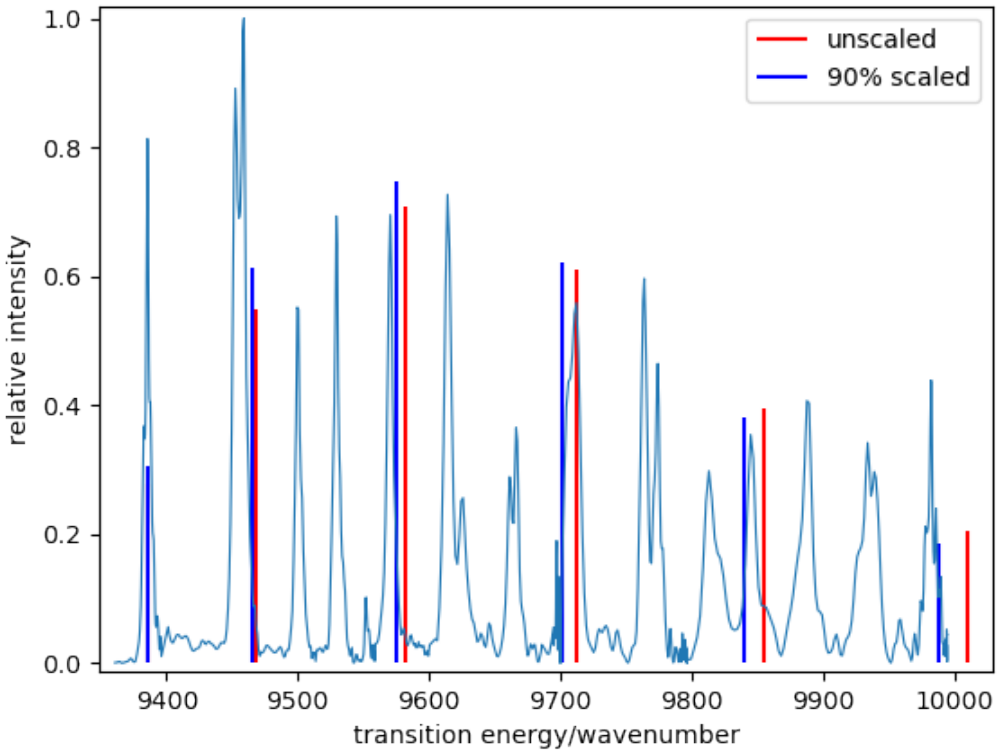

Figure 5.4: Cryo-SEVI spectrum of the electron detachment process of anionic ZrO_2 and H_2O adduct, overlaid with two series of DVR-simulated FC progressions, one unscaled, the other had its potential energies scaled to 90%.

Figure 5.5 show the result of the 90% scaled DVR-simulated FC progressions combined with the Gaussian-simulated results in Figure 5.3. All excitations that involve **a1** were removed from the Gaussian results. This combined simulated spectrum matches more than half of the peaks in the cryo-SEVI spectrum, but are still missing a few significant peaks.

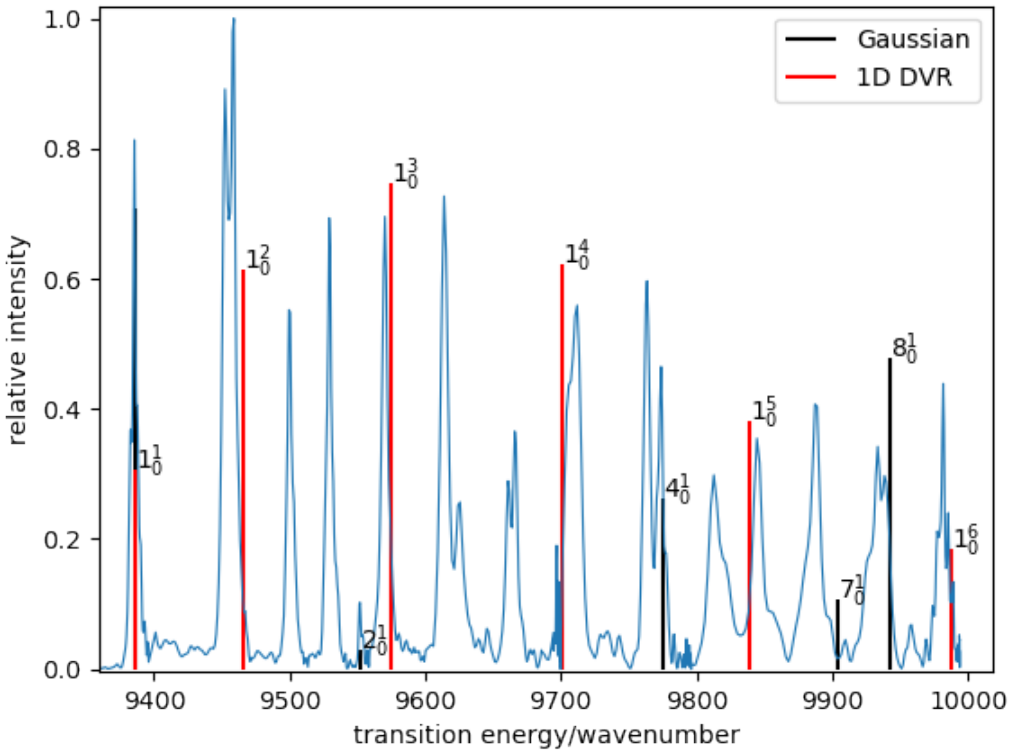

Figure 5.5: 1D-DVR analysis on mode **a1** combined with the Gaussian results with **a1** truncated, overlaid with the cryo-SEVI spectrum

Comparing to the pure Gaussian FC simulation, this combined graph does not take into consideration the combination modes of **a1** and **a2** because the lack of ways to incorporate a DVR calculation into Gaussian. A 2D DVR simulation on **a1** and **a2** would reproduce the combination modes. There are a few other facts that supports this direction of study. First, **a2** and **a1** have similar motions and they should couple fairly strongly. It is highly likely that **a1** & **a2** combination modes played an important role in the experimental spectrum. Second, it is shown that DVR simulations produce different relative intensities than the harmonic FC simulations from Gaussian. Doing a 2D DVR may change the relatively low intensities of **a2** related modes predicted by Gaussian. Third, both **a1** and **a2** are very soft modes which match the range where we failed to predict the most peaks. All other modes have too big frequencies to be considered candidates of the missing peaks in 9500 - 9700 cm^{-1}.

Figure 5.6 shows the 2D DVR result in comparison with the 1D one. Both 1D and 2D DVR scan energies are scaled to 90% of their original values. Most sticks are labeled with their corresponding vibronic transition. Clearly, 1D and 2D do not differ significantly in their **a1** transitions, so only the 1D ones are labeled. Note that the 1_0^6 transition simulated by 1D and 2D are separated

by ~ 20 cm^{-1}. In addition, 2D DVR calculation do not provide information on vibronational assignment of sticks that correspond to **a2** and **a1/a2** combination modes. The labels on those sticks were estimated based on their position, and in a way analogous to the **a1** progressions. **a2** and **a1/a2** signals are significantly weaker than **a1**'s which agrees with the Gaussian results. Most importantly, 2D DVR predicted four more peaks than 1D DVR in the 9750 - 9950 region, despite the intensity mismatch with the experimental spectrum.

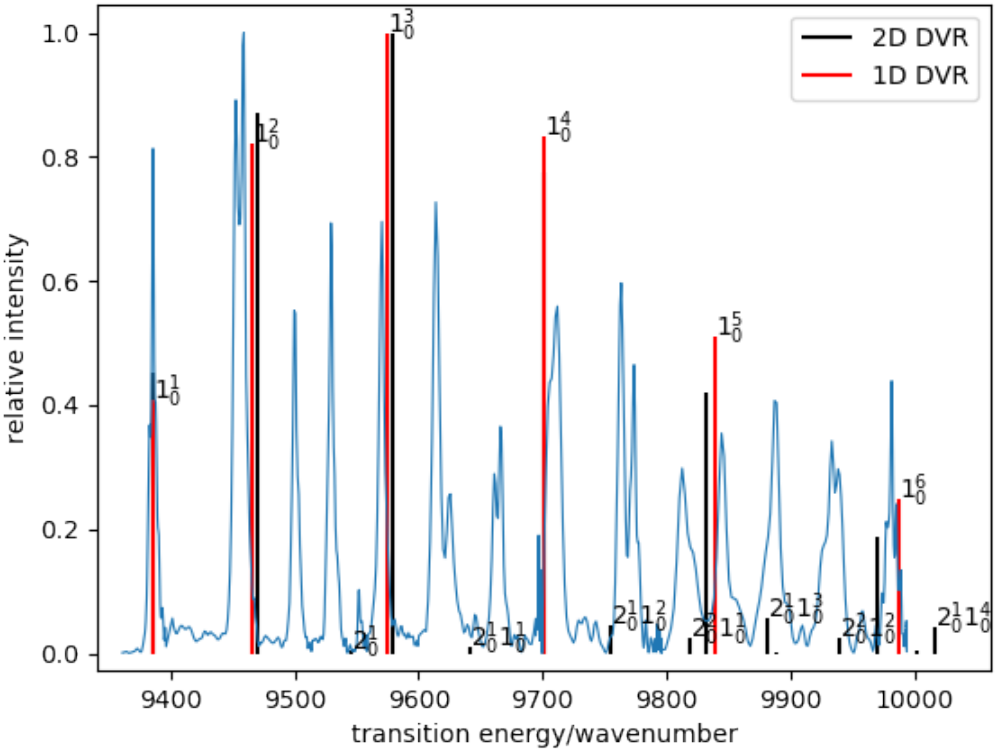

Figure 5.6: Cryo-SEVI spectrum of the electron detachment process of anionic ZrO_2 and H_2O adduct, overlaid with both 1D and 2D DVR-simulated FC progressions. The simulated sticks are labeled with their corresponding vibrational transitions.

Combining the results from 2D DVR and Gaussian, we summarize vibrational assignments in Table 5.3. The peak labels are those shown in Figure 5.1.

Table 5.3: Peak positions, shifts from the 0 to 0 transition and viborational assignments of features in the cryo-SEVI spectrum of ZrO_2 and H_2O adduct. Peak R and S could be either $2_0^2 1_0^2$ or 8_0^1 because the they are only a few cm^{-1} apart.

Peak	eBE (cm^{-1})	Shift (cm^{-1})	Assignment
A	9385.5	0	0_0^0
B	9452.4	66.9	1_0^1
C	9458.9	73.4	1_0^1
D	9500.4	114.9	unassigned
E	9529.2	143.7	unassigned
F	9551.5	166	2_0^1
G	9570.3	184.8	1_0^2
H	9613.8	228.3	unassigned
I	9625.6	240.1	unassigned
J	9661	275.5	unassigned
K	9666	280.5	unassigned
L	9712	326.5	1_0^3
M	9763.5	378	$2_0^1 1_0^2$
N	9773.8	388.3	4_0^1
O	9812.7	427.2	$2_0^2 1_0^1$
P	9844.5	459	1_0^4
Q	9889	503.5	$2_0^1 1_0^3$ or 7_0^1
R	9933.5	548	$2_0^2 1_0^2$ or 8_0^1
S	9939.8	554.3	$2_0^2 1_0^2$ or 8_0^1
T	9957.9	572.4	unassigned
U	9981.8	596.3	1_0^5

In summary, the umbrella motion **a1** is highly anharmonic and cannot be treated with a harmonic approximation. DVR was employed to simulate vibronic states of the double-well potential and produced an FC progression of increasing spacing. To further simulate the strong coupling between **a1** and **a2** and recover their combination modes, 2D DVR was employed and applied to both **a1** and **a2**. 2D DVR predicted four more peaks in the 9750 - 10000 cm^{-1} region. Despite the success of DVR, four peaks between 9500 and 9700 cm^{-1} are still unable to be simulated. Due to the fact that all other modes have too big frequencies to be considered candidates of the missing peaks in this range, we think there were other species that were probed in the cryo-SEVI experiment. However, to this end, we have not found a qualifying candidate. Species that we have considered include the lowest electronic excited state of the singlet neutral $OZr(OH)_2$ which lies 4.27 eV above the ground state, and the triplet neutral $OZr(OH)_2$ which lies 2.76 eV above the singlet.

Chapter 6

Summary & Outlooks

6.1 Summary

The goal of this work is to expand the computational toolkit for theoretical chemistry, with an emphasis on expanding knowledge on potential energy surfaces (PES) and transition metal chemistry.

A PES is a multi-dimensional hyper surface. Due to the high dimensionality, efficient computational tools are essential to study PESs. This thesis dedicated most work to developing computational tools around PES. These works include benchmarking a spin projection method to correct distorted PES due to spin contamination, a geometry optimization tool that locates the minimum energy crossing point of two adiabatic PESs of different spins, and a mechanism generator that connects two points on a PES with intermediates that constitute reaction paths with low energy barriers. In addition, a Franck-Condon (FC) simulator using 2D- discrete variable representation (DVR) was developed and used to interpret a cryo-SEVI spectra of ZrO_2 and H_2O adduct produced by our experimental collaborator.

A benchmark of Approximate Projection. Single-determinantal methods, such as conventional DFT, can introduce spin contamination error to approximate wave functions, which in turn distorts the resulting PES. This error is prominent in transition metal systems. We applied the Approximate Projection (AP) method and the corresponding first and second derivative algorithms, to calculate the magnetic exchange coupling constants (J-couplings) of 9 bi-metallic complexes and the spin crossover energy gaps of 43 mono-center transition metal complexes. AP reduced the mean average error (MAE) of the 43 energy gaps from 14.92 to 3.03 kcal/mol. Although slightly worse than Friesner's DBLOC method, AP does not introduce any fitting parameters for the test set and incurs minimal computational cost. On the other hand, AP was found to behave worse than a non-projection (NP) method for calculating J-couplings, due to the spin contamination errors being outweighed by errors from DFT functional. In addition, both J-coupling and spin crossover gap were found to be mostly unaffected by AP-corrected geometry optimization, although studies had shown that AP correction greatly altered the energy landscape of transition metal species.

MECP optimization. Minimum energy crossing point (MECP) is the minima on the crossing seam of two adiabatic PESs. In terms of intersystem crossing events, the two surfaces are those of two spin states. An optimization tool was developed that locates the MECP geometry given two

spin states using a projected gradient method. The tool also incorporated efficient geometry optimization techniques such as GDIIS and GEDIIS, which accelerates the optimization process by 30 - 40%, and makes MECP optimizations more robust, compared to Harvey's implementation. Despite the significant acceleration, in some cases the optimization tool behaves worse than Harvey's. A common issue has been identified in the tool that the optimizer sometimes goes off the seam near convergence, causing delays in optimization. This will be addressed in future work.

Mechanism generator. Chemical intuition is not always reliable when trying to elucidate the most complex and counter-intuitive reaction mechanisms. Various tools have been developed to help chemists systematically searches the PES for the lowest energy pathway between two points, but there is still room for improvement. Computational cost and human intervention are two main factors one has to consider when designing a tool. In general, more human intervention means less computational cost, but also means less systematic and an increased chance to miss important possible paths. Herein, a systematic approach is proposed to generate reaction mechanisms based on an electron-pushing model, and is implemented. Given reactants and products, the program systematically generates all reaction pathways between them. The results are filtered on the fly by pre-defined rules in the language of the Lewis structure and electron-pushing arrows, which determine what structure are "allowed" in the mechanism search. Thus, the amount of human input as well as computational cost become adjustable. Depending on one's need, more specific rules will yield a more restricted search, thus less running time. *Vice versa*. We applied this tool to a substitution reaction, a Diels-Alder reaction and a Claisen ester condensation reaction, and successfully generated the accepted mechanism for all three. The "human input tuning" was shown to be very effective in reducing computational cost while still able to discover the accepted mechanism if applied correctly. In addition, we analyzed the time complexity of our algorithm. It is $O(k * m^{p*a}(1 + m^d)$, where k is the number of intermediates in the network, m is the number of active atoms, p is the number of pairs of electrons allowed to move in one elementary step, a is the exponent of the time complexity of enumerating a single electron-pushing arrow and d is the exponent of the time complexity of deduplication a single SMILES.

A computational simulation of a cryo-SEVI spectrum of ZrO_2 and H_2O adduct. Zirconium oxide is found to have potential applications as catalyst in water splitting reactions. Recently, a high-resolution cryo-SEVI spectrum of the adduct of ZrO_2 and H_2O were produced by our experimental collaborator, which showed dense features in the first 600 cm^{-1} range after the vertical excitation. We found that an umbrella motion of one possible adduct structure may play important roles in the spectrum. Due to high anharmonicity of this mode and its strong coupling with a similar mode, we employed 2D DVR to simulate the FC progressions of this structure. Employing 2D DVR method, we were able to account for the anharmonicity of the umbrella mode, and interpret most of the peaks in the dense vibronic spectra, thus shedding some light on the structure of the adduct.

6.2 Future Work

Although the developed tools for theoretical chemistry show good usability and potential of expanding our chemical knowledge, a number of aspects need further development and closer examination.

The MECP optimization tool is a robust and faster tool compared to previously developed

ones. However, there is still room for improving where the optimizer sometimes goes off the seam near convergence and causes the optimization to take many extra steps. We think this is a systematic error that can be fixed in multiple ways. First, tuning the proportion of the two components in the projected gradient could fix this error. When the structure is far away from the seam, tune up the branching component (the second term in eq. 4.5, to drive it to the seam faster. When the structure is close to the seam, tune down the branching component so that the optimizer does not stray away. This method requires some fine tuning and multi-phase design. The second direction is to use the Hessian to decide the size of each optimization step. Care must be taken in calculating Hessian because the gradient is not a proper derivative of an energy function.

The mechanism generator provides a systematic way of discovering unknown reaction mechanisms. The mechanism search is based on customizable rules which is designed to mimic an electron-pushing model. This tool is able to generate possible mechanisms for up to 8 - 10 reacting atoms depending on the rule set. Having achieved this, there are still a number of improvements that can be made.

- **Thermodynamics analysis**. This provides a filter that filters out high energy intermediates when there are too many reaction pathways to be examined manually. It requires an energy calculation on each intermediate that is generated. A notable difficulty one has to address is that when a generated intermediate contains multiple species, each needs to be properly separated and calculated for their individual energies. In addition, some fragment species appear repeatedly in the reaction network, so building a database that stores a mapping between model chemistry, species and their energies would greatly speed up the mechanism generation.

- **Metals and radicals support.** The tool uses the electron-pushing model as the electron-counting scheme in the enumeration stage, which is based on the rules of Lewis structures. It sometimes fails to describe metal-involving reactions, especially those that involve oxidation and reduction. The new scheme should be based on oxidation state. For radicals, the electron-pushing model can still be used with small modifications (move one electron instead of two).

- **Transition state structures.** Kinetics analysis enables a quantitative study on the reaction network, thus enabling automatic prediction of the most probable reaction mechanism. This requires a reliable way to find the transition structure between every two connecting species in the reaction network. Existing methods all have their limitations. One possible direction is to find a fast way to generate a guess transition state structure, and use methods like quadratic synchronous transit [186], which is known to be reliable when the guess structure is reasonably close to the true transition state.

- **Double-ended mechanism expansion.** The current algorithm starts at the reactant and expands the reaction network in all directions until one branch reaches the product. Most branches go further away from the product and thus are wasteful. One way to avoid this is to expand the reaction network from both ends, until they meet in between. Another way is to define a distance between the reactant and the product on the reaction graph, and only expand in the direction that reduces the distance.

Appendix A

Converged MECP geometries of 7 molecules discussed in Chapter 4

Table A.1: Optimized MECP geometry of Species 1

Atomic	Coordinates (Å)		
Number	X	Y	Z
1	-0.18299	0	-0.12624
6	0.045195	0	0.971858
1	1.166343	0	0.999449

Table A.2: Optimized MECP geometry of Species 2

Atomic	Coordinates (Å)		
Number	X	Y	Z
6	-1.38278	0.427476	0.090213
9	-0.83181	0.684033	1.266212
9	-2.66546	0.750792	0.120724
9	-1.26184	-0.87279	-0.17856
53	-0.34836	1.578812	-1.4977
8	-1.06455	3.364743	-0.3536

Table A.3: Optimized MECP geometry of Species 3

Atomic	Coordinates (Å)		
Number	X	Y	Z
6	-0.87995	3.752969	-0.19013
6	0.508456	3.73792	-0.18956
6	1.116843	5.008979	-0.19017
6	0.508817	6.279689	-0.19126
6	-0.87958	6.264509	-0.1918
6	-1.57336	5.008551	-0.19124
1	-1.44106	2.82504	-0.18973
1	1.084196	2.819466	-0.18872
1	1.084461	7.198197	-0.19165
1	-1.44082	7.19238	-0.19265
1	-2.65905	5.008713	-0.19167

Table A.4: Optimized MECP geometry of Species 4

Atomic Number	Coordinates (Å) X	Y	Z
6	1.784037	1.184435	0.724065
1	1.628462	2.032772	1.374776
6	1.658972	1.186927	-0.68167
1	1.346556	2.018452	-1.29338
6	1.894	-0.14023	-1.12934
1	1.857775	-0.47872	-2.15452
6	2.203413	-0.10377	1.144626
1	2.463291	-0.39433	2.149968
6	2.284315	-0.92684	-0.01775
1	2.608985	-1.95486	-0.0468
6	-1.83663	-0.16192	-1.14273
1	-1.78921	-0.5001	-2.16757
6	-2.22594	-0.95281	-0.03381
1	-2.53862	-1.98448	-0.065
6	-2.16283	-0.12871	1.12895
1	-2.42661	-0.42211	2.132449
6	-1.62006	1.167922	-0.69366
1	-1.31271	2.002858	-1.30329
6	-1.75518	1.164167	0.711141
1	-1.61392	2.014263	1.362819
42	0.025104	-0.45665	0.334616
6	0.0305	-2.06226	1.386456
8	0.033699	-3.03448	2.030752

Table A.5: Optimized MECP geometry of Species 5

Atomic Number	Coordinates (Å) X	Y	Z
6	1.743707	1.21586	0.686358
1	1.543156	2.031211	1.365825
6	1.663092	1.259728	-0.70006
1	1.383228	2.112989	-1.29929
6	1.940466	-0.05186	-1.19941
1	1.983321	-0.33683	-2.24077
6	2.088537	-0.11791	1.072443
1	2.279642	-0.45503	2.079052
6	2.291851	-0.87821	-0.10514
1	2.626486	-1.90157	-0.15593
6	-1.93985	-0.05268	-1.1999
1	-1.98231	-0.33763	-2.24128
6	-2.2912	-0.8792	-0.10574
1	-2.62542	-1.90269	-0.15665
6	-2.08849	-0.11886	1.071914
1	-2.27973	-0.45608	2.078463
6	-1.66309	1.258992	-0.70044
1	-1.3834	2.112382	-1.29956
6	-1.74405	1.215046	0.685965
1	-1.54399	2.030452	1.36551
42	0.000258	-0.62535	0.051698
1	0.000561	-2.24503	-0.41801
1	0.000271	-1.62545	1.405952

Table A.6: Optimized MECP geometry of Species 6

Atomic Number	Coordinates (Å) X	Y	Z	Atomic Number	Coordinates (Å) X	Y	Z
6	-1.94131	-1.15715	-0.6325	1	5.096613	4.801025	-0.74126
6	-0.57228	-1.04245	-0.5166	7	3.494613	3.569099	-0.34978
6	0.060461	0.212418	-0.32002	6	3.69015	1.157669	-0.02981
6	-0.73695	1.416564	-0.24678	1	3.988421	0.249097	-0.57457
6	-2.15121	1.256018	-0.38511	6	4.263684	2.388157	-0.77639
6	-2.72746	0.01586	-0.5649	1	5.321248	2.511864	-0.49857
1	-2.40788	-2.12658	-0.77819	27	1.606448	3.183519	0.147958
1	0.055239	-1.93094	-0.57455	6	0.782691	2.263019	2.969066
1	-2.75149	2.15957	-0.33781	6	0.571785	2.302658	4.345791
1	-3.80876	-0.06025	-0.65935	6	1.162595	3.326032	5.086032
8	-0.24963	2.59632	-0.07068	6	1.939333	4.271062	4.416243
6	1.493063	0.238383	-0.25055	6	2.092819	4.15423	3.036606
1	1.996133	-0.72699	-0.39825	7	1.531073	3.167914	2.321894
7	2.227581	1.286709	-0.04744	1	1.018025	3.388144	6.161066
6	3.60595	8.436195	-0.22527	1	0.334251	1.490274	2.353812
6	4.163335	7.182749	-0.35082	1	-0.04645	1.546756	4.819512
6	3.382908	6.000366	-0.24501	1	2.416074	5.089655	4.94596
6	1.959534	6.098528	-0.00137	1	2.677969	4.875614	2.474917
6	1.41874	7.419045	0.107409	6	4.220206	1.056269	1.407455
6	2.213581	8.540191	0.003708	1	3.762597	0.207938	1.927406
1	4.219094	9.328323	-0.30803	1	5.306665	0.908332	1.400169
1	5.23063	7.077961	-0.54124	1	3.995903	1.964575	1.972831
1	0.349441	7.494479	0.280005	6	4.168406	2.221379	-2.3005
1	1.760598	9.525018	0.097218	1	3.126059	2.086649	-2.60888
8	1.174555	5.086026	0.123641	1	4.561748	3.106147	-2.81179
6	4.038686	4.744421	-0.45134	1	4.744184	1.348827	-2.63108

Table A.7: Optimized MECP geometry of Species 7

Atomic Number	Coordinates (Å) X	Y	Z
29	-0.97182	0.172523	0.97429
29	0.762663	-1.61566	0.968115
6	0.894761	0.252879	0.141821
6	-1.09017	-1.67684	0.108035
6	1.626348	0.958203	-0.5522
6	-1.81203	-2.36909	-0.6089
6	2.463635	1.764602	-1.3646
6	3.387954	2.653045	-0.78498
6	2.379429	1.684669	-2.7669
6	4.202775	3.436943	-1.5879
1	3.457414	2.719361	0.298331
6	3.198325	2.472523	-3.56156
1	1.666129	0.999149	-3.21745
6	4.110216	3.348786	-2.97574
1	4.914578	4.121081	-1.13187
1	3.127168	2.404892	-4.64461
1	4.750714	3.964955	-3.60259
6	-2.64168	-3.1639	-1.43998
6	-3.56949	-4.06114	-0.87925
6	-2.54728	-3.06453	-2.84042
6	-4.37763	-4.83456	-1.6989
1	-3.64649	-4.14212	0.202603
6	-3.35959	-3.84209	-3.65173
1	-1.83135	-2.37224	-3.27619
6	-4.27492	-4.72715	-3.08469
1	-5.09212	-5.52555	-1.25761
1	-3.28065	-3.75954	-4.7332

Atomic Number	Coordinates (Å) X	Y	Z
1	-4.9102	-5.33516	-3.72469
7	-0.94479	2.101716	1.712554
1	-0.96531	2.804536	0.974875
1	-0.05106	2.183624	2.194114
7	-2.90372	0.17365	1.699505
1	-2.78371	-0.41392	2.52752
1	-3.58371	-0.27455	1.089452
7	2.693298	-1.64479	1.701435
1	2.799962	-0.75574	2.186833
1	3.393697	-1.68079	0.962053
7	0.712308	-3.55005	1.685683
1	0.243789	-4.21491	1.074223
1	0.130657	-3.41743	2.515923
6	-2.07457	2.244518	2.65311
1	-1.7784	1.750692	3.584778
1	-2.2979	3.295347	2.87577
6	-3.29116	1.548465	2.06461
1	-3.61932	2.057364	1.150024
1	-4.12664	1.570411	2.776242
6	2.807815	-2.7822	2.63666
1	2.324994	-2.47676	3.571088
1	3.852773	-3.03515	2.855203
6	2.076962	-3.97672	2.04512
1	2.077908	-4.81549	2.753218
1	2.574017	-4.31487	1.127673
17	-0.12423	-0.74884	3.336144

Appendix B

All 32 intermediates in the reaction graph generated for the substitution reaction in Section 2.2.1

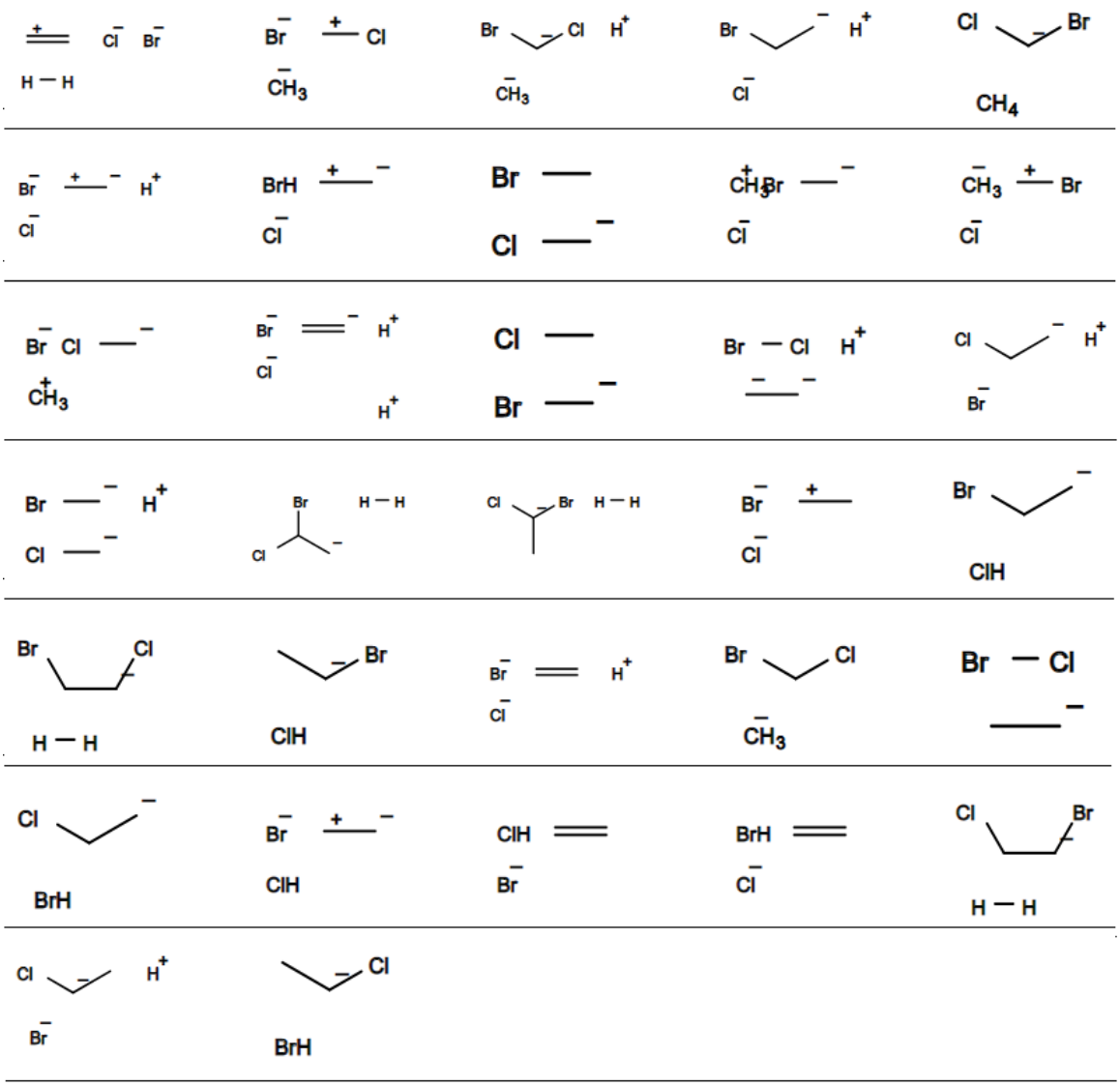

Figure B.1: All 32 intermediates in the reaction graph generated for the substitution reaction in Section 2.2.1

Appendix C

Supporting material for chapter: On the Effect of Spin-Projection on Potential Energy Surfaces

Table C.1: J-couplings calculated by B3LYP before and after geometry change made to binuclear transition metal compound 3, 6, 8, 9

Complex	Before	After	Experiment
3	-35.8	-32.6	-15.7
6	100.4	97.8	84
8	12.1	13.3	18.5
9	75.6[1]	71.3	54.4

1 Peralta, J. E.; Melo, J. I. J. Chem. Theory Comput. **2010**, 6, 1894-1899.

Table C.2: maximum geometric parameter change from crystal structures to AP optimized structures

Geometric parameter/Complex	1	2	3	4	5	6	7	8	9
Bond length(Å)	1.25	0.19	0.26	0.35	0.04	0.10	0.30	0.07	0.35
Metal-involving bond length(Å)	0.03	0.08	0.26	0.05	0.04	0.10	0.12	0.07	0.09
Angles(°)	8.4	12.2	36.1	16.3	3.2	30.5	16.0	8.2	14.2
Metal-involving angles(°)	6.1	3.4	36.1	2.0	3.2	26.8	16.0	8.2	11.8
Dihedrals(°)	15.8	34.2	89.1	35.2	40.1	30.9	21.4	57.5	63.6
Metal-involving dihedrals(°)	12.8	29.8	75.3	21.3	2.7	28.8	21.4	51.7	63.6

Table C.3: J-couplings (in wavenumber) calculated by B3LYP

Complex	1	2	3	4	5	6	7	8	9
S_a[1]	0.5	0.5	2.5	0.5	2	0.5	0.5	1.5	2
S_b	0.5	0.5	0.5	0.5	1.5	0.5	0.5	0.5	0.5
CSP[2]	-90.7	-105.9	-32.7	-101.0	-170.1	100.1	130.6	13.3	71.5
CNP	-45.3	-53.0	-27.2	-50.5	-136.1	50.1	65.3	9.9	57.2
CAP	-89.9	-104.7	-32.6	-100.1	-168.6	97.8	130.2	13.3	71.3
LSP	-88.4	-119.0	-43.3	-122.3	-132.9	157.7	113.0	34.4	115.7
LNP	-44.2	-59.5	-36.1	-61.1	-106.3	78.8	56.5	25.8	92.6
LAP	-87.7	-117.7	-43.2	-121.2	-131.7	154.0	112.7	34.4	115.4
HSP	-88.5	-109.9	-39.9	-91.8	-120.9	182.4	119.6	34.8	129.3
HNP	-44.2	-54.9	-33.3	-45.9	-96.7	91.2	59.8	26.1	103.4
HAP	-87.7	-108.7	-39.8	-91.0	-119.8	178.1	119.3	34.8	129.0
ASP	-93.3	-116.1	-44.1	-121.9	-136.4	132.0	116.1	34.2	112.7
ANP	-46.6	-58.1	-36.7	-60.9	-109.1	66.0	58.1	25.6	90.2
AAP	-92.7	-114.8	-43.9	-120.8	-135.2	129.0	115.8	34.2	112.4
Exp	-30.9	-37.4	-15.7	-107	-110	84.0	57.0	18.5	54.4
S^2_{HS}[3]	2.00	2.01	12.01	2.02	15.84	2.01	2.00	6.03	8.83
S^2_{LS}	1.00	0.99	6.99	1.01	3.73	0.98	1.00	3.03	4.82

1 Spin quantum number of each spin site

2 The first letter denotes geometry, C stands for crystal, L stands for low spin, H stands for high spin, A stands for AP; the last two letters denote method, SP stands for spin projected, NP stands for non projected, AP stands for approximate projection

3 Spin square expectation value at AP geometry for both HS and LS state

Table C.4: J-couplings (in wavenumber) calculated by LC-ωPBE

Complex	1	2	3	4	5	6	7	8	9
S_a [1]	0.5	0.5	2.5	0.5	2	0.5	0.5	1.5	2
S_b	0.5	0.5	0.5	0.5	1.5	0.5	0.5	0.5	0.5
CSP[2]	-44.9	-58.8	-16.7	-63.0	-151.9	314.8	118.1	23.7	62.1
CNP	-22.5	-29.4	-13.9	-31.5	-121.5	157.4	59.0	17.8	49.7
CAP	-43.6	-56.9	-16.3	-61.1	-147.3	300.9	115.2	23.2	60.6
LSP	-27.4	-66.9	-16.7	-83.7	-136.6	314.8	107.5	23.7	62.1
LNP	-13.7	-33.4	-13.9	-41.8	-109.3	157.4	53.8	17.8	49.7
LAP	-27.2	-66.1	-16.7	-83.0	-135.4	307.4	107.2	23.7	62.0
HSP	-25.1	-63.6	-16.6	-66.3	-123.5	343.0	109.5	24.2	64.6
HNP	-12.6	-31.8	-13.8	-33.2	-98.8	171.5	54.7	18.2	51.7
HAP	-24.9	-62.9	-16.5	-65.7	-122.3	334.9	109.2	24.2	64.4
ASP	-29.5	-69.4	-16.8	-110.9	-141.4	287.0	105.3	23.6	61.4
ANP	-14.8	-34.7	-14.0	-55.4	-113.1	143.5	52.7	17.7	49.1
AAP	-29.5	-69.2	-16.8	-110.2	-140.3	283.4	105.2	23.6	61.0
Exp	-30.9	-37.4	-15.7	-107	-110	84.0	57.0	18.5	54.4
S^2_{HS} [3]	2.00	2.01	12.01	2.02	15.84	2.01	2.00	6.03	8.83
S^2_{LS}	1.00	0.99	6.99	1.01	3.73	0.98	1.00	3.03	4.82

1 Spin quantum number of each spin site

2 The first letter denotes geometry, C stands for crystal, L stands for low spin, H stands for high spin, A stands for AP; the last two letters denote method, SP stands for spin projected, NP stands for non projected, AP stands for approximate projection

3 Spin square expectation value at AP geometry for both HS and LS state

Table C.5: J-couplings (in wavenumber) calculated by CAM-B3LYP

Complex	1	2	3	4	5	6	7	8	9
S_a [1]	0.5	0.5	2.5	0.5	2	0.5	0.5	1.5	2
S_b	0.5	0.5	0.5	0.5	1.5	0.5	0.5	0.5	0.5
CSP[2]	-49.5	-60.6	-15.5	-71.8	-143.7	183.8	119.7	10.9	48.1
CNP	-24.8	-30.3	-12.9	-35.9	-115.0	91.9	59.8	8.2	38.5
CAP	-48.0	-58.7	-15.1	-69.7	-139.4	175.7	116.8	10.7	47.0
LSP	-35.9	-73.1	-20.6	-92.8	-122.8	239.8	101.3	25.4	69.6
LNP	-18.0	-36.5	-17.1	-46.4	-98.3	119.9	50.7	19.0	55.6
LAP	-35.6	-72.2	-20.5	-92.0	-121.7	234.2	101.0	25.4	69.4
HSP	-33.6	-69.2	-20.2	-73.8	-113.5	261.1	104.6	25.7	73.0
HNP	-16.8	-34.6	-16.8	-36.9	-90.8	130.6	52.3	19.3	58.4
HAP	-33.3	-68.4	-20.1	-73.2	-112.4	255.0	104.3	25.7	72.8
ASP	-38.9	-75.7	-20.6	-122.9	-125.9	218.5	97.1	25.3	68.7
ANP	-19.5	-37.8	-17.2	-61.5	-100.7	109.2	48.6	19.0	55.0
AAP	-38.9	-75.4	-20.6	-122.2	-125.0	215.6	97.0	25.2	68.3
Exp	-30.9	-37.4	-15.7	-107	-110	84.0	57.0	18.5	54.4
S^2_{HS} [3]	2.00	2.01	12.01	2.02	15.84	2.01	2.00	6.03	8.83
S^2_{LS}	1.00	0.99	6.99	1.01	3.73	0.98	1.00	3.03	4.82

1 Spin quantum number of each spin site

2 The first letter denotes geometry, C stands for crystal, L stands for low spin, H stands for high spin, A stands for AP; the last two letters denote method, SP stands for spin projected, NP stands for non projected, AP stands for approximate projection

3 Spin square expectation value at AP geometry for both HS and LS state

Table C.6: J-couplings (in wavenumber) calculated by ωB97XD

Complex	1	2	3	4	5	6	7	8	9
S_a [1]	0.5	0.5	2.5	0.5	2	0.5	0.5	1.5	2
S_b	0.5	0.5	0.5	0.5	1.5	0.5	0.5	0.5	0.5
CSP[2]	-47.9	-60.8	-15.6	-79.1	-148.3	179.7	127.9	13.1	49.9
CNP	-24.0	-30.4	-13.0	-39.6	-118.6	89.9	63.9	9.8	39.9
CAP	-46.5	-58.8	-15.2	-76.8	-143.8	171.7	124.8	12.8	48.7
LSP	-33.7	-63.4	-20.4	-97.9	-128.4	222.5	115.2	27.6	71.9
LNP	-16.9	-31.7	-17.0	-49.0	-102.7	111.3	57.6	20.7	57.5
LAP	-33.4	-62.7	-20.3	-97.1	-127.2	217.3	114.9	27.6	71.7
HSP	-31.7	-61.1	-20.0	-79.8	-118.0	243.0	117.1	28.0	75.2
HNP	-15.9	-30.5	-16.7	-39.9	-94.4	121.5	58.5	21.0	60.2
HAP	-31.4	-60.4	-19.9	-79.1	-116.9	237.2	116.8	28.0	75.1
ASP	-36.1	-65.7	-20.5	-127.3	-132.0	202.7	113.0	27.5	71.1
ANP	-18.0	-32.9	-17.1	-63.6	-105.6	101.3	56.5	20.6	56.9
AAP	-36.0	-65.5	-20.5	-126.3	-131.0	200.1	112.8	27.5	70.7
Exp	-30.9	-37.4	-15.7	-107	-110	84.0	57.0	18.5	54.4
S^2_{HS} [3]	2.00	2.01	12.01	2.02	15.84	2.01	2.00	6.03	8.83
S^2_{LS}	1.00	0.99	6.99	1.01	3.73	0.98	1.00	3.03	4.82

1 Spin quantum number of each spin site

2 The first letter denotes geometry, C stands for crystal, L stands for low spin, H stands for high spin, A stands for AP; the last two letters denote method, SP stands for spin projected, NP stands for non projected, AP stands for approximate projection

3 Spin square expectation value at AP geometry for both HS and LS state

Table C.7: Errors of spin crossover gaps of a selection of complexes calculated by AP with B3LYP/6-311G* and B3LYP/LACV3P, and by DBLOC (B3LYP/LACV3P)

complex	6-311G*	LACV3P	DBLOC
cr223tetcl2	0.93	0.53	1.82
crcn6	3.36	5.17	5.73
mncn6	0.10	0.92	0.47
fe(3)cn6	4.04	3.43	3.58
col2	10.58	12.56	0.56
coterpy	4.45	3.62	1.89
nibipy3	5.09	9.04	0.95
nidpdpm2h2o2	2.22	6.20	0.20
niphen3	5.09	8.96	6.23
mnen3	3.11	3.64	4.22
MAE	3.90	5.41	2.57

Table C.8: Spin crossover gaps (kcal/mol) on crystal, optimized ground state and optimized AP-corrected ground state geometries calculated by B3LYP/6-311G(d) **considering solvent effect** and their errors wrt. experiments

complex	G1	G2	G3	G4	exp.	E1	E3	E4	E0
cr(3)f6	24.80	25.40	38.09	38.33	40.37	15.57	2.28	2.04	1.30
cr223tetcl2	24.18	23.78	35.60	36.24	36.53	12.35	0.93	0.29	1.82
crccsime36	20.94	21.49	32.23	32.63	33.52	12.58	1.29	0.89	2.61
crcn6	21.18	22.96	34.36	35.68	31	9.82	3.36	4.68	5.73
crcyclamncs2	23.11	23.22	34.79	35.14	34.54	11.43	0.25	0.60	3.43
cren3	25.38	25.81	38.65	38.83	38.67	13.29	0.02	0.16	1.56
crnh34cl2	25.15	24.86	37.24	37.83	36.95	11.80	0.29	0.88	2.31
crnh36	25.78	25.98	38.92	39.29	39.15	13.37	0.23	0.14	0.82
crox3	23.77	23.86	35.76	36.20	36.53	12.76	0.77	0.33	1.24
mnf6	25.87	25.78	38.57	39.25	41.24	15.37	2.67	1.99	1.31
mn2p2pameth2	11.70	11.45	22.24	22.19	46.55	34.85	24.31	24.36	4.47
mncn6	11.87	12.21	24.20	26.51	24.1	12.23	0.10	2.41	0.47
crf6	13.22	13.15	26.13	25.39	28.09	14.87	1.96	2.70	3.87
vf6	12.68	12.87	25.69	23.97	24.66	11.98	1.03	0.69	1.04
vurea6	12.13	12.24	24.42	24.55	23.99	11.86	0.43	0.56	0.41
fe(3)cn6	62.21	48.95	49.18	57.61	45.14	17.07	4.04	12.47	3.58
feen3	22.62	18.90	19.09	18.81	18.89	3.73	0.20	0.08	2.18
coamn3s3sarh	29.59	31.92	31.92	31.23	33.61	4.02	1.69	2.38	0.42
coamn5ssarh	32.11	31.68	31.68	34.49	32.48	0.37	0.80	2.01	3.85
coen3	37.23	37.20	37.20	36.69	32.33	4.90	4.87	4.36	1.81
coetn4s2amp	31.27	31.88	31.88	31.45	32.62	1.35	0.74	1.17	0.52
col2	34.80	34.32	34.32	34.19	23.74	11.06	10.58	10.45	0.56
con3s3	29.54	31.69	31.69	31.26	34.72	5.18	3.03	3.46	1.16
conh35soch32	28.39	28.94	28.94	28.50	26.22	2.17	2.72	2.28	1.59
conh36	35.78	35.62	35.62	35.30	30.33	5.45	5.29	4.97	0.66
fe(2)cn6	69.80	56.66	56.66	59.57	60.93	8.87	4.27	1.36	3.33
fe2amp3	-13.18	19.59	19.59	19.34	5.26	18.44	14.33	14.08	6.25
febptnncs2	-18.73	22.14	22.14	21.64	0	18.73	22.14	21.64	3.98
fehbpz32	42.83	27.94	27.94	27.78	4.54	38.29	23.40	23.24	6.74
fepapth2	-18.39	20.29	20.29	19.90	3.82	22.21	16.47	16.08	0.05
fephen2ncs2	25.28	23.98	23.98	23.19	0	25.28	23.98	23.19	0.14
fephen2ncse2	26.67	24.57	24.57	23.85	0	26.67	24.57	23.85	0.69
fepybzimh3	-1.63	19.20	19.20	18.73	5.02	6.65	14.18	13.71	0.05
fetacn2	29.48	18.73	18.73	18.67	5.5	23.98	13.23	13.17	10.16
fetpancs2	-1.73	22.88	22.88	22.05	0	1.73	22.88	22.05	2.19
fetpen	38.66	22.87	22.87	22.60	0	38.66	22.87	22.60	5.83
fetppn3	38.88	23.00	23.00	22.72	6.69	32.19	16.31	16.03	3.83
copyimine22	14.35	9.93	9.96	9.74	3.35	11.00	6.61	6.39	3.56
coterpy	9.47	7.54	7.56	7.38	3.11	6.36	4.45	4.27	1.89
ni2meim6	15.88	15.96	31.90	31.86	28.47	12.59	3.43	3.39	0.72
nibipy3	0.06	15.12	30.20	30.23	25.11	25.05	5.09	5.12	0.95
nibpm2no3	12.54	15.19	30.10	29.99	27.64	15.10	2.46	2.35	0.79
nidmso6	15.68	16.27	32.54	32.32	30.94	15.26	1.60	1.38	2.39
nidpdpm2h2o2	15.52	15.67	31.17	31.23	28.95	13.43	2.22	2.28	0.20
nidpdpm2no3h2o	15.43	15.45	30.76	30.91	28.95	13.52	1.81	1.96	0.64
nidpdpmno32ch3cn	15.23	15.48	30.90	30.81	28.95	13.72	1.95	1.86	3.84
nidpdpmno32	9.44	14.82	29.35	29.51	28.95	19.51	0.40	0.56	0.64
niedta	9.83	15.07	30.11	30.30	27	17.17	3.11	3.30	0.93
nien2scn2	13.20	13.56	26.46	26.44	27.03	13.83	0.57	0.59	0.83
nien3	0.05	15.16	30.31	30.39	26.08	26.03	4.23	4.31	6.89
nif6 (M062x)	18.16	17.77	35.54	35.65	33.72	15.56	1.82	1.93	3.21

Table C.8: Spin crossover gaps (kcal/mol) on crystal, optimized ground state and optimized AP-corrected ground state geometries calculated by B3LYP/6-311G(d) **considering solvent effect** and their errors wrt. experiments

complex	G1	G2	G3	G4	exp.	E1	E3	E4	E0
nigly3	11.83	15.18	30.10	30.11	28.29	16.46	1.81	1.82	0.22
nih2o6	9.36	17.19	34.38	34.23	33.03	23.67	1.35	1.20	2.95
ninh36	12.55	15.70	31.39	31.51	28.23	15.68	3.16	3.28	0.22
niphen3	1.89	15.08	30.25	30.35	25.16	23.27	5.09	5.19	6.23
nipyrazole6	18.42	15.72	31.42	31.58	28.86	10.44	2.56	2.72	0.25
nitach3mepyr	12.00	14.69	29.35	29.57	23.14	11.14	6.21	6.43	4.59
nitpm2	0.03	15.47	30.91	31.26	27.78	27.75	3.13	3.48	0.85
nitpmno32	11.81	15.40	30.75	30.90	27.58	15.77	3.17	3.32	1.38
feh2o6	17.34	30.11	30.94	30.07	29.19	11.85	1.75	0.88	3.42
fethiocarbamate3	2.97	8.48	9.01	9.18	11.75	8.78	2.74	2.57	0.94
fetrencam	15.29	27.40	27.72	29.01	22.9	7.61	4.82	6.11	3.24
mnden2	20.49	37.99	42.83	42.36	39.05	18.56	3.78	3.31	4.30
mnen	19.07	37.06	41.16	38.70	38.05	18.98	3.11	0.65	4.22
mnh2o6	39.32	42.42	49.19	46.23	47.12	7.80	2.07	0.89	2.45
MAE						14.80	5.83	5.92	2.38
MAE without alpha=1						14.92	3.03	3.22	2.20

1 G1-G4 stand for spin crossover gap on different geometries, G1 is crystal structure, G2 is UDFT geometry, G3 is UDFT//AP, G4 is the AP//AP
2 E1, E3, E4 corresponds to the error wrt. to experiments for G1, G3, G4, and E0 stands for the error of DBLOC method

Table C.9: Spin crossover gaps (kcal/mol) on crystal, optimized ground state and optimized AP-corrected ground state geometries calculated by B3LYP/6-311G(d) **not considering solvent effect** and their errors wrt. experiments

complex	G1	G2	G3	G4	exp.	E1	E3	E4	E0
cr(3)f6	24.80	25.40	38.09	38.33	40.37	15.57	2.28	2.04	1.30
cr223tetcl2	24.18	23.78	35.60	36.24	36.53	12.35	0.93	0.29	1.82
crccsime36	20.94	21.49	32.23	32.63	33.52	12.58	1.29	0.89	2.61
crcn6	21.18	22.96	34.36	35.68	31	9.82	3.36	4.68	5.73
crcyclamncs2	22.17	22.10	33.12	33.46	34.54	12.37	1.42	1.08	3.43
cren3	25.38	25.63	38.36	39.08	38.67	13.29	0.31	0.41	1.56
crnh34cl2	24.68	23.95	35.50	35.68	36.95	12.27	1.45	1.27	2.31
crnh36	25.74	26.04	38.99	39.67	39.15	13.41	0.16	0.52	0.82
crox3	23.79	23.92	35.83	36.21	36.53	12.74	0.70	0.32	1.24
mnf6	25.87	25.78	38.57	39.25	41.24	15.37	2.67	1.99	1.31
mn2p2pameth2	11.71	11.33	21.94	21.26	46.55	34.84	24.61	25.29	4.47
mncn6	11.87	12.56	24.89	24.90	24.1	12.23	0.79	0.80	0.47
crf6	13.22	13.15	26.13	25.39	28.09	14.87	1.96	2.70	3.87
vf6	12.68	12.87	25.69	23.97	24.66	11.98	1.03	0.69	1.04
vurea6	12.13	12.24	24.42	24.55	23.99	11.86	0.43	0.56	0.41
fe(3)cn6	62.60	42.32	42.55	42.35	45.14	17.46	2.59	2.79	3.58
feen3	22.62	18.90	19.09	18.81	18.89	3.73	0.20	0.08	2.18
coamn3s3sarh	29.59	31.92	31.92	31.23	33.61	4.02	1.69	2.38	0.42
coamn5ssarh	32.11	31.68	31.68	34.49	32.48	0.37	0.80	2.01	3.85
coen3	37.47	33.73	33.73	41.27	32.33	5.14	1.40	8.94	1.81

Table C.9: Spin crossover gaps (kcal/mol) on crystal, optimized ground state and optimized AP-corrected ground state geometries calculated by B3LYP/6-311G(d) **not considering solvent effect** and their errors wrt. experiments

complex	G1	G2	G3	G4	exp.	E1	E3	E4	E0
coetn4s2amp	31.27	31.88	31.88	31.45	32.62	1.35	0.74	1.17	0.52
col2	34.98	34.06	34.06	33.92	23.74	11.24	10.32	10.18	0.56
con3s3	29.54	31.69	31.69	31.26	34.72	5.18	3.03	3.46	1.16
conh35soch32	28.91	25.33	25.33	25.18	26.22	2.69	0.89	1.04	1.59
conh36	36.45	30.96	30.96	30.85	30.33	6.12	0.63	0.52	0.66
fe(2)cn6	70.36	41.76	41.76	44.52	30.33		11.43	14.19	3.33
fe2amp3	-13.18	19.59	19.59	19.34	5.26	7.92	14.33	14.08	6.25
febptnncs2	-18.73	22.14	22.14	21.64	0	18.73	22.14	21.64	3.98
fehbpz32	42.83	27.94	27.94	27.78	4.54	38.29	23.40	23.24	6.74
fepapth2	-18.39	20.29	20.29	19.90	3.82	14.57	16.47	16.08	0.05
fephen2ncs2	25.28	23.98	23.98	23.19	0	25.28	23.98	23.19	0.14
fephen2ncse2	26.67	24.57	24.57	23.85	0	26.67	24.57	23.85	0.69
fepybzimh3	-1.63	19.20	19.20	18.73	5.02	3.39	14.18	13.71	0.05
fetacn2	29.48	18.73	18.73	18.67	5.5	23.98	13.23	13.17	10.16
fetpancs2	-1.73	22.88	22.88	22.05	0	1.73	22.88	22.05	2.19
fetpen	38.66	22.87	22.87	22.60	0	38.66	22.87	22.60	5.83
fetppn3	38.88	23.00	23.00	22.72	6.69	32.19	16.31	16.03	3.83
copyimine22	14.35	9.93	9.96	9.74	3.35	11.00	6.61	6.39	3.56
coterpy	9.47	7.54	7.56	7.38	3.11	6.36	4.45	4.27	1.89
ni2meim6	15.88	15.94	31.87	31.88	28.47	12.59	3.40	3.41	0.72
nibipy3	0.07	15.09	30.16	30.24	25.11	25.04	5.05	5.13	0.95
nibpm2no3	12.49	15.28	30.48	30.46	27.64	15.15	2.84	2.82	0.79
nidmso6	15.66	16.22	32.44	32.42	30.94	15.28	1.50	1.48	2.39
nidpdpm2h2o2	15.36	15.47	30.71	30.80	28.95	13.59	1.76	1.85	0.20
nidpdpm2no3h2o	15.45	15.59	31.15	30.99	28.95	13.50	2.20	2.04	0.64
nidpdpmno32ch3cn	15.00	15.11	30.14	30.15	28.95	13.95	1.19	1.20	3.84
nidpdpmno32	12.27	15.02	30.01	30.20	28.95	16.68	1.06	1.25	0.64
niedta	8.81	15.23	30.44	30.50	27	18.19	3.44	3.50	0.93
nien2scn2	13.12	13.57	26.85	26.96	27.03	13.91	0.18	0.07	0.83
nien3	0.05	15.16	30.31	30.39	26.08	26.03	4.23	4.31	6.89
nif6 (M062x)	18.16	17.77	35.54	35.65	33.72	15.56	1.82	1.93	3.21
nigly3	10.73	11.20	20.29	20.41	28.29	17.56	8.00	7.88	0.22
nih2o6	9.72	17.44	34.87	34.71	33.03	23.31	1.84	1.68	2.95
ninh36	12.55	15.70	31.39	31.51	28.23	15.68	3.16	3.28	0.22
niphen3	1.90	15.14	30.25	30.37	25.16	23.26	5.09	5.21	6.23
nipyrazole6	18.42	15.72	31.42	31.58	28.86	10.44	2.56	2.72	0.25
nitach3mepyr	12.03	14.76	29.49	29.61	23.14	11.11	6.35	6.47	4.59
nitpm2	0.03	15.47	30.91	31.26	27.78	27.75	3.13	3.48	0.85
nitpmno32	10.74	15.12	30.23	30.33	27.58	16.84	2.65	2.75	1.38
feh2o6	16.84	32.27	34.11	34.11	29.19	12.35	4.92	4.92	3.42
fethiocarbamate3	3.25	8.60	9.12	9.27	11.75	8.50	2.63	2.48	0.94
fetrencam	15.29	27.40	27.72	29.01	22.9	7.61	4.82	6.11	3.24
mnden2	20.10	36.47	36.59	38.07	39.05	18.95	2.46	0.98	4.30
mnen3	18.78	37.19	37.28	38.97	38.05	19.27	0.77	0.92	4.22
mnh2o6	39.14	43.25	43.28	47.75	47.12	7.98	3.84	0.63	2.45
MAE						14.71	5.83	5.92	2.38
MAE without alpha=1						14.98	3.04	2.98	2.20

1 G1-G4 stand for spin crossover gap on different geometries, G1 is crystal structure, G2 is UDFT geometry, G3 is UDFT//AP, G4 is the AP//AP

2 E1, E3, E4 corresponds to the error wrt. to experiments for G1, G3, G4, and E0 stands for the error of DBLOC method

Bibliography

[1] E. Schrödinger, An undulatory theory of the mechanics of atoms and molecules, Phys. Rev. 28 (1926) 1049–1070. doi:10.1103/PhysRev.28.1049.

[2] M. Born, W. Heisenberg, Zur quantentheorie der molekeln, Annalen der Physik 379 (9) (1924) 1–31.

[3] D. R. Hartree, The wave mechanics of an atom with a non-coulomb central field. part ii. some results and discussion, in: Mathematical Proceedings of the Cambridge Philosophical Society, Vol. 24, Cambridge University Press, 1928, pp. 111–132.

[4] J. C. Slater, Note on hartree's method, Physical Review 35 (2) (1930) 210.

[5] V. Fock, Näherungsmethode zur lösung des quantenmechanischen mehrkörperproblems, Zeitschrift für Physik 61 (1-2) (1930) 126–148.

[6] W. Hehre, L. Radom, R. Schleyer, P. J., AB INITIO Molecular Orbital Theory, Wiley-Interscience, 1986.

[7] M. Head-Gordon, R. J. Rico, M. Oumi, T. J. Lee, A doubles correction to electronic excited states from configuration interaction in the space of single substitutions, Chemical Physics Letters 219 (1) (1994) 21 – 29.

[8] J. A. Pople, M. Head-Gordon, K. Raghavachari, Quadratic configuration interaction. a general technique for determining electron correlation energies, The Journal of chemical physics 87 (10) (1987) 5968–5975.

[9] G. D. Purvis III, R. J. Bartlett, A full coupled-cluster singles and doubles model: The inclusion of disconnected triples, The Journal of Chemical Physics 76 (4) (1982) 1910–1918.

[10] K. Raghavachari, G. W. Trucks, J. A. Pople, M. Head-Gordon, A fifth-order perturbation comparison of electron correlation theories, Chemical Physics Letters 157 (6) (1989) 479–483.

[11] T. Van Voorhis, M. Head-Gordon, Two-body coupled cluster expansions, The Journal of Chemical Physics 115 (11) (2001) 5033–5040.

[12] C. Møller, M. S. Plesset, Note on an approximation treatment for many-electron systems, Physical Review 46 (7) (1934) 618.

[13] R. Krishnan, J. A. Pople, Approximate fourth-order perturbation theory of the electron correlation energy, International Journal of Quantum Chemistry 14 (1) (1978) 91–100.

[14] L. H. Thomas, The calculation of atomic fields, in: Mathematical Proceedings of the Cambridge Philosophical Society, Vol. 23, Cambridge University Press, 1927, pp. 542–548.

[15] E. Fermi, Eine statistische methode zur bestimmung einiger eigenschaften des atoms und ihre anwendung auf die theorie des periodischen systems der elemente, Zeitschrift für Physik 48 (1-2) (1928) 73–79.

[16] F. Jensen, Introduction to computational chemistry, John wiley & sons, 2017.

[17] W. Kohn, L. J. Sham, Self-consistent equations including exchange and correlation effects, Physical review 140 (4A) (1965) A1133.

[18] J. P. Perdew, A. Ruzsinszky, J. Tao, V. N. Staroverov, G. E. Scuseria, G. I. Csonka, Prescription for the design and selection of density functional approximations: More constraint satisfaction with fewer fits, The Journal of chemical physics 123 (6) (2005) 062201.

[19] J. P. Perdew, A. Ruzsinszky, L. A. Constantin, J. Sun, G. I. Csonka, Some fundamental issues in ground-state density functional theory: A guide for the perplexed, Journal of chemical theory and computation 5 (4) (2009) 902–908.

[20] A. Ruzsinszky, J. P. Perdew, Twelve outstanding problems in ground-state density functional theory: A bouquet of puzzles, Computational and Theoretical Chemistry 963 (1) (2011) 2–6.

[21] C. D. Sherrill, M. S. Lee, M. Head-Gordon, On the performance of density functional theory for symmetry-breaking problems, Chemical physics letters 302 (5-6) (1999) 425–430.

[22] A. J. Cohen, P. Mori-Sánchez, W. Yang, Insights into current limitations of density functional theory, Science 321 (5890) (2008) 792–794.

[23] P. Pulay, Ab initio calculation of force constants and equilibrium geometries in polyatomic molecules: I. theory, Molecular Physics 17 (2) (1969) 197–204.

[24] R. H. Crabtree, Multifunctional ligands in transition metal catalysis, New J. Chem. 35 (1) (2011) 18. doi:10.1039/c0nj00776e.

[25] C. Murray, S. Sun, H. Doyle, T. Betley, Monodisperse 3d Transition-Metal (Co,Ni,Fe) Nanoparticles and Their Assembly intoNanoparticle Superlattices, MRS Bull. 26 (12) (2001) 985–991. doi:10.1557/mrs2001.254.

[26] L. A. Finney, T. V. O'Halloran, Transition metal speciation in the cell: Insights from the chemistry of metal ion receptor, Science 300 (5621) (2003) 931–936. doi:10.1126/science.1085049.

[27] G. Christou, D. Gatteschi, D. N. Hendrickson, R. Sessoli, Single-Molecule Magnets, MRS Bull. 25 (11) (2000) 66–71. doi:10.1557/mrs2000.226.

[28] J.-S. Wang, K. Matyjaszewski, Controlled"Living" Radical Polymerization. Atom Transfer Radical Polymerization in the Presence of Transition-Metal Complexes, J. Am. Chem. Soc. 117 (6) (1995) 5614–5615. arXiv:JA950538I, doi:10.1021/ja00125a035.

[29] M. Reiher, A theoretical challenge: Transition-metal compounds, CHIMIA International Journal for Chemistry 63 (3) (2009) 140–145.

[30] E. R. Davidson, Computational Transition Metal Chemistry (special issue, 2), Chemical Review 100 (2) (2000) 351–818.

[31] A. Szabo, N. S. Ostlund, Modern quantum chemistry: introduction to advanced electronic structure theory, Courier Corporation, 2012.

[32] J. L. Sonnenberg, H. B. Schlegel, H. P. Hratchian, Spin Contamination in Inorganic Chemistry Calculations, Encycl. Inorg. Chem.doi:10.1002/0470862106.ia617.

[33] K. N. Houk, P. H.-Y. Cheong, Computational prediction of small-molecule catalysts, Nature 455 (7211) (2008) 309.

[34] P. H.-Y. Cheong, C. Y. Legault, J. M. Um, N. Celebi-Olcum, K. N. Houk, Quantum mechanical investigations of organocatalysis: mechanisms, reactivities, and selectivities, Chem. Rev. 111 (8) (2011) 5042–5137.

[35] F. Himo, Quantum chemical modeling of enzyme active sites and reaction mechanisms, Theor. Chem. Acc. 116 (1-3) (2006) 232–240.

[36] K. Rudolf, D. C. Spellmeyer, K. N. Houk, Prediction and experimental verification of the stereoselective electrocyclization of 3-formylcyclobutene, J. Org. Chem. 52 (16) (1987) 3708–3710.

[37] S. Bahmanyar, K. N. Houk, The origin of stereoselectivity in proline-catalyzed intramolecular aldol reactions, J. Am. Chem. Soc. 123 (51) (2001) 12911–12912.

[38] G. N. Simm, A. C. Vaucher, M. Reiher, Exploration of Reaction Pathways and Chemical Transformation Networks, J. Phys. Chem. A.

[39] A. L. Dewyer, A. J. Argüelles, P. M. Zimmerman, Methods for exploring reaction space in molecular systems, Wiley Interdiscip. Rev. Comput. Mol. Sci. 8 (2) (2018) e1354.

[40] S. Maeda, K. Morokuma, Communications: A systematic method for locating transition structures of A+BX type reactions, J. Chem. Phys. 132 (24) (2010) 1–5. doi:10.1063/1.3457903.

[41] S. Maeda, T. Taketsugu, K. Morokuma, K. Ohno, Anharmonic downward distortion following for automated exploration of quantum chemical potential energy surfaces, Bull. Chem. Soc. Jpn. 87 (12) (2014) 1315–1334. doi:10.1246/bcsj.20140189.

[42] L. P. Wang, R. T. McGibbon, V. S. Pande, T. J. Martinez, Automated Discovery and Refinement of Reactive Molecular Dynamics Pathways, J. Chem. Theory Comput. 12 (2) (2016) 638–649. doi:10.1021/acs.jctc.5b00830.

[43] K. Ohno, S. Maeda, Global reaction route mapping on potential energy surfaces of formaldehyde, formic acid, and their metal-substituted analogues, J. Phys. Chem. A 110 (28) (2006) 8933–8941.

[44] S. Maeda, T. Taketsugu, K. Morokuma, Exploring transition state structures for intramolecular pathways by the artificial force induced reaction method, J. Comput. Chem. 35 (2) (2014) 166–173.

[45] S. Maeda, Y. Harabuchi, M. Takagi, T. Taketsugu, K. Morokuma, Artificial force induced reaction (AFIR) method for exploring quantum chemical potential energy surfaces, Chem. Rec. 16 (5) (2016) 2232–2248.

[46] D. Rappoport, C. J. Galvin, D. Y. Zubarev, A. Aspuru-Guzik, Complex Chemical Reaction Networks from Heuristics-Aided Quantum Chemistry, J. Chem. Theory Comput. 10 (3) (2014) 897–907. doi:10.1021/ct401004r.

[47] P. M. Zimmerman, Automated discovery of chemically reasonable elementary reaction steps, J. Comput. Chem. 34 (16) (2013) 1385–1392. doi:10.1002/jcc.23271.

[48] M. Bergeler, G. N. Simm, J. Proppe, M. Reiher, Heuristics-Guided Exploration of Reaction Mechanisms, J. Chem. Theory Comput. 11 (12) (2015) 5712–5722. arXiv:arXiv:1509.03120v1, doi:10.1021/acs.jctc.5b00866.

[49] Y. Kim, J. W. Kim, Z. Kim, W. Y. Kim, Efficient prediction of reaction paths through molecular graph and reaction network analysis, Chem. Sci.doi:10.1039/C7SC03628K.

[50] Y. V. Suleimanov, W. H. Green, Automated Discovery of Elementary Chemical Reaction Steps Using Freezing String and Berny Optimization Methods, J. Chem. Theory Comput. 11 (9) (2015) 4248–4259. doi:10.1021/acs.jctc.5b00407.

[51] P. M. Zimmerman, Navigating molecular space for reaction mechanisms: an efficient, automated procedure, Mol. Simul. 41 (1-3) (2015) 43–54.

[52] S. Habershon, Sampling reactive pathways with random walks in chemical space: Applications to molecular dissociation and catalysis, J. Chem. Phys.doi:10.1063/1.4929992.

[53] D. Weininger, Smiles, a chemical language and information system. 1. introduction to methodology and encoding rules, Journal of chemical information and computer sciences 28 (1) (1988) 31–36.

[54] D. Weininger, A. Weininger, J. L. Weininger, Smiles. 2. algorithm for generation of unique smiles notation, Journal of chemical information and computer sciences 29 (2) (1989) 97–101.

[55] D. Weininger, Smiles. 3. depict. graphical depiction of chemical structures, Journal of chemical information and computer sciences 30 (3) (1990) 237–243.

[56] Smiles specifications, `http://www.daylight.com/dayhtml/doc/theory/theory.smiles.html`.

[57] T. A. Halgren, Merck molecular force field. i. basis, form, scope, parameterization, and performance of mmff94, Journal of computational chemistry 17 (5-6) (1996) 490–519.

[58] T. A. Halgren, Merck molecular force field. ii. mmff94 van der waals and electrostatic parameters for intermolecular interactions, Journal of Computational Chemistry 17 (5-6) (1996) 520–552.

[59] T. A. Halgren, Merck molecular force field. iii. molecular geometries and vibrational frequencies for mmff94, Journal of computational chemistry 17 (5-6) (1996) 553–586.

[60] T. A. Halgren, R. B. Nachbar, Merck molecular force field. iv. conformational energies and geometries for mmff94, Journal of computational chemistry 17 (5-6) (1996) 587–615.

[61] T. A. Halgren, Merck molecular force field. v. extension of mmff94 using experimental data, additional computational data, and empirical rules, Journal of Computational Chemistry 17 (5-6) (1996) 616–641.

[62] A. K. Rappé, C. J. Casewit, K. Colwell, W. A. Goddard III, W. Skiff, Uff, a full periodic table force field for molecular mechanics and molecular dynamics simulations, Journal of the American chemical society 114 (25) (1992) 10024–10035.

[63] J. Wang, R. M. Wolf, J. W. Caldwell, P. A. Kollman, D. A. Case, Development and testing of a general amber force field, Journal of computational chemistry 25 (9) (2004) 1157–1174.

[64] J. Dugundji, I. Ugi, An algebraic model of constitutional chemistry as a basis for chemical computer programs, in: Comput. Chem., Springer, 1973, pp. 19–64.

[65] W. O. Kermack, R. Robinson, LI.An explanation of the property of induced polarity of atoms and an interpretation of the theory of partial valencies on an electronic basis, J. Chem. Soc. Trans. 121 (1922) 427–440.

[66] J. Hopcroft, R. Tarjan, Algorithm 447: efficient algorithms for graph manipulation, Commun. ACM 16 (6) (1973) 372–378.

[67] J. E. Hopcroft, J.-K. Wong, Linear time algorithm for isomorphism of planar graphs (preliminary report), in: Proc. sixth Annu. ACM Symp. Theory Comput., ACM, 1974, pp. 172–184.

[68] F. A. Carey, Organic Chemistry, 6th Edition, NY: McGraw-Hill, 2006.

[69] J. McMurry, Organic Chemistry, 4th Edition, Brooks/Cole Publishing Company, 1995.

[70] X. Sheng, L. Thompson, H. Hratchiandoi:https://doi.org/10.26434/chemrxiv.7976474.v2.

[71] A. J. Cohen, P. Mori-Sánchez, W. T. Yang, Insights into current limitations of density functional theory, Science 321 (5890) (2008) 792.

[72] L. M. Thompson, C. C. Jarrold, H. P. Hratchian, Explaining the movo 4- photoelectron spectrum: Rationalization of geometric and electronic structure, The Journal of chemical physics 146 (10) (2017) 104301.

[73] L. M. Thompson, H. P. Hratchian, Modeling the Photoelectron Spectra of $MoNbO_2$– Accounting for Spin Contamination in Density Functional Theory, The Journal of Physical Chemistry A 119 (32) (2015) 8744–8751.

[74] L. M. Thompson, H. P. Hratchian, On approximate projection models, Molecular Physics 0 (0) (2018) 1–9. arXiv:https://doi.org/10.1080/00268976.2018.1554828, doi:10.1080/00268976.2018.1554828.

[75] A. J. Garza, C. A. Jiménez-Hoyos, G. E. Scuseria, Capturing static and dynamic correlations by a combination of projected Hartree-Fock and density functional theories, J. Chem. Phys. 138 (13). doi:10.1063/1.4796545.

[76] C. A. Jiménez-Hoyos, T. M. Henderson, T. Tsuchimochi, G. E. Scuseria, Projected Hartree-Fock theory, J. Chem. Phys. 136 (16). arXiv:arXiv:1202.3148v1, doi:10.1063/1.4705280.

[77] G. E. Scuseria, C. A. Jiménez-Hoyos, T. M. Henderson, K. Samanta, J. K. Ellis, Projected quasiparticle theory for molecular electronic structure, J. Chem. Phys. 135 (12). arXiv:1106.0956, doi:10.1063/1.3643338.

[78] H. B. Schlegel, Spin contamination (1998). doi:10.1002/0470845015.csa020.

[79] K. Yamaguchi, F. Jensen, A. Dorigo, K. Houk, a spin correction procedure for unrestricted hartree-fock and moller-plesset wavefunctions for singlet diradicals and polyradicals, Chem. Phys. Lett. 149 (1988) 537–542.

[80] T. Saito, S. Nishihara, Y. Kataoka, Y. Nakanishi, T. Matsui, Y. Kitagawa, T. Kawakami, M. Okumura, K. Yamaguchi, Transition state optimization based on approximate spin-projection (AP) method, Chem. Phys. Lett. 483 (1-3) (2009) 168–171. doi:10.1016/j.cplett.2009.10.055.

[81] T. Saito, A. Ito, T. Watanabe, T. Kawakami, M. Okumura, K. Yamaguchi, Performance of the coupled cluster and DFT methods for through-space magnetic interactions of nitroxide dimer, Chem. Phys. Lett. 542 (2012) 19–25. doi:10.1016/j.cplett.2012.05.046.

[82] L. M. Thompson, H. P. Hratchian, Modeling the Photoelectron Spectra of $MoNbO_2$ Accounting for Spin Contamination in Density Functional Theory, J. Phys. Chem. A 119 (32) (2015) 8744–8751. doi:10.1021/acs.jpca.5b04625.

[83] J. I. Melo, J. J. Phillips, J. E. Peralta, Structural dependence of magnetic exchange coupling parameters in transition-metal complexes, Chem. Phys. Lett. 557 (2013) 110–113. doi:10.1016/j.cplett.2012.12.013.

[84] H. P. Hratchian, Communication: an efficient analytic gradient theory for approximate spin projection methods., J. Chem. Phys. 138 (10) (2013) 101101. doi:10.1063/1.4795429.

[85] L. M. Thompson, H. P. Hratchian, Second derivatives for approximate spin projection methods, J. Chem. Phys. 142 (2015) 054106. doi:10.1063/1.4907269.

[86] M. J. Frisch, G. W. Trucks, H. B. Schlegel, G. E. Scuseria, M. A. Robb, J. R. Cheeseman, G. Scalmani, V. Barone, B. Mennucci, G. A. Petersson, H. Nakatsuji, M. Caricato, X. Li, H. P. Hratchian, A. F. Izmaylov, J. Bloino, G. Zheng, J. L. Sonnenberg, M. Hada, M. Ehara, K. Toyota, R. Fukuda, J. Hasegawa, M. Ishida, T. Nakajima, Y. Honda, O. Kitao, H. Nakai, T. Vreven, J. A. Montgomery, Jr., J. E. Peralta, F. Ogliaro, M. Bearpark, J. J. Heyd, E. Brothers, K. N. Kudin, V. N. Staroverov, R. Kobayashi, J. Normand, K. Raghavachari, A. Rendell, J. C. Burant, S. S. Iyengar, J. Tomasi, M. Cossi, N. Rega, J. M. Millam, M. Klene, J. E. Knox, J. B. Cross, V. Bakken, C. Adamo, J. Jaramillo, R. Gomperts, R. E. Stratmann, O. Yazyev, A. J. Austin, R. Cammi, C. Pomelli, J. W. Ochterski, R. L. Martin, K. Morokuma, V. G. Zakrzewski, G. A. Voth, P. Salvador, J. J. Dannenberg, S. Dapprich, A. D. Daniels, . Farkas, J. B. Foresman, J. V. Ortiz, J. Cioslowski, D. J. Fox, Gaussian 09 Revision D.01, gaussian Inc. Wallingford CT 2009.

[87] J. E. Peralta, J. I. Melo, Magnetic Exchange Couplings with Range-Separated Hybrid Density Functionals, J. Chem. Theory Comput. 6 (6) (2010) 1894–1899. doi:10.1021/ct100104v.

[88] I. Rudra, Q. Wu, T. Van Voorhis, Accurate magnetic exchange couplings in transition-metal complexes from constrained density-functional theory., J. Chem. Phys. 124 (2) (2006) 024103. doi:10.1063/1.2145878.

[89] A. D. Becke, Density-functional thermochemistry.III. The role of exact exchange, J. Chem. Phys. 98 (7) (1993) 5648. doi:10.1063/1.464913.

[90] P. Stephens, F. J. Devlin, C. F. Chabalowski, M. J. Frisch, Ab-Initio Calculation of Vibrational Absorption and Circular-Dichroism Spectra Using Density-Functional Force-Fields, J. Phys. Chem. 98 (45) (1994) 11623–11627. doi:10.1021/j100046a014.

[91] A. V. Krukau, O. A. Vydrov, A. F. Izmaylov, G. E. Scuseria, Influence of the exchange screening parameter on the performance of screened hybrid functionals, J. Chem. Phys. 125 (22). doi:10.1063/1.2404663.

[92] O. A. Vydrov, G. E. Scuseria, J. P. Perdew, Tests of functionals for systems with fractional electron number, J. Chem. Phys. 126 (15). doi:10.1063/1.2723119.

[93] T. Yanai, D. P. Tew, N. C. Handy, A new hybrid exchange-correlation functional using the Coulomb-attenuating method (CAM-B3LYP), Chem. Phys. Lett. 393 (1-3) (2004) 51–57. doi:10.1016/j.cplett.2004.06.011.

[94] J. P. Perdew, K. Burke, Y. Wang, Generalized gradient approximation for the exchange-correlation hole of a many-electron system, Physical Review B 54 (23) (1996) 16533.

[95] J.-D. Chai, M. Head-Gordon, Long-range corrected hybrid density functionals with damped atom-atom dispersion corrections., Phys. Chem. Chem. Phys. 10 (44) (2008) 6615–6620. doi:10.1039/b810189b.

[96] E. Ruiz, J. Cano, S. Alvarez, P. Alemany, Broken symmetry approach to calculation of exchange coupling constants for homobinuclear and heterobinuclear transition metal complexes, J. Comput. Chem. 20 (13) (1999) 1391–1400.

[97] A. Schäfer, C. Huber, R. Ahlrichs, Fully optimized contracted gaussian basis sets of triple zeta valence quality for atoms li to kr, J. Chem. Phys. 100 (8) (1994) 5829–5835.

[98] A. Schäfer, H. Horn, R. Ahlrichs, Fully optimized contracted gaussian basis sets for atoms li to kr, J. Chem. Phys. 97 (4) (1992) 2571–2577.

[99] R. Seeger, J. A. Pople, Self-consistent molecular orbital methods. XVIII. Constraints and stability in Hartree–Fock theory, J. Chem. Phys. 66 (7) (1977) 3045.

[100] R. Bauernschmitt, R. Ahlrichs, Stability analysis for solutions of the closed shell Kohn–Sham equation, J. Chem. Phys. 104 (22) (1998) 9047–9052.

[101] H. P. Hratchian, H. B. Schlegel, Finding Minima, Transition States, and Following Reaction Pathways on Ab Initio Potential Energy Surfaces, in: C. E. Dykstra, G. Frenking, K. S. Kim, G. E. Scuseria (Eds.), Theory and Applications of Computational Chemistry, Elsevier, Amsterdam, 2005, pp. 195–249.

[102] T. F. Hughes, R. a. Friesner, Correcting Systematic Errors in DFT Spin-Splitting Energetics for Transition Metal Complexes, J. Chem. Theory Comput. 7 (1) (2011) 19–32. doi:10.1021/ct100359x.

[103] J. Tomasi, B. Mennucci, R. Cammi, Quantum mechanical continuum solvation models, Chemical Reviews 105 (8) (2005) 2999–3094. doi:10.1021/cr9904009.

[104] G. Scalmani, M. J. Frisch, Continuous surface charge polarizable continuum models of solvation. i. general formalism, J. Chem. Phys. 132 (11) (2010) 114110. doi:10.1063/1.3359469.

[105] C. Mathoniere, O. Kahn, J. C. Daran, H. Hilbig, F. H. Koehler, Complementarity and internal consistency between magnetic and optical properties for the manganese(II) copper(II) heterodinuclear compound, Inorg. Chem. 32 (19) (1993) 4057–4062. doi:10.1021/ic00071a015.

[106] W. Z. Heisenberg, Phys. A: Hadrons Nucl. 49 (1928) 619–636.

[107] S. A. Stoian, C. Paraschiv, N. Kiritsakas, F. Lloret, E. Münck, E. L. Bominaar, M. Andruh, Mössbauer, electron paramagnetic resonance and magnetic susceptibility studies on members of a new family of cyano-bridged 3d-4f complexes. demonstration of anisotropic exchange in a Fe-Gd complex, Inorg. Chem. 49 (7) (2010) 3387–3401. doi:10.1021/ic902516r.

[108] D. Dai, M. H. Whangbo, Spin exchange interactions of a spin dimer: Analysis of broken-symmetry spin states in terms of the eigenstates of Heisenberg and Ising spin Hamiltonians, J. Chem. Phys. 118 (1) (2003) 29–39. doi:10.1063/1.1525809.

[109] J. J. Phillips, J. E. Peralta, Magnetic exchange couplings from semilocal functionals evaluated nonself-consistently on hybrid densities: Insights on relative importance of exchange, correlation, and delocalization, J. Chem. Theory Comput. 8 (9) (2012) 3147–3158. doi:10.1021/ct3004904.

[110] E. Ruiz, P. Alemany, S. Alvarez, J. Cano, Structural Modeling and Magneto-Structural Correlations for Hydroxo-Bridged Copper(II) Binuclear Complexes., Inorg. Chem. 36 (17) (1997) 3683–3688. doi:10.1021/ic970310r.

[111] A. Rodrguez-fortea, P. Alemany, S. Alvarez, E. Ruiz, A. Rodr, Exchange Coupling in Halo-Bridged Dinuclear Cu (II) Compounds : A Density Functional Study, Inorg. Chem. 41 (Ii) (2002) 3769–3778. doi:10.1021/ic011308.

[112] T. Saito, W. Thiel, Analytical gradients for density functional calculations with approximate spin projection, J. Phys. Chem. A 116 (44) (2012) 10864–10869. doi:10.1021/jp308916s.

[113] E. Ruiz, P. Alemany, S. Alvarez, J. Cano, Toward the Prediction of Magnetic Coupling in Molecular Systems: Hydroxo- and Alkoxo-Bridged Cu (II) Binuclear Complexes, J. Am. Chem. Soc. 119 (Ii) (1997) 1297–1303.

[114] R. Valero, R. Costa, I. De P. R. Moreira, D. G. Truhlar, F. Illas, Performance of the M06 family of exchange-correlation functionals for predicting magnetic coupling in organic and inorganic molecules, J. Chem. Phys. 128 (11). doi:10.1063/1.2838987.

[115] E. Ruiz, S. Alvarez, J. Cano, V. Polo, About the calculation of exchange coupling constants using density-functional theory: the role of the self-interaction error., J. Chem. Phys. 123 (16) (2005) 164110. doi:10.1063/1.2085171.

[116] J. J. Phillips, J. E. Peralta, The role of range-separated Hartree-Fock exchange in the calculation of magnetic exchange couplings in transition metal complexes, J. Chem. Phys. 134 (3). doi:10.1063/1.3531696.

[117] K. Goushi, K. Yoshida, K. Sato, C. Adachi, Organic light-emitting diodes employing efficient reverse intersystem crossing for triplet-to-singlet state conversion, Nature Photonics 6 (4) (2012) 253.

[118] N. J. Turro, V. Ramamurthy, V. Ramamurthy, J. C. Scaiano, Principles of molecular photochemistry: an introduction, University science books, 2009.

[119] M. Klessinger, J. Michl, Excited states and photochemistry of organic molecules, Wiley-VCH, 1995.

[120] A. Maciejewski, R. P. Steer, The photophysics, physical photochemistry, and related spectroscopy of thiocarbonyls, Chemical reviews 93 (1) (1993) 67–98.

[121] J. B. Delos, On the reactions of N_2 with O, The Journal of Chemical Physics 59 (5) (1973) 2365–2369.

[122] N. Harris, S. Shaik, D. Schröder, H. Schwarz, Single-and Two-State Reactivity in the Gas-Phase C−H Bond Activation of Norbornane by Bare FeO^+, Helvetica chimica acta 82 (10) (1999) 1784–1797.

[123] D. R. Yarkony, Theoretical studies of spin-forbidden radiationless decay in polyatomic systems: insights from recently developed computational methods, Journal of the American Chemical Society 114 (13) (1992) 5406–5411.

[124] J. N. Harvey, Spin-forbidden reactions: computational insight into mechanisms and kinetics, Wiley Interdisciplinary Reviews: Computational Molecular Science 4 (1) (2014) 1–14.

[125] D. R. Yarkony, Systematic determination of intersections of potential energy surfaces using a lagrange multiplier constrained procedure, The Journal of Physical Chemistry 97 (17) (1993) 4407–4412.

[126] J. N. Harvey, Understanding the kinetics of spin-forbidden chemical reactions, Physical Chemistry Chemical Physics 9 (3) (2007) 331–343.

[127] N. Koga, K. Morokuma, Determination of the lowest energy point on the crossing seam between two potential surfaces using the energy gradient, Chemical physics letters 119 (5) (1985) 371–374.

[128] M. R. Manaa, D. R. Yarkony, On the intersection of two potential energy surfaces of the same symmetry. systematic characterization using a lagrange multiplier constrained procedure, The Journal of chemical physics 99 (7) (1993) 5251–5256.

[129] R. Fletcher, Practical methods of optimization, 2nd Edition, Wiley, Chichester.

[130] T. W. Keal, A. Koslowski, W. Thiel, Comparison of algorithms for conical intersection optimisation using semiempirical methods, Theoretical Chemistry Accounts: Theory, Computation, and Modeling (Theoretica Chimica Acta) 118 (5) (2007) 837–844.

[131] C. Ciminelli, G. Granucci, M. Persico, The photoisomerization mechanism of azobenzene: A semiclassical simulation of nonadiabatic dynamics, Chemistry-A European Journal 10 (9) (2004) 2327–2341.

[132] M. J. Bearpark, M. A. Robb, H. B. Schlegel, A direct method for the location of the lowest energy point on a potential surface crossing, Chemical physics letters 223 (3) (1994) 269–274.

[133] J. N. Harvey, M. Aschi, H. Schwarz, W. Koch, The singlet and triplet states of phenyl cation. a hybrid approach for locating minimum energy crossing points between non-interacting potential energy surfaces, Theoretical Chemistry Accounts: Theory, Computation, and Modeling (Theoretica Chimica Acta) 99 (2) (1998) 95–99.

[134] L. Grippo, F. Lampariello, S. Lucidi, A nonmonotone line search technique for newtons method, SIAM Journal on Numerical Analysis 23 (4) (1986) 707–716.

[135] X. Li, M. J. Frisch, Energy-represented direct inversion in the iterative subspace within a hybrid geometry optimization method, Journal of chemical theory and computation 2 (3) (2006) 835–839.

[136] S. Ruiz-Barragan, M. A. Robb, L. Blancafort, Conical intersection optimization based on a double newton–raphson algorithm using composed steps, Journal of chemical theory and computation 9 (3) (2013) 1433–1442.

[137] Ö. Farkas, H. B. Schlegel, Methods for optimizing large molecules. part iii. an improved algorithm for geometry optimization using direct inversion in the iterative subspace (gdiis), Physical Chemistry Chemical Physics 4 (1) (2002) 11–15.

[138] P. Pulay, P. pulay, j. comput. chem. 3, 556 (1982)., J. Comput. Chem. 3 (1982) 556.

[139] F. Eckert, P. Pulay, H.-J. Werner, Ab initio geometry optimization for large molecules, Journal of computational chemistry 18 (12) (1997) 1473–1483.

[140] K. N. Kudin, G. E. Scuseria, E. Cances, A black-box self-consistent field convergence algorithm: One step closer, The Journal of chemical physics 116 (19) (2002) 8255–8261.

[141] A. Banerjee, N. Adams, J. Simons, R. Shepard, Search for stationary points on surfaces, The Journal of Physical Chemistry 89 (1) (1985) 52–57.

[142] J. Simons, J. Nichols, Strategies for walking on potential energy surfaces using local quadratic approximations, International Journal of Quantum Chemistry 38 (S24) (1990) 263–276.

[143] N. J. Turro, Y. Cha, I. R. Gould, Reactivity and intersystem crossing of singlet methylene in solution, Journal of the American Chemical Society 109 (7) (1987) 2101–2107.

[144] J. Wang, D. Smith, R. Grice, Role of Intersystem Crossing in the Dynamics of the O (3P)+ C_2H_5I Reaction, The Journal of Physical Chemistry 100 (16) (1996) 6620–6625.

[145] K. J. Watanabe, N. Nakatani, A. Nakayama, M. Higashi, J. Y. Hasegawa, Spin-Blocking Effect in CO and H_2 Binding Reactions to Molybdenocene and Tungstenocene: A Theoretical Study on the Reaction Mechanism via the Minimum Energy Intersystem Crossing Point, Inorganic Chemistry 55 (16) (2016) 8082–8090. doi:10.1021/acs.inorgchem.6b01187.

[146] V. E. Henrich, P. A. Cox, The surface science of metal oxides, Cambridge university press, 1996.

[147] K. Tanabe, Surface and catalytic properties of ZrO_2, Materials chemistry and physics 13 (3-4) (1985) 347–364.

[148] N. Greenwood, A. Earnshaw, Chemistry of the Elements 2nd Edition, Butterworth-Heinemann, 1997.

[149] I. Salem, Recent studies on the catalytic activity of titanium, zirconium, and hafnium oxides, Catalysis reviews 45 (2) (2003) 205–296.

[150] K. Sayama, H. Arakawa, Photocatalytic decomposition of water and photocatalytic reduction of carbon dioxide over zirconia catalyst, The Journal of Physical Chemistry 97 (3) (1993) 531–533.

[151] K. Sayama, H. Arakawa, Effect of carbonate addition on the photocatalytic decomposition of liquid water over a ZrO_2 catalyst, Journal of Photochemistry and Photobiology A: Chemistry 94 (1) (1996) 67–76.

[152] J. E. Miller, M. D. Allendorf, R. B. Diver, L. R. Evans, N. P. Siegel, J. N. Stuecker, Metal oxide composites and structures for ultra-high temperature solar thermochemical cycles, Journal of Materials Science 43 (14) (2008) 4714–4728.

[153] M. Ni, M. K. Leung, D. Y. Leung, K. Sumathy, A review and recent developments in photocatalytic water-splitting using tio2 for hydrogen production, Renewable and Sustainable Energy Reviews 11 (3) (2007) 401–425.

[154] C. Acar, I. Dincer, G. F. Naterer, Review of photocatalytic water-splitting methods for sustainable hydrogen production, International Journal of Energy Research 40 (11) (2016) 1449–1473.

[155] H. H. Kristoffersen, J. Ø. Hansen, U. Martinez, Y. Wei, J. Matthiesen, R. Streber, R. Bechstein, E. Lægsgaard, F. Besenbacher, B. Hammer, et al., Role of steps in the dissociative adsorption of water on rutile tio 2 (110), Physical review letters 110 (14) (2013) 146101.

[156] P. Redfern, P. Zapol, L. Curtiss, T. Rajh, M. Thurnauer, Computational studies of catechol and water interactions with titanium oxide nanoparticles, The Journal of Physical Chemistry B 107 (41) (2003) 11419–11427.

[157] T. Zheng, C. Wu, M. Chen, Y. Zhang, P. T. Cummings, A dft study of water adsorption on rutile tio2 (110) surface: The effects of surface steps, The Journal of chemical physics 145 (4) (2016) 044702.

[158] E. Berardo, M. A. Zwijnenburg, Modeling the water splitting activity of a tio2 rutile nanoparticle, The Journal of Physical Chemistry C 119 (24) (2015) 13384–13393.

[159] S. M. Lang, T. M. Bernhardt, Gas phase metal cluster model systems for heterogeneous catalysis, Physical Chemistry Chemical Physics 14 (26) (2012) 9255–9269.

[160] A. W. Castleman, Cluster structure and reactions: Gaining insights into catalytic processes, Catalysis letters 141 (9) (2011) 1243.

[161] H.-J. Zhai, L.-S. Wang, Probing the electronic structure of early transition metal oxide clusters: Molecular models towards mechanistic insights into oxide surfaces and catalysis, Chemical Physics Letters 500 (4-6) (2010) 185–195.

[162] M. Anpo, T. Shima, S. Kodama, Y. Kubokawa, Photocatalytic hydrogenation of propyne with water on small-particle titania: size quantization effects and reaction intermediates, Journal of Physical Chemistry 91 (16) (1987) 4305–4310.

[163] A. J. Bard, Design of semiconductor photoelectrochemical systems for solar energy conversion, The Journal of Physical Chemistry 86 (2) (1982) 172–177.

[164] J. A. DeVine, A. Abou Taka, M. C. Babin, M. L. Weichman, H. P. Hratchian, D. M. Neumark, High-resolution photoelectron spectroscopy of tio3h2-: Probing the tio2-+ h2o dissociative adduct, The Journal of chemical physics 148 (22) (2018) 222810.

[165] P. Agron, E. Fuller Jr, H. Holmes, IR studies of water sorption on ZrO_2 polymorphs. I, Journal of colloid and interface science 52 (3) (1975) 553–561.

[166] Z. Fang, M. D. Outlaw, K. K. Smith, N. W. Gist, S. Li, D. A. Dixon, J. L. Gole, Computational Study of the Hydrolysis Reactions of Small MO_2 (M= Zr and Hf) Nanoclusters with Water, The Journal of Physical Chemistry C 116 (15) (2012) 8475–8492.

[167] J. B. Kim, M. L. Weichman, D. M. Neumark, High-resolution anion photoelectron spectra of TiO_2^-, ZrO_2^-, and HfO_2^- obtained by slow electron velocity-map imaging, Physical Chemistry Chemical Physics 15 (48) (2013) 20973–20981.

[168] F. Santoro, R. Improta, A. Lami, J. Bloino, V. Barone, Effective method to compute franck-condon integrals for optical spectra of large molecules in solution, The Journal of chemical physics 126 (8) (2007) 084509.

[169] F. Santoro, A. Lami, R. Improta, V. Barone, Effective method to compute vibrationally resolved optical spectra of large molecules at finite temperature in the gas phase and in solution, The Journal of chemical physics 126 (18) (2007) 184102.

[170] D. T. Colbert, W. H. Miller, A novel discrete variable representation for quantum mechanical reactive scattering via the s-matrix kohn method, The Journal of chemical physics 96 (3) (1992) 1982–1991.

[171] J.-D. Chai, M. Head-Gordon, Long-range corrected hybrid density functionals with damped atom–atom dispersion corrections, Physical Chemistry Chemical Physics 10 (44) (2008) 6615–6620.

[172] S. H. Vosko, L. Wilk, M. Nusair, Accurate spin-dependent electron liquid correlation energies for local spin density calculations: a critical analysis, Canadian Journal of physics 58 (8) (1980) 1200–1211.

[173] C. Lee, W. Yang, R. G. Parr, Development of the colle-salvetti correlation-energy formula into a functional of the electron density, Physical review B 37 (2) (1988) 785.

[174] A. D. Becke, Density-functional thermochemistry. iii. the role of exact exchange, The Journal of chemical physics 98 (7) (1993) 5648–5652.

[175] P. Stephens, F. Devlin, C. Chabalowski, M. J. Frisch, Ab initio calculation of vibrational absorption and circular dichroism spectra using density functional force fields, The Journal of Physical Chemistry 98 (45) (1994) 11623–11627.

[176] J. P. Perdew, J. A. Chevary, S. H. Vosko, K. A. Jackson, M. R. Pederson, D. J. Singh, C. Fiolhais, Atoms, molecules, solids, and surfaces: Applications of the generalized gradient approximation for exchange and correlation, Physical Review B 46 (11) (1992) 6671.

[177] F. Weigend, R. Ahlrichs, Balanced basis sets of split valence, triple zeta valence and quadruple zeta valence quality for h to rn: Design and assessment of accuracy, Physical Chemistry Chemical Physics 7 (18) (2005) 3297–3305.

[178] D. Dirk Andrae, unpublished (1989).

[179] S. E. Waller, J. E. Mann, D. W. Rothgeb, C. C. Jarrold, Study of MoNbO y (y= 2–5) Anion and Neutral Clusters using Photoelectron Spectroscopy and Density Functional Theory Calculations: Impact of Spin Contamination on Single Point Calculations, The Journal of Physical Chemistry A 116 (39) (2012) 9639–9652.

[180] N. J. Mayhall, D. W. Rothgeb, E. Hossain, K. Raghavachari, C. C. Jarrold, Electronic structures of mowo y- and mowo y determined by anion photoelectron spectroscopy and dft calculations, The Journal of chemical physics 130 (12) (2009) 124313.

[181] D. Andrae, U. Haeussermann, M. Dolg, H. Stoll, H. Preuss, Energy-adjustedab initio pseudopotentials for the second and third row transition elements, Theoretica chimica acta 77 (2) (1990) 123–141.

[182] H. P. Hratchian, H. B. Schlegel, Finding minima, transition states, and following reaction pathways on ab initio potential energy surfaces, in: Theory and applications of computational chemistry, Elsevier, 2005, pp. 195–249.

[183] A. Osterwalder, M. J. Nee, J. Zhou, D. M. Neumark, High resolution photodetachment spectroscopy of negative ions via slow photoelectron imaging, The Journal of chemical physics 121 (13) (2004) 6317–6322.

[184] D. M. Neumark, Slow electron velocity-map imaging of negative ions: applications to spectroscopy and dynamics, The Journal of Physical Chemistry A 112 (51) (2008) 13287–13301.

[185] C. Hock, J. B. Kim, M. L. Weichman, T. I. Yacovitch, D. M. Neumark, Slow photoelectron velocity-map imaging spectroscopy of cold negative ions, The Journal of chemical physics 137 (24) (2012) 244201.

[186] C. Peng, H. Bernhard Schlegel, Combining synchronous transit and quasi-newton methods to find transition states, Israel Journal of Chemistry 33 (4) (1993) 449–454.